UNIVERSITÀ DEGLI STUDI DI FIRENZE

Facoltà di Scienze Matematiche, Fisiche e Naturali
Dipartimento di Astronomia e Scienze dello Spazio
Dottorato di Ricerca in Astronomia - Ciclo XXIV - FIS/05

Constraing variations of dust properties in circumstellar disk with mm observations

Francesco Trotta

Consigliere Scientifico: **Dr. Leonardo Testi**
Tutore: **Prof. Alessandro Marconi**
Coordinatore: **Prof. Alberto Righini**

Anno Accademico 2011 - 2012

Contents

Chapter 1

Introduction: The Formation of stars and planetary systems

Contents

This first chapter summarize the astrophysical context of the thesis and present the main questions that we want to investigate. We will start with a short review of the paradigm of star formation and in particular for single star with low mass (star of a mass comparable to our Sun). Then we will describe in Sec.1.2 the current most accepted planet formation scenario, the so-called '*core accretion*' model. In Sec.1.3 we will describe the viscous accretion and photoevaportation processes, which drive the evolution of the gas component of the circumstellar disk. We will then describe in Sec.1.4 the dust grain growth and settling processes which operate on the solid particle and regulate the first stage of planet formation. In Sec.1.5 we will present the main questions that we want to investigate related to the first stage of planet formation and we will give a brief summary of the contents of this thesis.

1.1 Star formation

Star formation in our galaxy is a continuous process that occurs inside large concentrations of cold gas and dust, the Giant Molecular Clouds (GMCs). Characterized by temperatures of about 10 K, extent up to 100 parsec and with masses between 10^4 and 10^6 $M_\odot$, the GMCs have complex structure containig smaller scale structure that may be filamentary or clumpy on a wide range of scales ([119] Williams et al. 2000). This strong density inhomogeneity inside the cloud may be generated

by supersonic turbulent motions ([125] Zuckerman and Evas, 1974) as is indicated by the broad and often complex profiles of their molecular emission lines.

1.1.1 Initial condition for the collapse of prestellar cloud cores

It is expected that star formation starts in one of the denser regions '*cores*' of giant molecular clouds by gravitational contraction. The star-forming cores are created by complex processes of molecular cloud dynamics ([75] Larson, 2003) that are not yet full understood and therefore it's not possible specify precisely how the cores begin their collapse. One possiblility, suggested by stability analyses, is that the collapse begins with an unstable core in which gravity gains the upper hand over thermal pressure and causes a runaway collapse to occur ([68, 69] Jeans 1902,1929, [109, 110] Spitzer 1942,1978). The condition for core collapse can be easily estimate with the *virial theorem* which describe the condition of equilibrium for a stable, gravitationally bound system. In the case of a purely pressure-supported core (i.e. in which the only force opposing gravity is the gas thermal pressure) the condition for collapse is

$$2K + U < 0 \tag{1.1}$$

where K,U are, respectively, the kinetic and gravitational potential energy of the core. If we assume, for example, a uniform and isothermal spherical core of radius R, volume $V = 4\pi R^3/3$, mass M, temperature T, density $\rho = M/V$ and mean molecular weight μ, we can write

$$K = \frac{3}{2}\frac{M}{\mu m_H}k_B T \qquad U = -\frac{3}{5}\frac{GM^2}{R}$$

where $k_B = 1.381 \times 10^{-16} ergK^{-1}$ is the Boltzmann constant, $G = 6.674 \times 10^{-8} cm^3 g^{-1} s^{-2}$ is the gravitational constant, $m_H = 1.674 \times 10^{-24} g$ is the mass of the hydrogen atom. The condition (1.1) may be solved for the minimum mass necessary to initiate the spontaneous collapse of the cloud. This condition is know as the *Jeans criterion*

$$M > M_J \qquad M_J = \left(\frac{5k_B T}{G\mu M_H}\right)^{3/2}\left(\frac{3}{4\pi\rho}\right)^{1/2} \tag{1.2}$$

The critical value M_J is called the Jeans mass. Cores which satisfy this condition should thus be gravitationally unstable and will start to collapse. In reality, the physics of a molecular cloud can be more complex as additional physical effect, supporting the core against gravity, can affect the way how the cores begin their collapse. Some possibilities that have been considered are the effects of rotation, magnetic fields and turbulent motions (see the reviews by [75] Larson (2003) and [24] Bonnell et al. (2007)). While the core rotation has been found to be negligible compared to gravity ([9] Arquilla and Goldsmith, 1986; [29] Caselli et al., 2002), magnetic field and turbulence could play an important role in the core stability delaying or preventing the star formation. Many authors ([94] Ostriker et al., 1999;

[76] Li et al., 2004) think that molecular core can collapse only after the magnetic field has been dissipated by ambipolar diffusion ([110] Spitzer, 1978) on a time scale of 10^6 yrs, an order of magnitude higher than the typical free-fall time. Balancing gravity with magnetic energy, critical masses comparable with core masses can be obtained with a magnetic field of about $50\mu G$. Turbulent motions can also prevent cores from collapsing. In many cases, the velocities measured from the width of molecular lines are indeed large enough to sustain the core against the gravity.

1.1.2 Observational classification scheme of YSOs and its theoretical interpretation

The Young Stellar Objects (YSOs) are classified observationally according to the shape of their Spectral Energy Distribution (SED) in the infrared (IR), as first suggestion by [73] Lada and Wilking (1984) and subsequently extended by [5] Andre et al. (1993). At this wavelenght range the YSOs present an infrared excess (over the stellar photospheric contribution) which magnitude is quantified by the slope of the IR SED defined as

$$\alpha_{IR} = \frac{\Delta log(\lambda F_\lambda)}{\Delta log \lambda} \tag{1.3}$$

between the near-IR and the mid-IR. In this way, the YSOs has been classify (Fig. 1.1 left pannels) in:

- **Class 0**: SED peaks in the far-IR or sub-mm part of the spectrum ($\sim 100\mu m$) with no flux being detectable in the near-IR
- **Class I**: approximately flat or rising SED into mid-IR ($\alpha_{IR} > 0$)
- **Class II**: falling SED into mid-IR ($-1.5 < \alpha_{IR} < 0$)
- **Class III**: little or no execess in the IR.

This observational classification scheme is theoretically interpreted as an evolutionary scenario sequence ([1] Adams, Lada & Shu, 1987). According this scenario, from the gravitational collapse of cores until the formation of the final star, this four class objects can be described (Fig. 1.1 right pannels) as follow:

- **Class 0**: Once a core becomes gravitational unstable, it starts to collapse. The *collapse phase* is very short in comparison to the other phases of star formation. For a typical inital density of a molecular core $\rho = 3.3 \times 10^{-19} gcm^{-3}$, the free fall time, for a spherical core, is $t_{ff} \sim 10^5 yrs$. In this phase the forming protostar is completely embedded by the collapsing envelope and cannot be observed at optical and IR wavelengths yet. The spectra peak at far-IR or sub-millimeter wavelengths.
- **Class I**: The free fall approximation breaks down when the heating from gravitational energy, released during the infall, increases the pressure of the gas

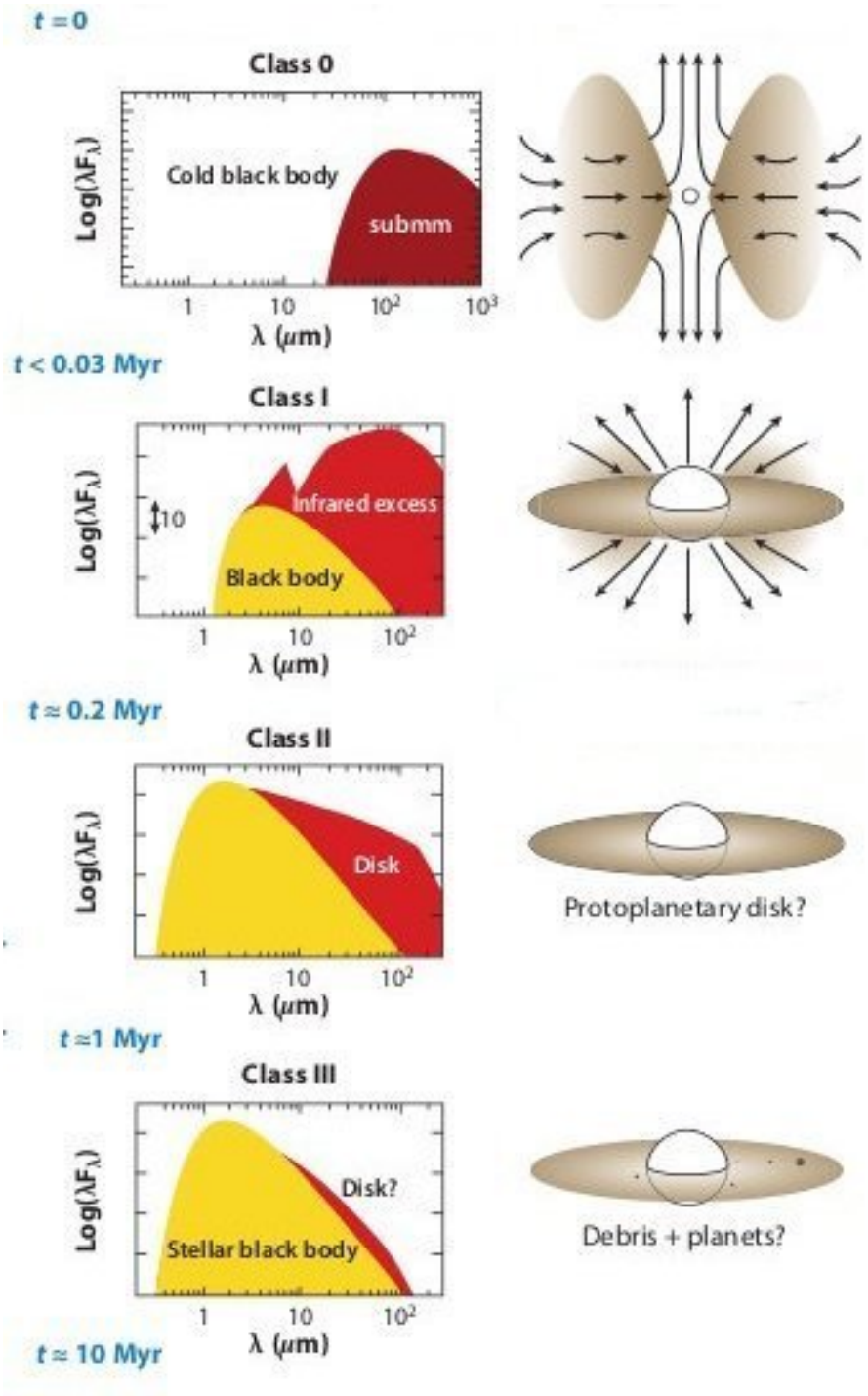

Figure 1.1: Different evolutionary stages during the formation process of a single star. The left panels show the spectral energy distribution (SEDs) of the system and the right panels the corrisponding system geometry. As the protostar accretes material from the surrounding circumstellar disk approaching the final MS-star stage, the peak of the emission shifts to shorter wavelengths and the IR excess diminishes.

sufficiently to resist further contraction. The system now enters the *protostellar phase*. During the protostellar phase, sometimes, strong bipolar outflows are observed to develop, i.e. strong winds moving radially outwards from the polar regions at high speed ($10 - 200 Km\ s^{-1}$). In this phase the protostar are still obscured by the surroundig envelope, making them difficult to observe at optical wavelengths. Their spectra peak at far-IR wavelengths.

- **Class II**: Once most of the collapsing molecular core has either accreted onto the star, been blown away by the bi-polar outflow, or settled in the disk, it enters in a more stable phase that lasts a few million years, the *T Tauri phase*. The star continues to accrete gas from the disk, adding a luminosity to the star comparable to the energy generated from the internal fusion. In this phase the T Tauri stars are more easily seen than their younger counterparts, the protostars, because of the clearing of the ambient medium. Their spectra is composed by the protostellar emission and the flux arising from circumstellar disk. The disk contributes to the emission at $\lambda \geq$ IR-wavelengths producing an excess of radiation as compared to the naked stellar photosphere.

- **Class III**: After most of the material in the disk around a T Tauri star has accreted/been blown away, what remains is a protostar surround by an exiguous residual disk. The protostar has now ceased its strong magnetic activity, and is no longer accreting any significant mass from the circumstellar disk. The disks are thought to be thin and dusty (in the sense that the total disk mass is small and mostly contained in dust) and possibly with planets. This disk is usually very difficult to observe as its emission is strongly overwhelmed by the star emission. The spectra of this objects has a pure stellar photospheric shape.

1.2 Planet formation

The detection and study of planets outside our solar system is one of the great scientific, technological and philosophical undertakings of our time. During the last years great efforts have been done to understand the origin and evolution of planets and maybe most importantly to check for the presence of even primitive life elsewhere in the universe. There is now clear evidence for a substatial numbers of planets orbiting other stars. From both space and ground-based instruments and using both direct and indirect techniques (see [70] Jones 2008 for a brief review), more then 700 planets have been discovered (Fig. 1.2).

The basic challenge of planet formation consists of assembling, in a disk orbiting a central star, the initial ISM dust grains of sub-mm size in bodies with over 10^4 km in diameter (fig.1.3), a growth by nearly a factor 10^{13} in size or 10^{40} in mass. In the study of plant formation is useful to consider different *size regimes* in which the interaction between the solid component and the gas is qualitatively different:

- **Dust** - small particles from sub-mm to cm in size. They are very well-coupled

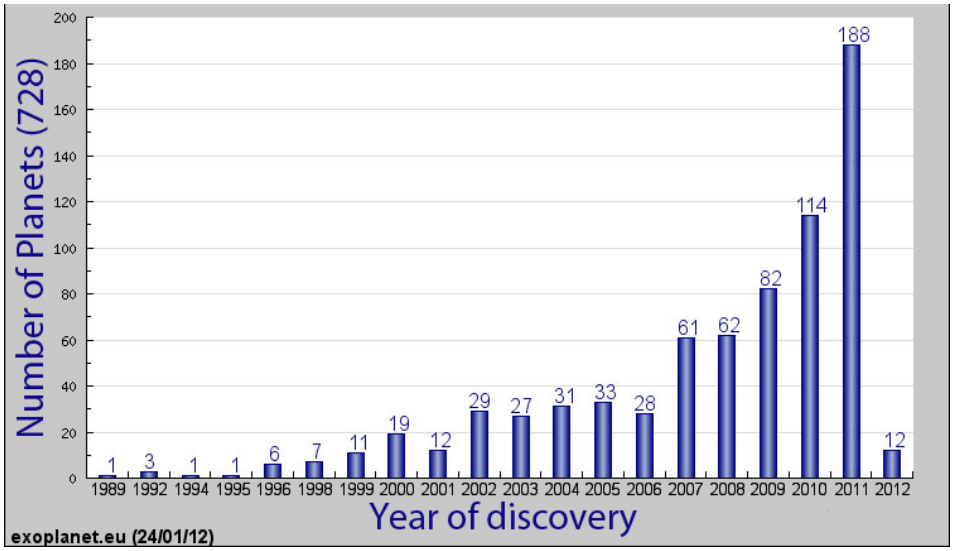

Figure 1.2: Number of extrasolar planets versus year of discovery (generated from the online Extrasolar Planets Encyclopedia www.exoplanet.eu).

to the gas and their dynamic is drived by a very strong drag forces with the gas.

- **Rocks** - objects from cm to km in size. They are still coupled to the gas but this couppled become more and more weak with the increasing of the size.
- **Planetesimals** - objects from 1km to 10^3km in size. They are massive enough to be complitely decoupled to the gas and their dynamic is drived mainly from the gravitational field.
- **Planets** - objects of 10^3 km and above. They again become coupled to the gas but this time no via aerodynamic interaction but via gravitational interaction.

The process of planet formation involve a complex interaction of many factor such as turbulent motion of the gas, magnetic processes, incident radiation field, chimical composition of the dust. Considerable progress has been done over the past two decade but there are still different unresolved issues. However, the most widely accepted planet formation model is the so-colled '*core accertion*' model. Basically the evolutionary scenario of this model involves three stages (see Fig. 1.3)

1. *Sticking and coagulation*: In the early stage the initial sub-μm ISM dust particles grow up via collisions and stiking where the collisions are drived by aerodynamic interaction. This growth could continues unitil 1 km-size bodies with the formation of planetesimals. However, while growth from dust grains to roughly meter sized bodies can be reasonably well modeled with classical coagulation simulations ([26] Brauer et al. 2008), how to continue from m-size to km-size bodies is still an unsolved problem, the so colled '*meter barrier*' problem.

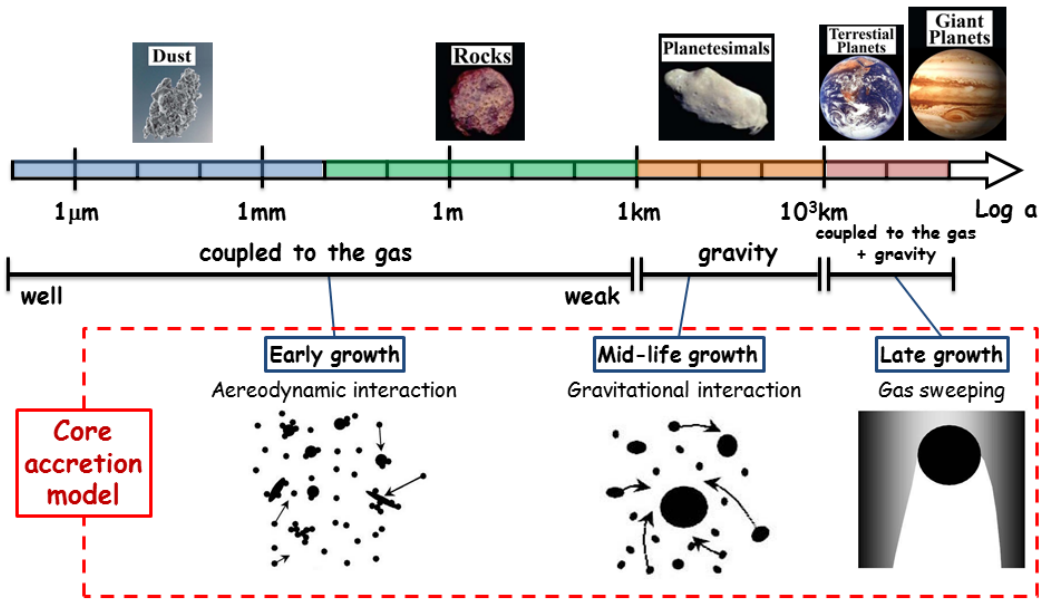

Figure 1.3: Sequence of events leading to the assembly of the sub-micro dust grains in planets according the core accertion model: (1) grain growth through particle-particle interactions, (2) growth of planetesimals by two-body interactions aided by gravity, and (3) the accretion of gas via gravitational attraction.

2. *Gravitational attraction*: Beyond 1km-size bodies, gravity is the clearly dominant force and the planetesimals grow up via collisions drived by gravitational interaction. This leads to the formation of planetary rocky cores.

3. *Gas sweeping*: The rocky cores then attract the surrounding gas which eventually form their atmospheres. In this late stage the forming planets heavily interact with the disk, opening gaps and migrating towards the inner regions. If the planetary core become massive enough, it will able to accretes and hold on a large amounts of gas forming the giant planets.

1.3 Formation and Evolution of disks

Accretion disks around YSOs appear as a natural consequence of the gravitational collapse of material with nonzero angular momentum ($\mathbf{L} \neq 0$). Even if the molecular core have initially a very low rotation velocity, as the core collapse, the rate of rotation increase to conserve angular momentum with a consequence formation of flattened structure perpendicular to the rotational axis, a *disk*. This can be understood if one consider a collapsing spherical core rotating around one single axis. Matter falling toward the center along the direction of rotational axis ($\mathbf{L}$ direction), does not feel the resistance of inertial momentum and contracts freely. In contrast, matter falling in perpendicular to $\mathbf{L}$ has to transfer a high fraction of its infall velocity to a rotational velocity; in this case it will not be able to fall freely on the

protostar but will settle down in the minimum energy orbit for a given angular momentum, i.e. a circular orbit at a certein radius R. The radius can be estimate considering as specific angular momentum that appropriate for a keplerian orbit, i.e. $l_k = \sqrt{GMR}$. If we assume a core with constant density, mass $M \approx 1M_\odot$ and total angular momentum $J \approx 10^{54} g\ cm^2 s^{-1}$, then the fluid elements with an average specific angular momentum $l = J/M_\odot = 10^{21} cm^2 s^{-1}$ will adopts keplerian orbit around the protostar at a distance $R = l^2/GM \approx 500$ AU. This is clearly much larger than the size of the star, so the gas needs to redistribute the angular moment in order to accrete further to the center. In reality, the physics of a cloud core collapse is much more complicated because turbulence and magnetic field can also play an important role during the collapse. The formation of a disk is however a well estabilished outcome, also of more realistic simulation of cloud collapse ([64] Inutsuka et al. 2010).

Understanding the physical processes that drive the evolution of primordial circumstellar disks, is crucial for our understanding of planet formation. Disks evolve through various processes, including viscous accretion, photo-evaporation by ultraviolet and X-ray radiation, dust grain growth and settling. Here we summarize the models and observational constrains for the different processes that control the evolution of circumstellar disks. In this section we focus on the evolution of the gas, which dominate the mass of the disk. The evolution of the solid component, which is partially coupled to the gas but which also involves distinct physical processes, is discuss in the next section.

1.3.1 Viscous angular momentum transport

In order to let the matter of the disk fall into the the central star, we need a method of redistributing angular momentum throughout the disk, and the central problem of accretion disk theory is to determine why this should occur. For protoplanetary disk, one possibility is the 'viscous' evolution of the gas (e.g. [107] Shakura and Sunyaev 1973, [81] Lynden-Bell & Pringle 1974, [101] Pringle 1981) which will be briefly summarized in this section.

1.3.1.1 The magnitude of molecular viscosity

It is well know that molecular viscosity does not provide enought stress to power disk accretion and can be neglected. In order to see this, let consider the viscous timescale (i.e. time scale on which viscosity smooth out surface density gradient on the radial scale R)

$$t_\nu = \frac{R^2}{\nu_m} \tag{1.4}$$

Molecular viscosity can be expressed as $\nu_m \sim \lambda c_s$, the product of the typical random velocity of molecules (that will be of the order of the sound speed c_s) and the collisional mean free path $\lambda = 1/n\sigma$ where n is the number density of molecules with cross-section for collision σ. To give an idea of the number involved, let's

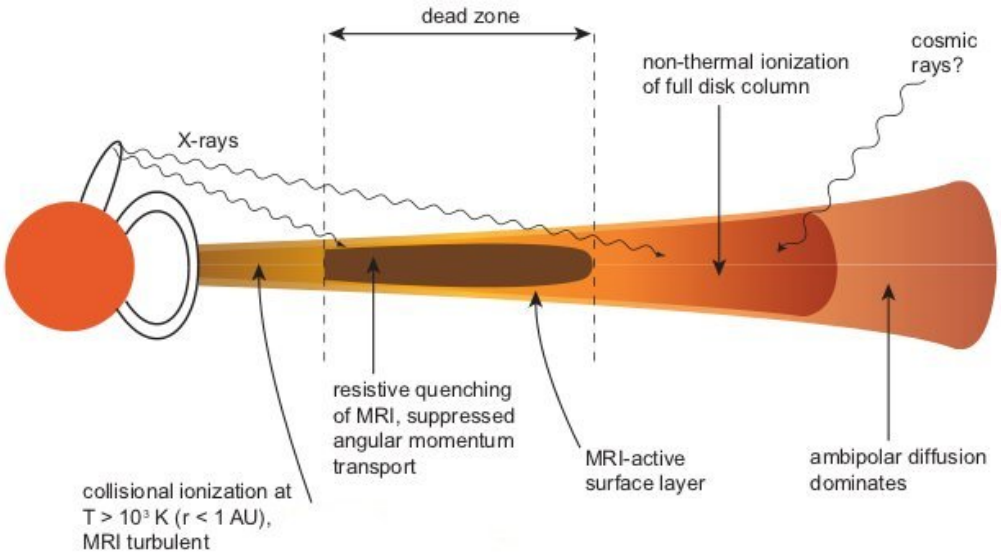

Figure 1.4: Illustration of the layered disk model proposed by Gammie (1996) [52]. In this model the innermost regions of the disk are hot enough such that thermal ionization suffices to couple the magnetic field to the gas well enough for the MRI to operate. At large radii, cosmic rays or stellar X-rays penetrate deep enough into the disk to provide the necessary level of ionization. At intermedi- ate radii, it is hypothesized that accretion occurs primarily in an active surface layer ionized by these nonthermal processes, while the central 'dead zone' is magnetically inactive.

consider, for example, a protoplanetary disk with $\Sigma = 10^3 gcm^{-2}$ and $H/R = 0.05$ at 1 AU. The number density is of the order of $n \sim \Sigma/2m_H H \sim 4 \times 10^{14} cm^{-3}$, the collision cross-section of a hydrogen molecule is of the order of $\sigma \sim 2 \times 10^{-15} cm^2$ and the sound speed is $c_s \sim 1.5 \times 10^5 cms^{-1}$. So the molecular viscosity is

$$\nu_m \sim 2 \times 10^5 cm^2 s^{-1} \tag{1.5}$$

This implied viscous time scale $t_\nu \sim 10^{12} yrs$. This time scale can be estimate observationally by measuring, for example, the rate at which accretion on to the star decays as a function of the stellar age and for protoplanetary disks around Solar-type stars it appears to be of the order of a $10^6 yrs$. The value we have estimete is so approximatly 10^6 times longer then the observed time scale for disk evolution and so the molecular viscosity can not be the source of angular momentum transport within disks.

1.3.1.2 Turbulent viscosity and its possible physical origin

Given the insignificance of direct (molecular) viscosity transport of angular momentum, the central question in the accretion disk theory is so understand which are the dominant physical mecchanisms responsible for the angular momentum transport

within disks. In general to evaluate the importance of the inertial effect respect to viscous effect for a given flow, one consider the *Reynolds number* which is defined

$$Re = \frac{UL}{\nu_m} \tag{1.6}$$

where U and L are the characteristic velocity and lenght scales in the system. Low Reynolds numbers occurs for laminar flow which is dominated by viscous forces and is characterized by smooth, constant fluid motion; high Reynolds numbers occurs for turbulent flow which is dominated by inertial forces and tend to produce chaotic eddies, vortices and other flow instabilities. For the accretion disks, taking $U = c_s$, $L = H$ and using the parameters of the previous section (for the estimation of ν_m), we have Reynold number extremely large ($\sim 10^{14}$) and the flow is therefore expect to be highly turbulent. Typically, turbulence results in a much greater effective viscosity which produce a much efficient trasport. Turbulent motion in the accretion disks can be therefore the key to solve the angular momentum transport problem.

Which might be the physical cause for the turbulence? The turbulence requires a source (es. an instability) and until now a variety of instability have been proposed to explane the origine of such turbulence. The most intensively studied mechanism are self-gravity ([113] Toomre 1964) and magnetorotational instability ([13] Balbus and Hawley, 1991). These originate from linear instabilities. Hydrodynamic instabilities associated with the disk's radial thermal structure (baroclinic instability) could also contribute to angular momentum transport, through the non-linear formation of vortices (see the reviews by [8]). An important quantity in turbulent trasport theories in accretion disk is the *shear stress tensor* $T_{R\phi}$. It is constituted by the correlated fluctuations which constituite the source of the transport.

- In the pure hydrodynamic flow the only relevant field is the velocity fluctuation field, and this contribution to the stress tensor (called the 'Reynolds' stress) is $T^{Re}_{R\phi} = -\Sigma\langle u^{Re}_R u^{Re}_\phi\rangle$ where $\mathbf{u}^{Re}$ is the velocity fluctuation
- In the case of a magnetized disk, the magnetic field $\mathbf{B}$ provides another source of transport, leading to the so-called 'Maxwell' stress $T^M_{R\phi} = \Sigma\langle u_{A,R} u_{A,\phi}\rangle$ where $\mathbf{u}_A = \mathbf{B}/\sqrt{4\pi\rho}$ is the Alfvén velocity.
- If the disk is massive enough that its self-gravity is non-negligible, the perturbated gravitationl field $\mathbf{g}$ provides yet another source of transport, in the form: $T^g_{R\phi} = -\Sigma\langle u^g_R u^g_\phi\rangle$ where $\mathbf{u}^g = \mathbf{g}/\sqrt{4\pi G\rho}$

Models suggest that protoplanetary disks are likely to have both magnetically active zones, where the disk is turbulent, and adjacent magnetically '*dead-zones*' where the flow can be laminar (figure 1.4) (e.g. [52] Gammie 1996; [48] Fromang et al. 2002; [63] Ilgner e Nelson 2006).

1.3.1.3 α Model of Protoplanetary disks

Absent detailed knowledge of the physical origin of the angular momentum transport, the classical approach to construct a viscous disk models is adopting the 'α *prescription*' ([107] Shakura & Sunyaev 1973). It postulate a source of disk viscosity due to turbulence and suggest that whatever is the source of turbulence, the resulting stress should be proportional to the local gas pressure. In vertical integrated form

$$T_{R\phi} = \frac{dln\Omega}{dlnR}\alpha P \tag{1.7}$$

where $P = \Sigma c_s^2$ stand for the averange pressure and $dln\Omega/dlnR \sim -3/2$ for a keplerian disk. The proportionality factor α is a dimensionaless quantity, know as the Shakura-Sunyaev α parameter, that measure the strength of the turbulence in the disk and so the efficiency of angular momentum transport due to turbulence. Another way of expressing the α prescription is by considering the viscosity ν. As showed in [101] Pringle 1981 the expression 1.7 is equivalent to

$$\nu = \alpha c_s H \tag{1.8}$$

The simplest and usually adopted approach to construct viscous disk model is to assume that α is a constant. Models of this type have been constructed, for example, by [19] Bell et al. (1997), [34] D'alessio et al. (1998). The value of α itself can be constrained by studies of the evolution of the stellar accretion rate ([56] Hartmann et al. 1998), or by detailed studies of individual systems ([62] Hueso & Guillot 2005). These methods typically yield $\alpha \sim 10^2$, with large uncertainties.

Although α models provide a parsimonious description of the observations in terms of a single free parameter, there are compelling reasons to think that they are not a full description of protoplanetary disks. There are not physical reason to take α constant. In general α may vary with the temperature, density and composition of the disk gas and there may even be regions which fail to satisfy the basic assumtion by not developping turbulence at all ([45] Flock & al. 2011). Typical values range between $\alpha = 10^{-6}$ and 10^{-2}, where the former corresponds to the turbulent strength in dead zones, the latter describes turbulence in disk atmospheres. Despite the ongoing development of increasingly sophisticated large scale numerical models, simple α disk model continue to represent a useful starting point for disk studies and remains the central link between theory and observations.

1.3.2 Photoevaporation

Together with viscous accretion, photoevaporation is one of the main mechanisms through which primordial circumstellar disks are believed to lose mass and eventually dissipate. The basic physics of photoevaporation ([108] Shu, Johnstone & Hollenbach 1993) is illustrated in Figure 1.5. Ionizing radiation from the central star, or from external stars, impinges on the disk surface and heats a relatively thin skin of gas to a temperature $T_{surf} > T_{eff}$. At some radius R_g, the sound speed c_s

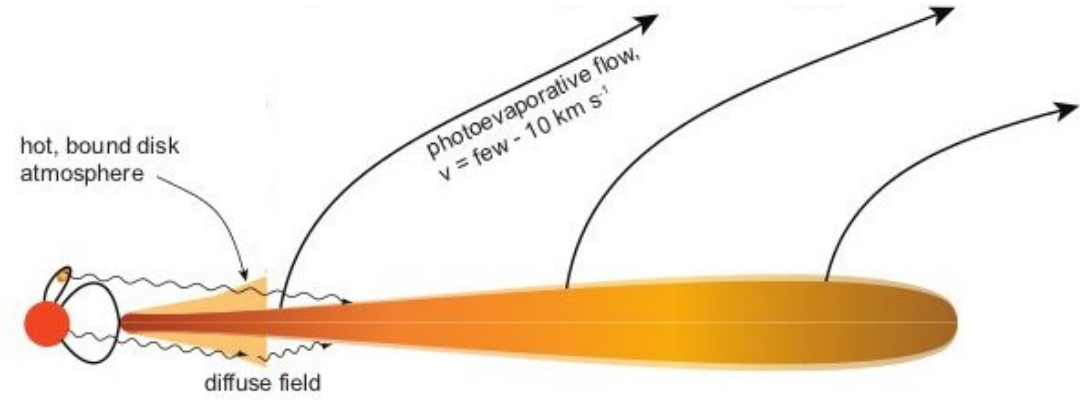

Figure 1.5: Schematic illustration of a photoevaporation process. Inside the gravitational radius R_g an ionizzed disk atmosphere is formed. Ouside R_g the UV or X-ray radiation from the central star, or from external stars, heats the disk surface to a temperature such that the gas is unbound and it can flow away from the disk.

in the surface layer equals the local Keplerian velocity, where R_g is given by,

$$R_g = \frac{GM_*}{c_s^2} \tag{1.9}$$

At radii $R < R_g$ the warm ionizzed disk atmosphere is gravitationally bound and at radii $R > R_g$ the gas in the surface layer is unbound and it can flow freely away from the disk as a wind driven by thermal pressure gradients. In this simplest form, then, photoevaporation is a 'pure' mass loss process, that diminishes Σ locally at each radius without causing additional evolution due to angular momentum loss. More detailed hydrodynamic models show that this division is not entirely sharp but gas can escape at a reduced rate from radii as small as $R_{cr} \backsimeq 0.1R_g$ ([77] Liffman 2003; [2] Adams et al. 2004; [46] Font et al. 2004).

Photoevaportion requires surface temperature high enough that they can only be attained as a result of disk irradiation by energetic photons: Far-ultraviolet (FUV) radiation ($6eV < h\nu < 13.6eV$), Extreme-ultraviolet (EUV) radiation ($13.6eV < h\nu < 0.1keV$) and X-rays ($h\nu > 0.1keV$). Photons in each energy range affect the disks in different ways, and the relative importance of FUV, EUV, and X-ray photoevaporation is still not well understood

The viscous evolution of the disk, discussed in Sec. 1.3.1, can be strongly affected by this photoevaporation process. Recente models, known as '*UV-switch*', tried to incorporate both viscous evolution and photoevaporation by EUV photons ([33] Clarke et al. 2001, [3, 4] Alexander et al. 2006a,b). According these models the evolution of the gas disk can be describe in three stages (see Fig. 1.6)

- *Viscous phase*: (few Myr). At early stage, the photoevaporative wind is negligible and the disc evolves due to viscous transport of angular momentum. Most of the disc mass is accreted on to the star, and most of the angular momentum is transported to large radii.

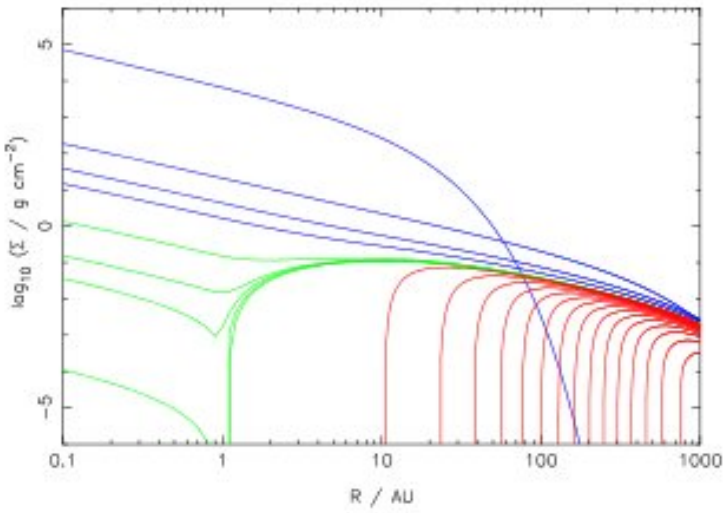

Figure 1.6: Evolution of the surface density of a EUV-photoevaporating disk (figure from Alexander et al. 2006b [4]). Colour-coded to identify the three stages of evolution described in the text. Snapshots of the surface density are plotted at t = 0, 2.0, 4.0, 5.9, 6.0, 6.01, 6.02,...,6.18 Myr. At t = 6.20 Myr, the surface density is zero across the entire grid. After the inner disc is drained, direct photoevaporation disperses the outer disc very rapidly.

- *Gap-opening phase*: ($\lesssim 10^5$ yr). In this phase the (diffuse) photoevaporative wind cuts of the inner disc from re-supply. At this point the inner disk drains on its own, short, viscous timescale and an inner hole of few AU in radius is formed in the disk.

- *Clearing phase*: (few 10^5 yr). In this phase the inner disk is optically thin to ionizing radiation, and the disk is dispersed from the inside-out by the (direct) photoevaporative wind.

Thus, the UV-switch model naturally accounts for the lifetimes and dissipation timescales of disks as well as for SEDs of some pre-main sequence stars suggesting the presence of large inner holes. ([28] Calvet et al. 2002; [25] Bouwman et al. 2003; [47] Forrest et al. 2004; [36] D'Alessio et al. 2005).

More recent photoevaporation models, including also X-ray ([95] Owen et al. 2010) and/or FUV irradiation ([53] Gorti, Dullemond & Hollenbach 2009; [54] Gorti & Hollenbach 2009), show a similar qualitative behavior to photoevaporation by EUV alone. However, there are several important differences as X-rays and FUV photons are able to penetrate much larger columns of neutral gas than EUV photons, they are able to heat gas that is located both deeper in the disk and at larger radii. Thus, while EUV induced photoevaporation is restricted to the inner few AU of the disk, X-rays and FUV photons can operate at tens of AU from the star.

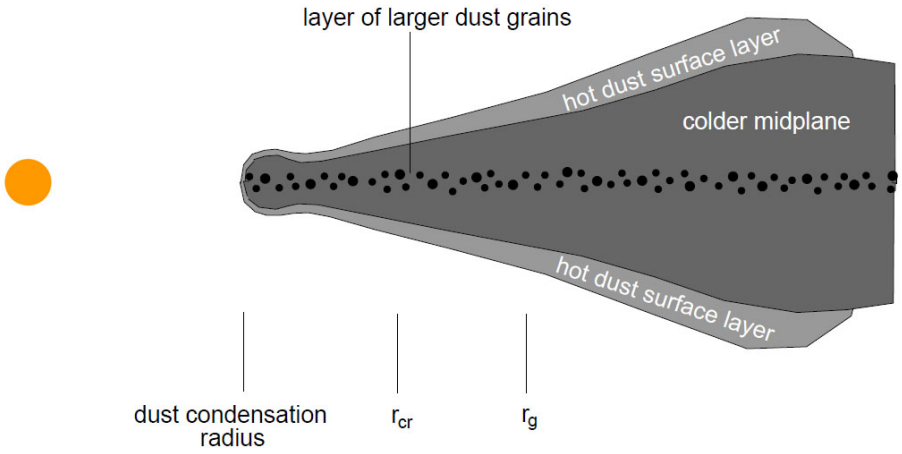

Figure 1.7: Scheme of the structure of a flaring protoplanetary disk (dust component). The radii R_g and R_{cr} are respectively the gravitational and critical radius as defined in Sec. 1.3.2.

1.4 Dust Grain growth and settling

Even though solid particles only represent 1% of the initial mass of the disk, understanding their evolution is fundamental for disk evolution and planet formation studies. Solids not only dominate the opacity of the disk, but also provide the raw material from which the terrestrial planets and the cores of the giant planets are made. Although viscous accretion and the photoevaporation processes discussed above drive the evolution of the gas, other processes operate on the solid particles, most importantly, grain growth and dust settling.

Grain growth and dust settling are intimately interconnected processes and represents the initial step toward planet formation. Gas motions differ slightly from Keplerian motions due to pressure. Small ($r \sim 0.1\mu m$) grains have a large surface-to-mass ratio and are swept along with the gas. As grains collide and stick together, their surface-to-mass ratio decreases and their motions decouple from the gas. They therefore suffer a strong drag force and settle toward the midplane. This increases the density of dust in the interior of the disk, which accelerates grain growth, and results in even larger grains settling deeper into the disk. If this process were to continue unimpeded, the end result would be a perfectly stratified disk with only small grains in the disk surface and large bodies in the midplane. However, because circumstellar disks are known to be turbulent, some degree of vertical stirring and mixing of grains is expected ([43] Dullemond & Dominik 2005). Collisions between particle is due by the fact that they are moving relative to one another. There are different sources of relative velocities in circumstellar disks: Brownian motion, v_{th}, sedimentation, v_s, and radial drift, v_r, turbulence-driven motion, v_{tur}.

A considerable ammount of work has been done to understand the physics of dust grain growth and sedimentation, including extensive numerical simulation on the topic, as well as dust coagulation studies in laboratories. Dullemond & Dominik

(2005) [43] investigated the dust coagulation process in circumstellar disks coupled to the settling and turbulent mixing of grains ignoring fragmentation and radial drift. They conclude that these processes are efficient enough to remove all small grains ($r < 100\mu m$) within 10^4 yrs. This is clearly inconsistent with the observational evidence showing the presence of micron sized grains throughout the duration of the primordial disk phase. The conclusion is that small grains must be replenished and that the persistence of small grains depends on a complex balance between dust coagulation and fragmentation ([44] Dullemond & Dominik 2008). Recent, more realistic models including fragmentation and radial drift confirm the necessity of grain fragmentation to explain the ubiquity of small grains in disks [22] Birnstiel, Ormel & Dullemond 2011; [26] Brauer, Dullemond & Henning 2008). These same models also confirm the severity of the problem known as the '*meter-size barrier*', a physical scale at which solids are expected to suffer both destructive collisions and removal through rapid inward migration ([116] Weidenschilling 1977). Even though several possible solutions have been proposed, including the formation of planetesimals in long-lived vortices (e.g., [57] Heng & Kenyon 2010), or via the gravitational instability of millimeter-sized chondrules in a gas deficient subdisk (e.g.,[123] Youdin & Shu 2002), overcoming this barrier remains one of the biggest challenges for planet formation theories ([32] Chiang & Youdin 2010).

1.5 Overview and aims of the thesis

In this thesis we study the structure and the emission properties at (sub-)mm wavelenghts of circumstellar disk around pre-main sequence stars. In particular, the main purpose is to investigated how the spatial variation of the dust opacity can influence the disk thermal and geometrical structure and so affect its emission properties. In order to reach this aim, we construct a circumstellar disk structure model which include the possibility to take into account (in parametric way) possible spatial variation of the grain size distribution and dust-to-gas ratio. Moreover we investigate if, a possible radial variation of a dust grain size distribution can be constrained comparing our two layer disk model, against spatially resolved multi-frequency observations at mm-wavelenghts

The thesis is organized as follow:

Chapter 2 give a general introduction of the models used to interprete the dust thermal emission from circumstellar disks which compute a self consistent disk structure. This overview is restricted primaly to circumstellar disk models aimed at a comparison with observation using a relative simple density distribution. So we are not intersted to those models which, for example, coupling the RT equation with the full HD or MHD equations. We will describe the density distributions and dust opacity models usually adopted and we will summarize the different numerical approaches often adopted to solve radiative transfer problem pointing out, for each one, its advantages and disasvantages.

Chapter 3 describes a new developed code which allow a self consistent compu-

tation of the structure of a steady passive thin disk in vertical hydrostatic equilibrium under the single annulus approximation (the so called 1+1Disk model). In order to compute a self-consistent thermal and geometrical disk structure the model numerically solve the hydrostatic equilibrium equation coupled to the radiative transfer equation in vertical direction. In particular the RT problem is solved with the Variable Eddington Factors (VEF) method which is been proved by [39] Dullemond et al. (2002) to be a fast and efficient method to find the solution of the radiative trasfer equation in circumstellar disk. In order to investigate the spatial variation of the dust opacity, the model include the possibility to have for each single radius and height in the disk a population of dust grains that can be different in terms of maximum grain size and dust-to-gas ratio. Using different (parametric) Rz-distribution for maximum grain size and dust-to-gas ratio the model predict change in the disk structure and dust continuum emission and so can be used to investigate the spatial variation of the dust property and try to constrain the grain growth and settling processes.

Chapter 4 describes a more semplified circumstellar disk model which allow, as the 1+1D model, a self consistent computation of the disk structure. This model solve the radiative transfer problem in simple way adopting the so called '*two layers*' approximation first proposed by [30] Chiang & Goldreich 1997. Using the capability of our two-layer model to have a radial variation of the dust properties, in particular, the possibility to modify the radial profile of the grain size distribution, we have used it to interpret observations at sub-millimiter and mm wavelenghts of disk around pre-main sequence stars.

Chapter 5 summarizes the main results discussed in the thesis and we discuss possible future developments.

Chapter 2

Overview of the models used to solve the structure of Circumstellar Disk

Contents

A self consistent disk structure model is required to interpret the dust thermal emission from circumstellar disks. The main objective of the models is the determination of the density and temperature structure of the disk. Such disk models have been developed and improve over many years and can operate at several levels, from simple vertically isothermal disk with power law radial temperature distribution (e.g., [16] Beckwith et al. 1990) to the more recent full time dipendent 3D (magneto/radiation) hydrodynamics (e.g., [50] Fromang & Papaloizou 2006, [51] Fromang S. & Nelson 2009). This last approach is obviosly very powerful as it include detailed physic, but it suffer for large computation cost and are so less pratical and often requires strong simplifying assumption in the radiative transfer to keep the problem tractable. We review in this chapter circumstellar disk models restricting primaly aimed at a comparison with observation. In Sec.2.1 we will describe the density distributions usually adopted for protoplanetary disk. In Sec.2.2 we will summarize the dust opacity models often used to describe the optical properties of circumstellar dust grain. We will then describe in Sec.2.3 the Radiative Transfer (RT) problem that has to be solved in order to compute the disk thermal structure and we will give a brief summary of the numerical approaches often adopted pointing out its advantages and disasvantages.

2.1 Disk Density Structure

In order to solve the stationary continuum RT equation (see Sec. 2.3) we need to specify the dust density distribution $\rho_d(\mathbf{x})$. As we already said, we are not intersted to those models which coupling the RT equation with the full HD or MHD equations, but to these one that solve the RT problem using a relative simple density distribution. Moreover it is usually assumed that the gas and dust are well mixed throughout the disk with a constant dust-to-gas ratio ($\rho_d/\rho_g = 0.01$).

One approach often used is to specify the gas surface density profile $\Sigma_g(R) = \int_{-\infty}^{+\infty} \rho_g(R,z)dz$ [1]. For a given $\Sigma_g(R)$ profile, the density distribution $\rho_g(R,z)$ can then be found integrating the vertical hydrostatic equilibrium equation:

$$\frac{\partial P_g(R,z)}{\partial z} = -\rho_g(R,z)g(R,z)_z \tag{2.1}$$

where P_g the gas pressure, g_z is the z component of the stellar gravity. A self consistent density structure can be found by iterating between the above equation and the RT equation ([92] Nomura 2002, [39] Dullemond 2002, [114] Walker et al. 2004). The simplest and very common approach is to use for $\Sigma_g(R)$ a truncated power law approximation

$$\Sigma_g(R) = \Sigma_0 \left(\frac{R_0}{R}\right)^p \qquad with \qquad R_{in} < R < R_{out} \tag{2.2}$$

where Σ_0 is the surface density at an arbitrary radius R_0 and R_{in},R_{out} are respectively the disk inner and outer radii. However this kind of distribution has no theoretical and abservational justification. Infact no disk accretion model (for isolated disk) predict disk structure with a sharp outer edge and morever this distribution fails to explain the differences in the radial extentions of the dust and the gas emission the are observed in a number disks around intermediate mass pre-main-sequance stars ([96] Piétu et al.2005; [65] Isella et al. 2007; [61] Hughes et al. 2008).

A more physical approach is to use one result of thin accretion disk. The key equation that describing the viscous evolution of a thin accretion disk is the diffusion equation for surface density (B.4) (see Appendix B for a brief review). It's well know that exist a series of analytic solutions (steady state and time-dependent solution) of this equation (B.4) that can be obtained assuming a given function for the viscosity ν. A time-dependent solution can be obtained in linear case assuming a power law approximation of the viscosity $\nu \prec R^\gamma$. In this case infact the Eq. (B.4) become linear and an analitic solution can be obtained ([81] Lynden-Bell & Pringle 1974):

$$\Sigma(\tilde{R},\tilde{t}) = \frac{C}{3\pi\nu_1\tilde{R}^\gamma}\tilde{t}^{\left[-\frac{(5/2-\gamma)}{(2-\gamma)}\right]}e^{\left[-\frac{\tilde{R}^{(2-\gamma)}}{\tilde{t}}\right]} \tag{2.3}$$

where C is a normalization constant, $\tilde{R} = R/R_1$ is the disk radius in units of radial scale factor R_1, $\nu_1 = \nu_1(R_1)$ is the disk viscosity at radius R_1, γ is the slope of the

[1] we use here a cylindrical (R,z) coordinate system

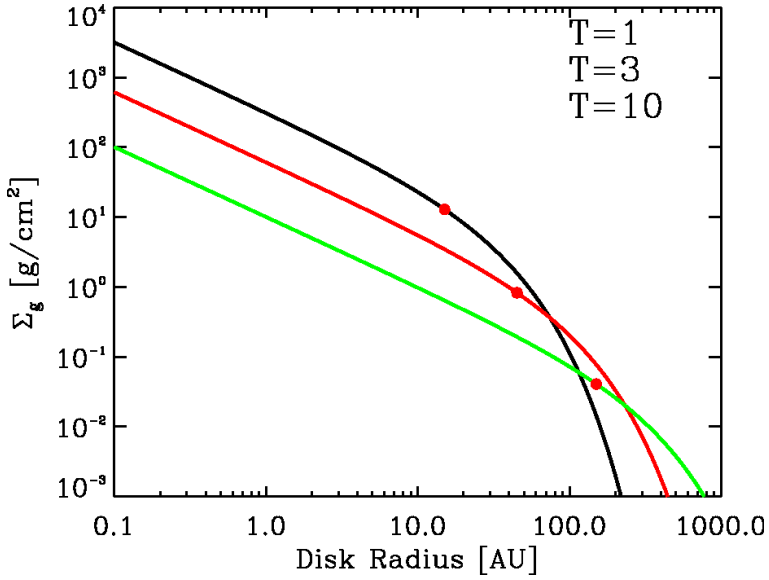

Figure 2.1: Evolution of the surface density according to Eq. (2.3) for $\gamma = 1$, $R_1 = 30AU$, $\nu_1 = 10^{15}$ and $C = 10^{17}$. The three lines show, from top to bottom, the self-similar solution at increasingly large times ($\tilde{t} = 1, 3, 10$, respectively). The red points correspond to the surface density at the transitional radius R_{tr} (see Appendix B for more details)

disk viscosity, $\tilde{t}$ is the non-dimensional time, $\tilde{t} = t/t_s + 1$, t is the age of the disk, and t_s is the viscous scaling time at the radius R_1 defined by $t_s = 1/[3(2-\gamma)^2]R_1^2/\nu_1$. How we can see, in contrast to the truncated power law, the disk has an outer edge that falling off exponentially and recent study ([61] Hughes et al. 2008; [66] Isella et al. 2009; [6] Andrews et al. 2009) have demostrated a more accurately reproducing the observed dust distribution in protoplanetary disks with respect to a power-law profile.

Another approach also used is to assume a given dust density distribution. Most applications ([122] Wood et al. 2002, [121] Wolf et al. 2003, [98] Pinte et al. 2008, [105] Sauter et al. 2009) have adopted, for example, the parametrized dust density distribution

$$\rho_d(R,z) = \rho_0 \left(\frac{R}{R_0}\right)^{\alpha} exp\left(-\frac{1}{2}\left(\frac{z}{h(R)}\right)\right) \tag{2.4}$$

where ρ_0 is the midplane density at $R = R_0$ and h the disk scale height

$$h(R) = h_0 \left(\frac{R}{R_0}\right)^{\beta} \tag{2.5}$$

where α, β and h_0 are the geometrical parameters.

2.2 Dust Opacity model

One important ingredient of a circumstellar disk model is the opacity distribution κ_ν. This quantity infact contribute to regulates the radiative transport and so controls the global energy redistribution throughout the disk. As the dust grains absorb radiation much more efficiently then the gas, they are the main source of opacity in the disk ([106] Semenov et al. 2003) and so they are usually assumed to be the only source of opacity ($\kappa = \kappa_{dust}$). Understand the dust opacity distribution presented in the disk is so essential to characterised their thermal and geometrical structure and consequently its emission properties.

The opacity of a population of dust grains depend on different properties (shapes, chemical compositions, porosity and sizes) of the grains ([87] Miyake & Nakagawa 1993; [99] Pollack et al. 1994; [37] Draine et al. 2006). To compute the dust opacity we need to specify the *dust efficiency* Q_ν and this is usually done, as we do, using the *Mie Theory* (see Appendix A.1 for a brief review). It is an exact theory based on classical electrodinamic for a continuum medium that can be applied at very idealized grain geometry. In the simpler case spherical grains are assumed. In order to determine the Mie coefficients a_n and b_n, the optical constant m of the grain material has to be specified (also called refractive index). This quantity is defined as

$$m = \sqrt{\varepsilon\mu} \tag{2.6}$$

where ε is the dielectric permeability and μ the magnetic permeability of the material. It is clear from the definition (2.6) that m contain information of the physical nature of the material and so describe the manner in wich a plane electromagnetic wave progresses through the material. The optical constant is a frequency dependent quantity (despite the denomination 'constant') and is a complex dimensionless number ($m_\nu = n_\nu + ik_\nu$) with real part n and imaginary part k. One online database of optical constant is the HJPDOC `(Heidelberg-Jena-St.Petersburg-Database of Optical Constants)` [2]. The database consists of tabulated data for several materials, each of one generally contain three columns: (1) wavelength or wavenumber, (2) real part n of the optical constant, (3) imaginary part k of the optical constant. In the case of a population of spherical grains of radius a with uniform chemical composition, the mass opacity coefficient κ_ν can be written

$$\kappa_\nu = \frac{\pi a^2 Q_\nu}{\frac{4\pi}{3}\rho_d a^3} = \frac{3}{4a}\frac{1}{\rho_d}Q_\nu \tag{2.7}$$

where ρ_d is the solid density of the grain and $3/4a$ is the geometrical cross section to volume ratio for particles for spheres.

During the evolution the dust grains are affected by different kind of processes which may take place in the disk, such as turbulence, settling, radial drift, etc. ([117] Weidenschilling 1989, [58] Henning & Stognienko 1996, [17] Beckwith, Henning & Nakagawa 2000) and the grain probabily become inhomogeney with porous

[2] http://www.mpia-hd.mpg.de/HJPDOC/

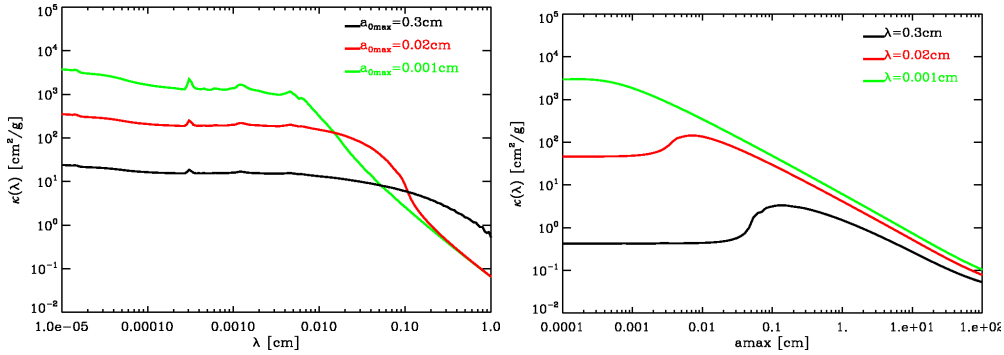

Figure 2.2: Mass opacity κ_ν of a population of composite particles with a power law size distribution (2.10) with $q = 3.0, a_{min} = 0.005\mu m$. The particles are made of (vol. perc.) 7% astronomical silicates, 21% carbonaceous material and 42% water ice and 30% vacuum. (*Left panel*) κ_ν in function of the wavelenght for 3 different maximum grains size. (*Right panel*) κ_ν in function of tha maximum grain size for 3 different wavelenghts.

structures. In this case the dielectic function within them varies from place to place ($\varepsilon = \varepsilon(\mathbf{x})$). The estimatation the optical properties of such composite particles is usually done using the *effective-medium theory* (EMT). The basic idea of the EMTs is to derive an effective dielettric function ε_{eff} representig the mixture as a whole i.e. an homogeneous grain with this dielectric function shall show the same characteristics in absorbtion and scattering as the original inhomogeneous particle. Two different approach are typically used: the Maxwell-Garnett approach ([85] Maxwell Garnet 1904) and the Bruggermann approach ([27] Bruggeman 1935) (see appendix A.2 for a brief review). Once determined, ε_{eff} is then used to derive the absorbtion efficiency of the grains $Q_{abs}(a, \nu)$ using the Mie theory. The effective optical constant $m_{eff} = n - ik$ to be used follow from $\varepsilon_{eff} = m^2_{eff}$. The mass opacity coefficient κ_ν for a population of composite grains can be written as in (2.7) with a dust density given by

$$\rho_d = \sum f_i \rho_i \tag{2.8}$$

where f_i and ρ_i are respectively the volume fraction and grain solid density of the i-esimo homogeneous component.

Coauglation and fragmentation processes in the disk will lead to a population of dust grain with a certain size distribution $n(a)$. One assume, usually, that $n(a)$ follows a truncated power law distribution:

$$n(a) \propto a^{-q} \quad with \quad a_{min} < a < a_{max} \tag{2.9}$$

where a_{min}, a_{max} are respectively the minimum and maximum grain size and q is the power law index. The mass opacity coefficient κ_ν for a population of grains with size distribution $n(a)$, can be written

$$\kappa(\nu) = -\frac{\pi \int n(a) a^2 Q_{abs}(a, \nu) da}{(4\pi/3)\rho_d \int n(a) a^3 da} \tag{2.10}$$

where ρ_d is the density of the composite dust grain. In figure 2.2 is shown, for a population of composite particles with a power law size distribution, the dust opacity distribution in function of the wavelenght (*left pannel*) and in function of the maximum grain size (*right pannel*).

2.3 The RT problem

Given the dust density structure and the specified the optical propertied of the dust grains, the RT problem can be solved. In this part lies the main complexity of the disk models and implement an efficient and relatively fast algoritm which is appropriated with the physical condition of the circumstellar disk is essential.

Solving the RT problem in a dusty circumstellar disk aims at determining the specific intensity $I(\nu, \mathbf{x}, \mathbf{n})$ of the radiation field at each point $\mathbf{x}$, direction $\mathbf{n}$ and frequency ν. This is achieved by solving the *stationary transfer equation*

$$\begin{aligned} \mathbf{n}\boldsymbol{\nabla}_x I(\nu, \mathbf{x}, \mathbf{n}) = &- [\kappa(\nu, \mathbf{x}) + \sigma(\nu, \mathbf{x})] I(\nu, \mathbf{x}, \mathbf{n}) \\ &+ \kappa(\nu, \mathbf{x}) B(\nu, T_d(\mathbf{x})) \\ &+ \frac{\sigma(\nu, \mathbf{x})}{4\pi} \int_\Omega p(\nu, \mathbf{n}, \mathbf{n}') I(\nu, \mathbf{n}, \mathbf{n}') d\Omega' \end{aligned} \tag{2.11}$$

where $\kappa(\nu, \mathbf{x})$ and $\sigma(\nu, \mathbf{x})$ are the absorbition and scattering coefficients (per volume unit). The quantity $p(\nu, \mathbf{n}, \mathbf{n}')$ denotes the probability that radiation is scattered from the direction $\mathbf{n}$' into $\mathbf{n}$, Ω is the solid angle, B_ν is the Plank function and T_d is the dust temperature.

Intensity and dust temperature are not indipendent. The radiation field determines the temperature and in turn, the dust re-emission contributes to the radiation field. This couples the partial differential RT equation to the *local energy balance equation* which can be write in as:

$$4\pi \int_0^\infty \kappa_\nu(z) B_\nu(T_d(\mathbf{x})) d\nu = 4\pi \int_0^\infty \kappa_\nu(z) J_\nu(\mathbf{x}) d\nu + Q(\mathbf{x}) \tag{2.12}$$

where Q is the absorbed energy (per volume element) from extra sources, like viscous heating or cosmic ray, and J_ν is the mean intensity defined as the average (over all solid angles) of the specific intensity

$$J_\nu(\mathbf{x}) = \frac{1}{4\pi} \int_\Omega I(\nu, \mathbf{x}, \mathbf{n}) d\Omega \tag{2.13}$$

The equation 2.12 describe how dust particles are heated to the temperature T_d such that the rate of energy absorbtion in a elementary volume (right side) is exactly balanced by the rate of energy emitted in the same volume (left side). The system of Eqs. 3.11, 3.12 and 3.49 completly defines the radiative transfer problem.

2.3.1 Numerical Methods

Over the last decade many dust continuum radiative trasfer programs and algorithms were developed to interpret the dust thermal emission from circumstellar disks. Numerical algorithms often used to solve the RT problem may be roughly classified in three categories: Monte Carlo methods, Discrete Ordinate methods and Angular Moment methods (the last two are also called grid-based methods as they are characterized by a discretization of also the photon propagation direction besides the spatial domain). Here we briefly present some basic concepts of these numerical techniques and point out its advantages and disadvantages.

2.3.1.1 Monte Carlo (MC) Methods

Monte Carlo (MC) methods solve the RT problem using a stocastic approach. The radiation field is partitioned in equal-energy, monocromatich 'photon packets' that are emitted stochastically by the radiation sources. The algorithm follow each individual 'photon packet' that propagate through the circumstellar enviroment until they exit the computation grid. The propagation process is governed by scattering, absorbtion and re-emission events that are controlled by the optical properties of the medium.

These methods have been applied for 2D-3D configuration in MC3D ([120] Wolf 2003), MCTRANSF ([91] Nicolini et al. 2003), RADMC ([42] Dullemond 2004), MOCASSIN ([89] Ercolano et al. 2003), TORUS ([59] Herries 2000), MCFOST ([97] Pinte et al 2006).

These methods have the advantage to be very flexible, since the concept of following photon packages is in principal applicable to arbitrary multidimentional configuration. Infact they can easily deal with complicated density distribution and arbitrary scattering and polarization. However, they have the drawback to presence random noise in the results and there is no global error control so one is never completely sure that a true solution has been reached. Moreover, it can become computationally expensive when the optical depth becomes very large as it is require a high number of photons to cover re-emission in all direction and this number increase with the optical depth.

2.3.1.2 Discrete Ordinate methods

Discrete Ordinate methods solve the RT equation using a deterministic approach. The solution is obtained using an iterative procedure that solve iteratively the RT equation and the local balance equation until the convergence criterio is reached. The two most used procedure are the ordinary '*Lambda Interaction*' (LI) and the '*Accelerator Lambda Interaction*' (ALI). The LI method first evaluate $I_\nu(\mathbf{x}, \mathbf{n})$ (Eq. 2.11), then $J_\nu(\mathbf{x})$ (Eq. 2.13) and finally $T(\mathbf{x})$ (Eq. 2.12) and iterate this procedure until convergene is reached. The ALI procedure, which converge faster, is a variant of the LI procedure, involving an approximate operatore Λ^*. Integration of the formal RT equation is often performed by using approach based on finite difference

scheme (like in STAINRAY) or by using the method of characteristics (like in RADICAL). Inoltre, different acceleration algorithms have been developed to speed up the iterative convergence to find the solution of the RT equation.

These methods have been developed mainly for line transfer, for which it has proven to be reasonably effective, and have not been widely used for dust continuum transfer. They have been applied in STAINRAY ([111] Steinacker et al. 2003), RADICAL ([40] Dullemond et al. 2002).

The Discrete Ordinate methods have the advantage to not involve random noise like in MC methods and provide an error control. However they are less flexible then MC and may be quite demanding. Moreovor, in optically thick regions they converges, like in MC, very slowly.

2.3.1.3 Angular Moment methods

Another type of deterministic algorithms to solve the RT problem are the *Angular Moment methods*. These methods solve the system of moments equation tuncated, usually at second order, with a closure relation (see Sec. 3.5 for more details). There is no easy way to formulate a closure relation. The simplest approach is to assume the so-called *diffusion approximation*. This approach has been applied, for example, by [34] D'Alessio et al. (1998), [84] Malbet et al. (2001). It has the advantage to solve the RT problem in a fast computation time. However, this approach is not applicable within optically thin regions, where the diffusion approximation is not valid anymore and the radiation field may significantly deviate from isotropy. For an accurate treatment a variable Eddington factor has to be calculated. This approach has been applied in RADICAL ([40] Dullemond et al. 2002) where the closure relation is obtained iteratively from the formal solution with the source function provided by the solution of the moment equations.

As the Discrete Ordinate methods, they have the advantage to not involve random noise and provide an error control. Moreover, they solve the RT problem from very low up to extremely high optical depths with only a few iterations (less then 10 usually). It converge, therefore, more quickly then the ALI procedure. However this approach is less flexible then MC and may be quite demanding.

Chapter 3

1+1D Disk Structure Model with spatial variation of dust property

Contents

In this chapter we present the 1+1D circumstellar disk models which allow a self consistent computation of the structure of a steady passive thin disk in vertical hydrostatic equilibrium under the single annulus approximation. In order to solve a self-consistent thermal and geometrical disk structure the model numerically solve the hydrostatic equilibrium equation coupled to the radiative transfer equation in vertical direction. Moreover, it include the possibility to have for each single radius and height in the disk a population of dust grains that can be different in terms of maximum grain size and dust-to-gas ratio. Using different (parametric) Rz-distribution for maximum grain size and dust-to-gas ratio the model predict change in the disk structure and dust continuum emission and so can be used to investigate the spatial variation of the dust property and try to constrain the grain growth and settling processes.

The chapter is organized as follow: In Sec. 3.1 we introduce the 1+1D disk structure model. In Sec. 3.2 we show the iterative procedure adopted in order to have a disk in vertical hydrostatic equilibrium. In Sec. 3.3 we analyse the two basic equations '*Radiative Trasfer equation*' and '*Hydrostatic Equilibrium equation*' we need to solve in order to compute a self consistent disk structure. In Sec. 3.4 we discuss how we solve the extintion of the primary stellar radiation using the so called '*irradiation-angle description*'. In Sec. 3.6 we present the '*Variable Eddington Factor*' (VEF) method we use to solve the RT problem. In Sec. 3.7 we show the adopted (paramteric) distribution for the dust-to-gas ratio η and maximum grain size a_{max}. In Sec. 3.8 we show how we compute the observable: SED and emission map. In Sec. 3.9, 3.10 we illustrate the basic results of the annulus structure calculation of a fiducal annulus model and we show how different $\eta(z)$ and $a_{max}(z)$ distribution, affect the structure and emission properties of the annulus. In Sec. 3.11, 3.12 we illustrate the basic results of the disk structure calculation of a fiducal disk model and we show how the different $\eta(R,z)$ and $a_{max}(R,z)$ distribution, affect the structure and emission properties of the disk.

3.1 Introduction: The $1+1$D Disk Model

Since the initial models of viscous accretion disks by [107] Shakura & Sunyaev (1973) and [81] Lynden-Bell & Pringle (1974), the physics of the close environment of T Tauri stars (TTS) has been extensively studied in order to interpret their spectral energy distribution (SED). For the sake of simplicity, models traditionally separated disks into two categories, sometimes called *active disks*, on one hand, in which viscous dissipation is predominant, and *passive disks*, on the other hand, for which irradiation by the central star is the main heating process. Early models used quasi-Keplerian steady accretion disks, assumed to be geometrically thin for a wide range of accretion rate; they predicted a fixed slope for the infrared spectrum: $\lambda F_\lambda \sim \lambda^{-4/3}$. However many TTS present flatter SEDs, and disk flaring was among the first attempts to explore disk vertical structure as an explanation for such SED

flattening ([1] Adams et al. 1987; [71] Kenyon & Hartmann 1987): in a *flared disk*, the disk opening angle (or the ratio between the scale height and the radius) increases toward the outer disk. The grazing angle at which the stellar radiation impinges on the disk changes with radius allowing for an increase of the heating of the outer regions of the disk. Since then, several models have been proposed in order to explain both standard SEDs and flatter ones.

The detailed vertical structure of a circumstellar disk can be computed by solving the equations of vertical pressure balance coupled to the equation of radiative transfer. An analytical study of the radiative transfer in vertical structure of disks was first carried out by [60] Hubeny (1990) for active disks, by [83] Malbet & Bertout 1991 for passive disks. Later on, [30] Chiang & Goldreich (1997) used a simplified two-layer passive disk model based on the same super-heating mechanism and derived SEDs, confirming conclusions of Malbet & Bertout 1991 and producing results consistent with observations. Malbet et al. 2001 [84], then, generalized to disks heated by several processes.

On the other hand, numerical integration of the equations of radiative transfer was carried out by varius authors in order to derive the vertical structure of accretion disks. [18] Bell & Lin (1994); [19] Bell et al. (1997) developed an active disk model in order to explain FU Orions outbursts; [34, 35] D'Alessio et al. 1998, 1999 dealt with the more general case solving the complete 1+1D disk structure solving the radiative transfer in diffusion limit approximation both by viscous heating and stellar irradiation. [40] Dullemond et al. 2002 apply exact 1D wavelenght-dependent radiative transfer for the vertical structure.

All these models cited above, compute the vertical structure adopting the so called *single annulus approximation*: i.e. the disk is considered as a set of concentric cylinders of infinitesimal width. Each cylinder is itself regarded as a plane-parallel atmosphere of dust and gas layer each assumed to be indipendent of the other and costituite an indipendent 1D vertical radiative transfer problem. The basic assumption is that the radial transfer of energy is smaller then the vertical transfer.

3.2 Iterative procedure to reach vertical hydrostitic equilibrium

In order to compute a self-consistent temperature and density distribution of a disk in hydrostatic equilibrium we adopt an iterative procedure where we recomputed iteratively the disk structure until the gas density profile converge. From the inner radius R_{in} to the outer radius R_{out}, we solve at each annulus (up to the deplection height z_{depl} [1]) the following sequence of steps (Fig. 3.1):

1. We compute the local ammount of energy $Q(R, z)$ that the stellar radiation release on the dust grains using the *irradiation-angle description*' (Sec. 3.4)

[1] The dust deplection height is set by the $a_{max}(R, z)$ distribution, i.e. corrispond to the height z where the maximum grain size reach the minimum size

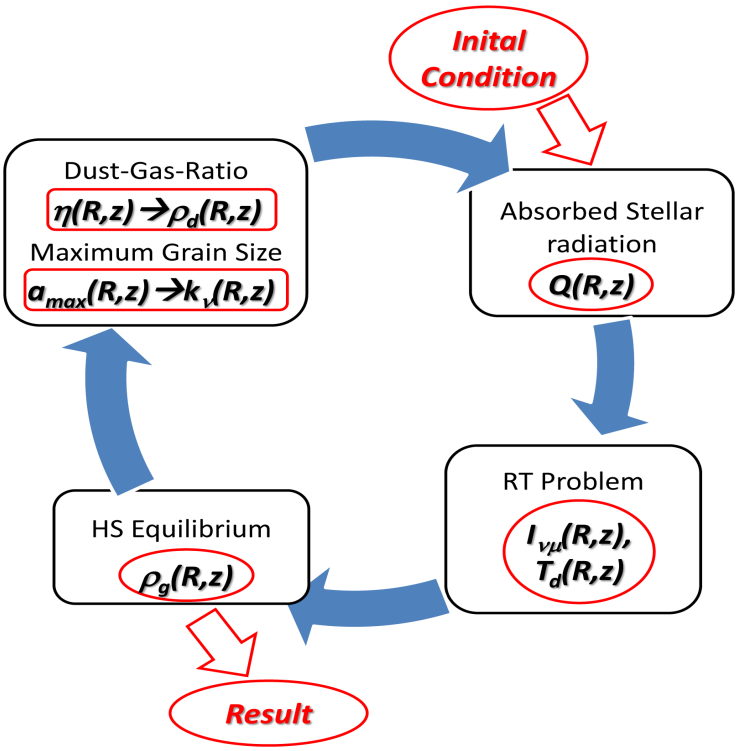

Figure 3.1: Scheme of the adopted iterative procedure to reach the vertical hydrostatic equilibrium.

where the angle $\alpha_{irr}(R)$ at which the stellar radiation incide on the surface height $z_s(R)$ is determined.

2. We compute the dust thermal structure $T_d(R,z)$ of the disk solving the 1D vertical radiative trasfer problem using the '*Variable Eddington Factor*' (VEF) method as described in Sec. 3.5.

3. Once we found the dust temperature stratification, we solve the vertical hydrostatic equilibrium equation (Sec. 3.3.2) (assuming gas and dust in thermal equilibrium $T_g = T_g$) in order to find the gas density structure $\rho_g(R,z)$ at which corrispond a new pressure heigh $H_p(R)$.

4. The new pressure height $H_p(R)$ is used to compute:

   (a) The dust-to-gas ratio $\eta(R,z)$ (Eq. 3.71) from which we can compute a new dust density structure $\rho_d(R,z)$.

   (b) The maximum grain size $a_{max}(R,z)$ (Eq. 3.71) from which we can compute a new dust opacity structure $k_\nu(R,z)$ (Eq. 2.10)

   From $\rho_d(R,z)$ and $k_\nu(R,z)$ we can then compute the new surface height $z_s(R)$ (Eq. 3.47) which will be used to determinate the incidente angle $\alpha_{irr}(R)$.

It should be noted that $H_p(R)$ can slightly vary throughout the iteration procedure and so the $k_\nu(R,z)$ and $\rho_d(R,z)$ distribution will be different respect to the initial configuration when the convergence criterio is reached.

Once obtained the entire structure of the disk we compare the new gas density distribution with that of the previews iteration and we iterate the entire procedure until a converged solution for $\rho_g(R,z)$ is reached i.e. when the relative difference in density between successive iterations drops below the convergence criterio

$$\max_{\substack{0\leq i\leq n_R-1\\ 0\leq j\leq n_z-1}} \left(\frac{|\rho_g^{old} - \rho_g^{new}|}{\rho_g^{old} + \rho_g^{new}} \right) < 10^{-2} \tag{3.1}$$

3.2.1 Initial condition

We solve the iterative procedure described above, departe from a simple *initial configuration*, corrisponding to a vertically isothermal thin disk in hydrostatic equilibrium. In this case the pressure balance equation (3.30) can be easily integrate (see Sec. 4.2.1) leading to a gas density distribution with a vertical gaussian profile:

$$\rho_g(R,z) = \frac{\Sigma_g(R)}{\sqrt{2\pi}H_p(R)} exp\left(-\frac{z^2}{2H_p(R)^2}\right) \tag{3.2}$$

where $\Sigma_g(R)$ is the gas surface density distribution and the quantity $H_p(R)$ denotes the pressure scale height of the gas given by

$$H_p(R) = \frac{c_s(R)}{\Omega_k(R)} \tag{3.3}$$

where $\Omega_k(R) = \sqrt{GM_\star/R^3}$ is the local angular velocity, $c_s(R) = \sqrt{k_B T_g(R)/\mu m_p}$ is the isothermal sound speed, k_B and G are the Boltzman constant and the gravitational constant,respectively, μ_g is the mean molecular weight, m_p is the mass of a proton and $T_g(R)$ is the gas temperature profile. For the initial temperature we use a simple profile corrisponding to the midplane temperature of a disk irradiated under a constant flaring angle of $\alpha_{irr}(R) = 0.05$. By equating the irradiation flux $F_{irr} = \alpha_{irr} L_\star/(4\pi R^2)$ to the cooling flux $F_{cool} = \sigma_s T(R)^4$ one can solve directly for $T(R)$, obtaining:

$$T_g(R) = \alpha_{irr}^{1/4} \sqrt{\frac{R_\star}{R}} T_\star \tag{3.4}$$

where $L_\star$, $R_\star$, and $T_\star$ are respectively the luminosity, radius and effective temperature of the central star. Given the pressure height $H_p(R)$, the initial dust-to-gas ratio $\eta(R,z)$ and maximum grain size $a_{max}(R,z)$ are given respectively by Eqs. 3.70 and 3.71 from which we can then compute respectively the initial dust density structure $\rho_d(R,z)$ and the initial dust opacity structure $k_\nu(R,z)$ (Eq. 2.10).

3.3 Basic Equations and adopted assumptions

In this section we analyse the two basic equations '*Radiative Trasfer equation*' and '*Hydrostatic Equilibrium equation*' that we need to solve in order to compute the disk structure. This equations will be solved under a certain number of assumptions and semplifications which will allow us to simplify the problem.
As we are in single annulus approximation, we will confine our attention exclusively to a *plane parallel geometry* (Fig. 3.2). In this case the intensity of the radiation field is function of the frequency ν, the height z in the direction normal to the plane of stratification and the polar angle θ i.e the angle between a ray and z-direction ($\mu = cos\theta$).

3.3.1 1D RT Problem in a plane-parallel dusty medium

Solving the RT problem in a plane-parallel dusty medium, aims at determining the specific intensity $I(\mu, \nu, z)$ of the radiation field at each hight z, frequency ν and direction μ. Starting with the boundary value, one can calculate this intensity in the considered domain by solving the 1D vertical stationary transfer equation

$$\underbrace{\mu \frac{dI(\mu,\nu,z)}{dz}}_{\substack{\text{variation of } I_\nu \\ \text{along a direction } \mu}} = \underbrace{-\chi(\nu,z) I(\mu,\nu,z)}_{\substack{\text{extintion} \\ \text{by matter}}} \underbrace{+ \quad \varepsilon(\nu,z)}_{\substack{\text{re-emission} \\ \text{by matter}}} \tag{3.5}$$

where $\chi(\nu, z) = \kappa(\nu, z) + \sigma(\nu, z)$ is the extinction coefficient (per unit of volume) given by the sum of the pure absorbtion κ and scattering σ coefficients (in general due to both dust grains and gas species) and $\varepsilon(\nu, z)$ is the emission coefficient. The Eq. 3.5 show that, for each direction, the intensity I_ν (per unit lenght) decrease by an amount $\chi_\nu I_\nu$ and increase by ε_ν. The RT equation is usually written in term of the source function $S_\nu = \varepsilon_\nu / \chi_\nu$. In this way the (3.5) become:

$$\mu \frac{dI_{\mu,\nu}(z)}{dz} = \chi_\nu(z) \left(S_\nu(z) - I_{\mu,\nu}(z)\right) \tag{3.6}$$

The source function describe how photons originally traveling with the beam are removed and replaced by photons from surrounding matter. For example, for a dusty medium with grains at temperature T_d and assuming isotropic scattering, the source function can be written

$$S_\nu = \frac{\kappa_\nu B_\nu(T_d) + \sigma_\nu J_\nu}{\chi_\nu} \tag{3.7}$$

where J_ν is the mean intensity of the radiation field (Eq. 3.49). In more general case, the knowledgment of this function can require complex calculation.

To solve the equation (3.6) we make a certain number of assumptions. We focus on the solution for continuum dust emission neglecting therefore the gas contribution

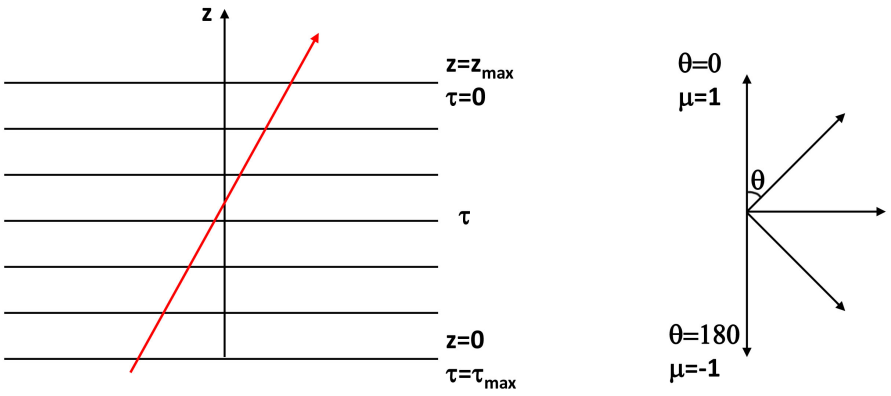

Figure 3.2: Schematic illustration of an annulus described as a plane parallel dusty medium. Note that there are inward ($\mu < 0$) and outward ($\mu > 0$) directed streams of radiation. The boundary conditions necessary for the solution are specified at the top of the annulus ($\tau = 0$) and at the midplane ($\tau = \tau_{max}$).

and its emission lines and for semplicity we also ignore the scattering opacity. In this way the extintion is due only to the continuum absorbtion by dust grains

$$\chi_\nu(z) = \kappa_\nu^{dust}(z) \tag{3.8}$$

We make, moreover, the assumption of local thermodynamic equilibrium (LTE) condition. According the Kirchhoff-Plank relation in this case the grain emission is only a function of dust temperature and is given by $\varepsilon_\nu = \kappa_\nu B_\nu(T_d)$; therefore the source function is identical to the Planck function

$$S_\nu(z) = B_\nu(T_d(z)) \tag{3.9}$$

Under the assumption of LTE, all the dust grains of each size have the same temperature T_d at each position. The RT equation (3.6) can then be writen in LTE as:

$$\mu \frac{dI_{\mu,\nu}(z)}{dz} = \rho_d(z) k_\nu(z) \left(B_\nu(T_d(z)) - I_{\mu,\nu}(z)\right) \tag{3.10}$$

where we have considered the opacity coefficient k_ν (per unit of matter) ($\kappa_\nu = \rho_d k_\nu$ where ρ_d is the dust density). So in our case to solve the RT equation we need to calculate the dust temperature.
Regarding the source function S_ν and the opacity κ_ν as given functions, the Eq. 3.10 is a linear first order differential equation and it's possible provide the so called '*formal solution*':

$$I_{\mu,\nu}(z) = I_\nu(z_0) e^{-\Delta\tau_\nu} + \int_0^{\Delta\tau_\nu} S(\tau'_\nu) e^{-(\Delta\tau_\nu - \tau'_\nu)} d\tau'_\nu \tag{3.11}$$

where $\Delta\tau_\nu$ is the optical depth difference between z_0 and z.

Intensity and dust temperature are not indipendent. The radiation field determines the temperature and in turn, the dust re-emission contributes to the radiation field. This couples the partial differential RT equation to the *local energy balance equation* which can be write in LTE as:

$$\underbrace{4\pi \int_0^\infty \rho_d(z) k_\nu(z) B_\nu(T_d(z)) d\nu}_{\substack{\text{energy emitted by} \\ \text{volume element}}} = \underbrace{4\pi \int_0^\infty \rho_d(z) k_\nu(z) J_\nu(z) d\nu \quad + \quad Q(z)}_{\substack{\text{energy absorbed by} \\ \text{volume element}}} \tag{3.12}$$

where Q is the absorbed energy (per volume element) from extra sources and J_ν is the mean intensity defined as the average (over all solid angles) of the specific intensity

$$J_\nu(z) = \frac{1}{2} \int_{-1}^{1} I_{\mu,\nu}(z) d\mu \tag{3.13}$$

The equation (3.12) describe how dust particles are heated to the temperature T_d such that the rate of energy absorbtion in a elementary volume is exactly balanced by the rate of energy emitted in the same volume. As other sources of energy, we consider only the direct stellar radiation (see Sec. 3.4). If there is extra source of energy then the radiation, like viscous heating or cosmic ray, this can be easly included by adding the corresponding term on the right hand side of balance equation. The system of Eqs. 3.11, 3.12 and 3.13 completly defines the radiative transfer problem.

3.3.2 Vertical Hydrostatic equilibrium

Under the assumption that the radiation pressure and the magnetic field do not influence the disk structure, the physical quantities describing the gas component of the disk (ρ_g, P_g, $\mathbf{u}_g$) must satisfy the equations of viscous fluid dynamics:

$$\frac{\partial \rho_g}{\partial t} + \boldsymbol{\nabla} \cdot (\rho_g \mathbf{u}_g) = 0 \quad \textit{(Mass conservation)} \tag{3.14}$$

$$\rho_g \left[\frac{\partial \mathbf{u}_g}{\partial t} + (\mathbf{u}_g \cdot \boldsymbol{\nabla}) \mathbf{u}_g \right] = -\boldsymbol{\nabla} P_g + \boldsymbol{\nabla} \cdot \sigma - \rho_g \boldsymbol{\nabla} \Phi \quad \textit{(Equation of motion)} \tag{3.15}$$

$$\left(\frac{\partial}{\partial t} + \mathbf{u}_g \cdot \boldsymbol{\nabla} \right) \left(P_g \rho_g^{-\gamma} \right) = 0 \quad \textit{(Energy Equation)} \tag{3.16}$$

where ρ_g is the gas density, P_g the gas pressure, Φ the gravitational potential and σ is the stress tensor describing the effect of viscous forces. Here we limit ourself to a steady state disk wherein all quantities are independent of time ($\frac{\partial}{\partial t} = 0$). The equation to solve are then:

$$\boldsymbol{\nabla} \cdot (\rho_g \mathbf{u}_g) = 0 \tag{3.17}$$

$$\rho_g (\mathbf{u}_g \cdot \boldsymbol{\nabla}) \mathbf{u}_g = -\boldsymbol{\nabla} P_g + \boldsymbol{\nabla} \cdot \sigma - \rho_g \boldsymbol{\nabla} \Phi \tag{3.18}$$

$$(\mathbf{u}_g \cdot \boldsymbol{\nabla}) \left(P_g \rho_g^{-\gamma} \right) = 0 \tag{3.19}$$

We assume that the gravity is dominated by the central star (disk self-gravity negligible). In this way the gravitational potential $\Phi(R,z)$ is simply given by

$$\Phi = -\frac{GM}{(R^2+z^2)^{1/2}} \tag{3.20}$$

We suppose then an axisymmetric disk where the physical quantities do not change if we move along the direction of rotation. It's so convenient to use a *cylindrical polar coordinate system* with origin at the center of the disk and with the axis z coincident with the axis of symmetry. In this way the variables describing the system are not functions of the azimuthal coordinate ϕ ($\frac{\partial}{\partial\phi}=0$) but depend only on R e z. The equations 3.17, 3.18 and 3.19 written in components are:

$$\frac{1}{R}\frac{\partial}{\partial R}(\rho_g R u_R) + \frac{\partial}{\partial z}(\rho_g u_z) = 0 \tag{3.21}$$

$$(\mathbf{u}_g\cdot\boldsymbol{\nabla})u_R - \frac{u_\phi^2}{R} = -\frac{1}{\rho_g}\frac{\partial P_g}{\partial R} + \frac{1}{\rho}\left[\boldsymbol{\nabla}\cdot\sigma\right]_R - \frac{\partial\Phi}{\partial R} \tag{3.22}$$

$$(\mathbf{u}_g\cdot\boldsymbol{\nabla})u_\phi + \frac{u_R u_\phi}{R} = \frac{1}{\rho_g}\left[\boldsymbol{\nabla}\cdot\sigma\right]_\phi \tag{3.23}$$

$$(\mathbf{u}_g\cdot\boldsymbol{\nabla})u_z = -\frac{1}{\rho_g}\frac{\partial P_g}{\partial z} + \frac{1}{\rho_g}\left[\boldsymbol{\nabla}\cdot\sigma\right]_z - \frac{\partial\Phi}{\partial z} \tag{3.24}$$

$$(\mathbf{u}_g\cdot\boldsymbol{\nabla})\left(P_g\rho_g^{-\gamma}\right) = 0 \tag{3.25}$$

where:

$$\mathbf{u}_g\cdot\boldsymbol{\nabla} = u_R\frac{\partial}{\partial R} + u_z\frac{\partial}{\partial z} \tag{3.26}$$

We assume, moreover, a geometrically thin disk, i.e. the disk flow is very confined to the midplane. This means that the typical length in the vertical direction, the disk thickness H, is much smaller that the radial distance R:

$$H << R \tag{3.27}$$

This approximation allow us to simplify the equations to solve:

1. The stress tensor σ can be assumed to be given by classical shear viscosity so that the only non-vanishing component of σ is the $R\phi$ component, proportional to the rate of strain $R\Omega'$

$$\sigma_{R\phi} = \rho_g \nu R\frac{d\Omega}{dR} \tag{3.28}$$

2. There is essentially no flow in z-direction and so all the velocity terms in this direction can be neglected

3. The R and z component of the gravitational field become:

$$\begin{aligned} g_R &= -\frac{\partial\Phi}{\partial R} \approx -\frac{GM}{R^2}\left(1-\frac{3}{2}\frac{z^2}{R^2}\right) \approx -\frac{GM}{R^2} \\ g_z &= -\frac{\partial\Phi}{\partial z} \approx -\frac{GMz}{R^3}\left(1-\frac{3}{2}\frac{z^2}{R^2}\right) \approx -\frac{GMz}{R^3} \end{aligned}$$

4. The radial pressure gradient can be neglected with respect to the other force in radial direction. In this way the equation of radial hydrostatic equilibrium (3.22) is reduced to:

$$-\frac{u_\phi^2}{R} = -\frac{GM}{R^2}$$

which express the condition of centrifugal balance (i.e. the radial component of the gravitational force is balance by the centrifugal force). This lead to a azimutal gas velocity to be keplerian:

$$v_\phi = v_K = \left(\frac{GM}{R}\right)^{\frac{1}{2}} \quad \text{o} \quad \Omega = \Omega_K = \frac{(GM)^{\frac{1}{2}}}{R^{\frac{3}{2}}} \tag{3.29}$$

In order to verify this assumption we can do a dimensional analysis of the hydrostatic equations. If we indicate with H and R the typical vertical and radial disk scales and assuming an isothermal relation $P \sim c_s^2\rho$ where c_s is the isothermal sound speed, the equation (3.24) give us:

$$\frac{c_s^2}{H} \cong \frac{GMH}{R^3} \qquad \Longrightarrow \qquad c_s << \left(\frac{GM}{R_\star}\right)^{1/2}$$

This means that the keplerian azimutal gas velocity of a thin disk is highly supersonic. Doing now the ratio between the pressure term and gravitational term of the equation (3.22) we obtain:

$$\frac{c_s^2/R}{GM/R^2} \backsimeq \frac{c_s^2}{\frac{GM}{R}}$$

which is very small and it allowed us to neglect the radial pressure gradient with respect to the other forces in radial direction. In conclusion, in the thin disk approximation we have that the azimuthal velocity is keplerian and highly supersonic.

Under our assumptions, the gas density distribution $\rho_g(R,z)$ can be then obtained solving the pressure balance equation:

$$\frac{1}{\rho_g(R,z)}\frac{\partial P_g(R,z)}{\partial z} = -\frac{GMz}{R^3} \tag{3.30}$$

To solve the Eq. 3.30 we relate P_g,ρ_g and T_g through the equation of state of an ideal gas:

$$P_g(R,z) = \frac{\rho_g(R,z)k_BT_g(R,z)}{\mu m_H} \tag{3.31}$$

where $k_B \simeq 1.38\times10^{-16}\text{ergK}^{-1}$ is the Boltzman constant, $m_H \sim m_p \simeq 1.67\times10^{-24}\text{g}$ is the mass of the hydrogen atom and μ is the mean molecular weight ($\mu = 2.3$ for H_2,He misture). In this way the equation to solve can be written:

$$\frac{dlog\rho_g}{dz} = -\left[\frac{az}{T_g} + \frac{dlogT_g}{dz}\right] \tag{3.32}$$

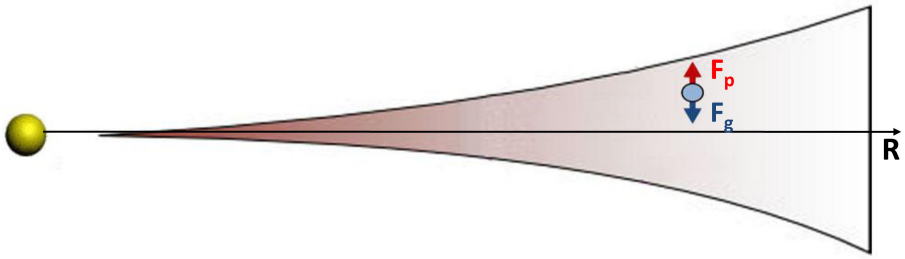

Figure 3.3: Balance of forces (pressure $F_p = \partial P_g/\partial z$ and gravitational force $F_g = \rho_g GMz/R^3$) acting on an element of gas in a thin disk in vertical HS equilibrium.

where $a = GM\mu m_H/kR^3$. In order to solve this equation and compute the gas density distribution $\rho_g(R,z)$, we need to know the gas thermal structure $T_g(R,z)$. To do this we compute the dust temperature $T_d(R,z)$ resolving the continuum radiative transfer (Sec. 3.5) and we assume that the gas and the dust are in thermal equilibrium ($T_d = T_g$). The Eq. 3.32 is a 1D ordinary differential equation and we straight integrate from the midplane up to z_{depl} using the forward Euler method. We take an arbitrary value for the midplane density $\rho_g(R,0)$ and we integrate obtaining the density distribution $\tilde{\rho}_g(R,z)$. Then we renormalize this resulting profile to the input gas surface density $\Sigma_g^{INPUT}(R)$.

$$\rho_g(R,z) = \tilde{\rho}_g(R,z) * \frac{\Sigma_g^{INPUT}(R)}{\tilde{\Sigma}_g(R)} \tag{3.33}$$

where

$$\tilde{\Sigma}_g(R) = 2\int_0^{\infty} \tilde{\rho}_g(R,z)dz \tag{3.34}$$

As our calculation go up to z_{depl} we actually renormalize the solution to the input dust surface density. As $(\Sigma_g/\Sigma_d)^{INP} = \tilde{\Sigma}_g/\tilde{\Sigma}_d$, we can rewrite the (3.33)

$$\rho_g(R,z) = \tilde{\rho}_g(R,z) * \frac{\Sigma_d^{INPUT}(R)}{\tilde{\Sigma}_d(R)} \tag{3.35}$$

where

$$\tilde{\Sigma}_d(R) = 2\int_0^{z_{depl}} \eta(R,z)\tilde{\rho}_g(R,z)dz \tag{3.36}$$

3.4 Extintion of the primary stellar radiation

The first problem to solve, in our iterative procedure, is the extintion process of the primary stellar photons, when they enter into the disk and get absorbed by the dust. This is modelled using a *irradiation-angle description* ([30] Chiang e Goldrich 1997) in which the amount of stellar radiation energy absorbed by the dust is determined by solving the vertical plane-parallel radiative transfer (pure absorbtion without

emission $\varepsilon_\nu = 0$) with the radiation entering the disk under an angle $\alpha_{irr}(R)$ with respect to the disk's surface height $z_s(R)$. For each annulus we need then to solve the RT equation (3.10) without source function ($S_\nu = 0$) and for the photon propagation direction $\mu = cos\theta \sim \alpha$ (due to the typical shallow incidente angle $\alpha \ll 1$) which give the solution

$$I_{\mu,\nu}(z) = I_{0,\nu} e^{-\tau_\nu(z)/\alpha} \tag{3.37}$$

where $I_{0,\nu}$ is the stellar incident intensity at the considered radius R and τ_ν is the vertical optical depth

$$\tau_\nu(z) = \int_z^\infty \rho_d(z) k_\nu(z) dz \tag{3.38}$$

The incident intensity is then reduced by a factor of $e^{-(\tau_\nu(z))/\alpha}$ when it passes throght the annulus. In term of flux we have

$$F_\nu(z) = \frac{L_\nu}{4\pi R^2} e^{-\tau_\nu(z)/\alpha} \tag{3.39}$$

where L_ν is the stellar luminosity. Once the function $F_\nu(z)$ is known, one can compute, from the local energy conservation equation (3.12), the amount of energy absorbed by the dust grains from the primary stellar radiation

$$Q(z) = \int_0^\infty \rho_d(z) k_\nu(z) F_\nu(z) d\nu \tag{3.40}$$

3.4.1 Incidente angle of a flared disk

The fraction of the primary stellar radiation entering in the disk, at each radius, depend on the value of the incidente angle $\alpha_{irr}(R)$ with respect to the disk's surface; larger the incidence angle, greater is the amount of stellar radiation energy absorbed by the dust. Let's compute this incidente angle starting to consider a flat and thin disk or a disk with a constant H/R. A disk surface element of unit area receives out of the solid angle $d\Omega$ pointing towards the star the flux $B_\nu(T_\star) d\Omega sin\theta sin\phi$ (figura 3.4). By the whole upper half of the star, the surface element is illuminated by the flux

$$F_\nu = B_\nu(T_\star) \int_0^{\theta_{max}} sin^2\theta d\theta \int_0^\pi sin\phi d\phi = B_\nu(T_\star) \left[\theta_{max} - \frac{1}{2} sin2\theta_{max}\right] \tag{3.41}$$

$$= B_\nu(T_\star) \left[\arcsin \frac{R_\star}{R} - \frac{R_\star}{R}\sqrt{1 - \left(\frac{R_\star}{R}\right)^2}\right] \tag{3.42}$$

We express F_ν through an effective incidente angle, α_{irr}^{flat}, defined by

$$F_\nu = B_\nu(T_\star) \cdot \Omega_\star \cdot \alpha_{irr}^{flat}$$

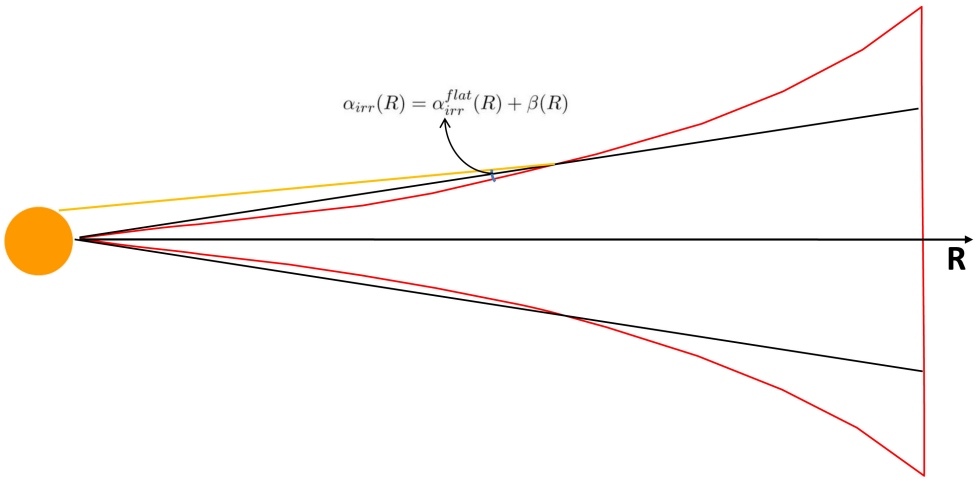

Figure 3.4: Incidente angle of the stellar photons on the disk's surface for a H/R constant disk (black line) and for a flared disk (red line). On the flared disk the incidente angle α_{irr} of the stellar light is enhanced with respect to the H/R constant disk by $\beta = \alpha_{irr} - \alpha_{irr}^{flat}$

where $\Omega_\star$ is the solid angle of the star. At large distances ($x \equiv R_\star/R << 1$) we can use the approximation [$\arcsin x - x\sqrt{1-x^2} \simeq 2x^3/3$] and [$\Omega_\star = \frac{\pi}{2}\frac{R_\star^2}{R^2}$]. In this way the incidente angle is simply given by

$$\alpha_{irr}^{flat}(R) \approx \frac{4}{3\pi}\frac{R_\star}{R} \tag{3.43}$$

How we can see, for a flat or H/R constant disk, the incidente angle decresce with the distance from the star.

In a keplerian disk, when the gas is in hydrostatic equilibrium in the z-direction, the pressure height H_p increases with the distance R from the star (Eq. 3.3). The disk is said to be *flared* (figura 3.4). Assuming that the gas and dust are well mixed, the dust disk is then not flat nor is the ratio H_p/R constant. In this case the incidente angle of the stellar photons is enhanced with respect to the flat disk:

$$\alpha_{irr}(R) = \alpha_{irr}^{flat}(R) + \beta(R)$$

This enhanced β is derived adopting, as disk's surface, the $\tau = 1$ surface (H_s) (see Sec. 3.4.2). In this way is possible to write β as

$$\beta(R) = \arctan\frac{dH_s}{dR} - \arctan\frac{H_s}{R} \approx \frac{dH_s}{dR} - \frac{H_s}{R} = R\frac{d}{dR}\left(\frac{H_s}{R}\right) \tag{3.44}$$

In coclusion, the incidente angle of the stellar photons on a flared disk is

$$\alpha_{irr}(R) \approx \frac{4}{3\pi}\frac{R_\star}{R} + R\frac{d}{dR}\left(\frac{H_s}{R}\right) = \frac{4}{3\pi}\frac{R_\star}{R} + (\gamma(R) - 1)\frac{H_s}{R} \tag{3.45}$$

where $\gamma(R)$ is the flaring index defined as:

$$\gamma(R) = \frac{d\log H_s}{d\log R} \tag{3.46}$$

The flaring index is a number of order $\gamma \approx 2/9$. Its value is computed self-consistently during the iteration procedure. Usually the iteration is started with a guess for γ and updated after each few iteration steps. In order to avoid numerical instabilities, γ is always evaluated two radial gridpoints away from the point where it is used (see Appendix of [31] Chiang et al. 2001). It is important to note that a proper self-consistent computation of the flaring index γ is crucial if one wants to achieve energy conservation.

3.4.2 Location of the disk surface layer

The disk surface layer enclose the upper part of the disk and is locate above the surface height $z_s(R)$ which is define as the height z above the midplane where the visual optical depth along the direction of the incident stellar light is egual 1 (so where the direct stellar radiation is extinced by e^{-1}). The equation to solve to get $z_s(R)$ is then:

$$\tau_V(R, z_s) = \frac{\tau_V^{\perp}(R, z_s)}{\sin\, \alpha_{irr}(R)} = 1 \tag{3.47}$$

where $\tau_V^{\perp}$ is the vertical component of τ_V at the visible wavelenghts given by:

$$\tau_V^{\perp}(R, z) = \int_z^{\infty} \rho_d(R, z) k_V(R, z) dz$$

As visible wavelenght we use the peak of the blackbody star. So the surface layer is the disk region where the largest fraction of stellar radiation is absorbed.

3.5 Solving the RT problem with the VEF method

Once determinato the local amount of energy absorbed by the dust grains from the primary stellar radiation, we compute the dust temperature distribution. As discuss in Sec. 2.3.1.2, a straight-forward way to solve them is using the iterative procedure, know as '*Lambda Iteraction*', which first evaluate $I_{\mu,\nu}(z)$ (Eq. 3.11), then $J_\nu(z)$ (Eq. 3.49) and finally $T_d(z)$ (Eq. 3.12) and iterate this procedure until convergene is reached. Instead to use this approach, which converges very slowly in optically thick regions, we use the moment method '*Variable Eddington Factors*' (VEF). This approach is been proved by Dullemond et al. (2002) to be a faster method to find the solution $I_{\nu\mu}(z)$ of the radiative trasfer equation in circumstellar disk. Before to introduce the procedure, let's give a general overview of the moment method and the related closure problem.

The moments of the radiation field are defined as angular averange of the specific intensity. In 1D geometry the k-th moments of the radiation field is given by:

$$M_k(z) = \frac{1}{2} \int_{-1}^{1} I_{\mu,\nu}(z) \mu^k d\mu \quad (\mu = cos\theta) \tag{3.48}$$

From this definition we can write the first three moments as:

$$J_\nu(z) = \frac{1}{2}\int_{-1}^{1} I_{\mu,\nu}(z)d\mu \quad \textit{(mean Intensity)} \tag{3.49}$$

$$H_\nu(z) = \frac{1}{2}\int_{-1}^{1} I_{\mu,\nu}(z)\mu d\mu \quad \textit{(Eddington Flux)} \tag{3.50}$$

$$K_\nu(z) = \frac{1}{2}\int_{-1}^{1} I_{\mu,\nu}(z)\mu^2 d\mu \quad \textit{(K-integral)} \tag{3.51}$$

Fisically, the moment J_ν is simply the *mean intensity* of radiation, the moment H_ν is related to the *radiation flux* by $F_\nu = 4\pi H_\nu$ and K_ν is related to the *radiation pressure* by $p_\nu = (4\pi/c)K_\nu$. The second moment is usually written as a dimensionless factor times the mean intensity, $K_\nu = f_\nu J_\nu$, where f_ν is called *Eddington factor*.

The moments obey to the so-called *general moments equation*, obtained by multiplying the RT equation (3.6) by μ^k and integrating over all solid angles $d\mu$

$$\begin{aligned}\frac{1}{2}\int_{-1}^{1}\frac{dI_{\mu,\nu}(z)}{dz}\mu^{k+1}d\mu =& \rho(z)k_\nu(z)B_\nu(T_d(z))\frac{1}{2}\int_{-1}^{1}\mu^k d\mu \\ &- \rho(z)k_\nu(z)\frac{1}{2}\int_{-1}^{1} I_{\mu,\nu}(z)\mu^k d\mu\end{aligned} \tag{3.52}$$

This rappresent an infinite set of equations ($k = 0, ..., \infty$) and so one need to truncate the system. In general the moments equation are truncated at the second order:

$$\left.\begin{aligned}\frac{dH_\nu(z)}{dz} &= \rho(z)k_\nu(z)(B_\nu(T_d(z)) - J_\nu(z)) \\ \frac{d(f_\nu(z)J_\nu(z))}{dz} &= -\rho(z)k_\nu(z)H_\nu(z)\end{aligned}\right\} \tag{3.53}$$

The system of equation (3.53) is however not closed. We have infact 2 equations with 3 unknowns J_ν,H_ν,f_ν and nothing is gained by writing moments equation of order higher than second. This difficulty is known as the *closure problem* and one additional relation among the moments must somehow be obtained to close the system.

There is no easy way to formulate a closure relation. One of the possible strategies, adopted in a variety of astrophysical scenarios (Mihalas & Mihalas 1984) and which can circumvent the difficulty of solving the RT equation, is to consider that the radiation field is in *diffusion limit approximation*. This limit assumes that the photons meanfree path is much smaller than the scalelenght of the system (optically thick regime). In other words, in such a diffusion limit, the radiation field is supposed to be *isotropic* and the close relation is the so-called *Eddington approximation*:

$$p_\nu = \frac{1}{3}U_\nu \quad (\Rightarrow f_\nu = \frac{1}{3}) \tag{3.54}$$

where $U_\nu = (4\pi/c)J_\nu$ is the radiation energy density. However, this condition is violated in the optically thin regime, where the photon mean-free path is sufficiently

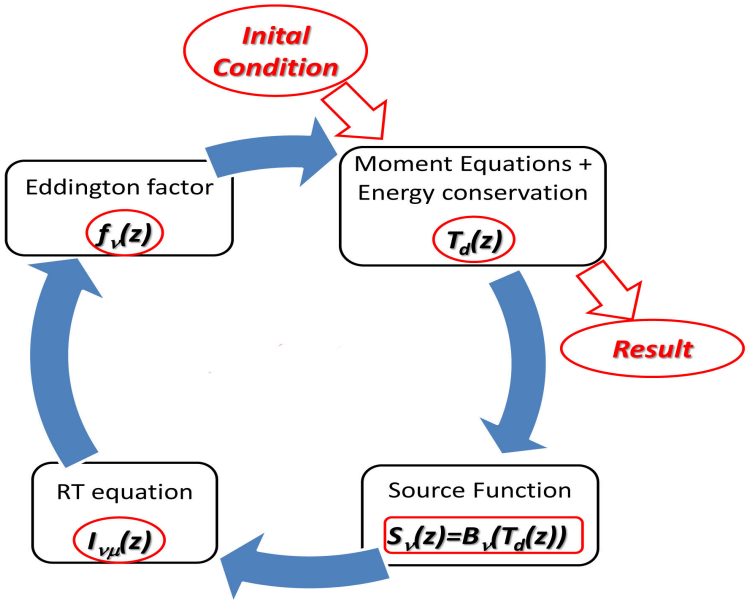

Figure 3.5: Scheme of the iterative VEF procedure to compute the dust temperature distribution.

larger then the scalelength of the system. In this case the radiation field generally become *anisotropic*. This can be fatal for problem involving circumstellar disk where both optically thin and thick regions are present and a RT model must be able to simultaneosly model both these parts of the disk. A more complex relation must be therefore applied in way to take into account the dependence of the Eddington factor from the optical depth τ.

The method we use is based on the *variable Eddington factor* (VEF) technique. The RT equation (3.65) and the moment equations (3.53) are solved with an iterative procedure which recompute iteratively the radiation field until the dust temperature profile converge. The variable Eddington factor $f(z)$ is updated at each iteration step and is used to close the moment equations. More in particular the procedure follow this sequence of steps:

- The Eddington factor $f_\nu(z)$ is used to close the truncated system of moment equations (Eq.3.53). Solving this system coupled with the local balance equation (Eq.3.12) we can determinate the dust temperature profile $T_d(z)$.
- The resulting temperature provide the source function ($S_\nu(z) = B_\nu(T_d(z))$) which we can use to integrate the formal solution (Eq. 3.11) allow to find the specific intensity $I_{\nu\mu}(z)$.
- From the resulting radiatiation field, we then update the Eddington factor $f_\nu(z)$ and use it in the first step.

These steps are iterated until a converged solution for $T_d(z)$ is reached, i.e. when

the relative difference in temperature between successive iterations drops below the convergence criterio

$$\max_{0\leq i\leq n_z-1}\left(\frac{|T_d^{old}(z_i)-T_d^{new}(z_i)|}{T_d^{old}(z_i)+T_d^{new}(z_i)}\right)<10^{-4} \tag{3.55}$$

3.5.1 Initial condition

We solve the VEF iterative procedure, departe from an *initial configuration*, corrisponding to an isotropic radiation field. In this way to solve the moment equation (3.56) we start with the J-mean Eddington factor $f_J = 1/3$. For the initial dust temperature T_d we take that corrisponding to the primary absorbtion of the stellar radiation. Finally, we initialize the J-mean opacity k_J to the planck dust opacity.

3.6 Numerical implementation for the RT problem

3.6.1 The Moment equations

The first step of our iterative procedure to solve the RT problem is to integrate the moment equations coupled with the local balance equation. This will provide the dust temperature $T_d(z)$ and therefore the source function $S_\nu(z)$ $(= B_\nu(T_d(z)))$. Instead of solving the full frequancy-dependent moment equations (3.53) we solve its frequency-integrated version:

$$\left.\begin{aligned}\frac{dH(z)}{dz}&=\rho(z)\left(k_P(T_d(z))\frac{\sigma_{SB}}{\pi}T_d(z)^4-k_J(z)J(z)\right)\\ \frac{d(f_J(z)J(z))}{dz}&=-\rho(z)\int_0^\infty k_\nu(z)H_\nu(z)d\nu\end{aligned}\right\} \tag{3.56}$$

where $\sigma_{SB}T_d^4/\pi = B(T_d) = \int_0^\infty B_\nu(T_d)d\nu$ is the frequency-integrated Planck function, $H = \int_0^\infty H_\nu d\nu$, $J = \int_0^\infty J_\nu d\nu$ are the frequency-integrated mean intensity and flux, respectively, and the quantities:

$$k_P(T_d)=\frac{\int_0^\infty B_\nu(T_d)k_\nu d\nu}{B(T_d)} \qquad k_J=\frac{\int_0^\infty k_\nu J_\nu d\nu}{J} \qquad f_J=\frac{\int_0^\infty f_\nu J_\nu d\nu}{J}$$

are respectively the Planck mean opacity, J-mean opacity and J-mean Eddington factor. These last two quantity are computed from the solution of the radiative transfer. As point out in [39] Dullemond et al. 2002 the second equation in 3.56 is integrated without use the the flux-mean opacity (or Rosseland opacity) $k_H = \int_0^\infty k_\nu H_\nu d\nu/H$ (see Appendix A in Dullemond et al. 2002).

The right-hand-side of the first equation can be moreover replace by the source term $Q(z)/4\pi$ by using the frequency-integrated version of the local energy conservation equation (3.12) which can be written

$$\rho(z)k_P(T_d(z))\frac{\sigma_{SB}}{\pi}T_d(z)^4=\rho(z)k_J(z)J(z)+\frac{Q(z)}{4\pi} \tag{3.57}$$

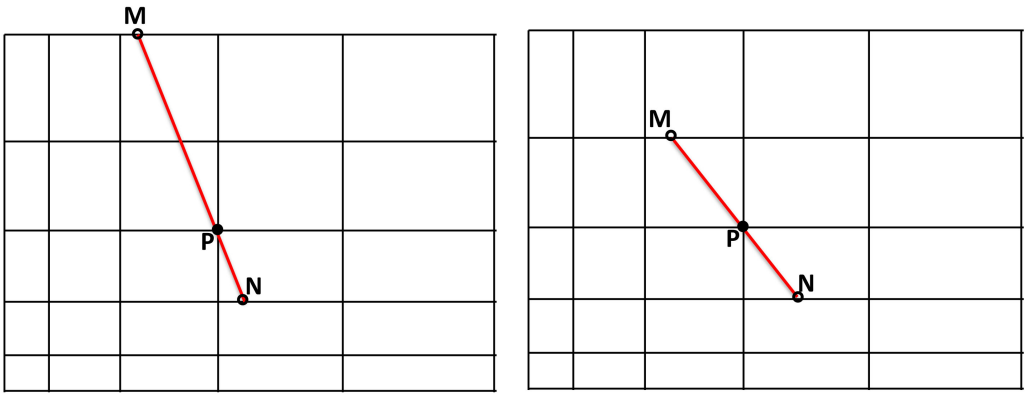

Figure 3.6: Scheme of integration paths in a 2D medium for the long characteristic method (*left*) and the short characteristic method (*right*). In both cases the rays are directed towards the bottom right. Note that the intensity values at the starting points must be determined by interpolation. When long characteristics are used many interpolations along the path are required in addition

The advantage of the moment equation (3.56) is that they can be integrated directly, using a two-point boundary value method. The first equation can be integrated from the midplane up to z_{max} using, at $z = 0$ the BC

$$H(0) = 0 \tag{3.58}$$

The second equation is integrated back from z_{max} towards the midplane using, at $z = z_{max}$, the BC

$$J(z_{max}) = H(z_{max})/\psi \tag{3.59}$$

where $H(z_{max})$ is that obtained from the first equation and the ratio ψ is computed from the solution of the radiative transfer. Both the differential equations are straight numerically solved using the forward Euler method.

Once the frequency-integrated mean intensity $J(z)$ is obtained, the dust temperature can be determined from the frequency-integrated energy conservation equation (Eq. 3.57). This allow us to obtained the source function which will be used to integrate the formal solution (Eq. 3.11).

3.6.2 Formal solution of the RT equation

Once the source function is know, we procede our iterative procedure solving at each hight z, direction μ and frequency ν, the formal solution (Eq. 3.11). This will provide the variable Eddington factor needed to close the truncated system of moment equations (3.56). Here we illustrate the method we are going to use in a more generale case of a $2D$ Cartesian grid (the application at $1D$ is then straighforward).

Essentially, the VEF method reduces the general RT problem into a set of formal solution. This means that the speed with which we solve a general RT problem is largely determined by the speed of the formal solution. Therefore, we have to seek as efficient numerical schemes for performing a formal solution as possible. The most straightforward way to do this is by the method of '*Long Characteristics*' (LC) where the integral equation is solved, at each spatial grid-point, along the entire ray coming from the external boundary (figure 3.6). The values of the quantities along the ray are obtained by interpolation. This method is accurate but computationally time-consuming as typically requires in the order of N integration steps. This means that if we have a spatial grid $N_{\vec{x}}^2$, angle grid N_Ω^2 and a set of N_ν frequencies, the total computational time (at each iteration) scales as

$$N_{CPU} \propto N_{\vec{x}}^3 \times N_\Omega^2 \times N_\nu \tag{3.60}$$

A more efficient algorithm to compute the formal solution is by the method of '*Short Characteristics*' (SC) ([86] Mihalas et al. 1978, [72] Kunasz & Auer 1988, [12] Auer & Paletou 1994) where instead of performing the integral, at each spatial grid-point, along the entire ray (the long characteristic), one perform the integral only along a portion of the ray (the short characteristic). If the point P is the grid point at which one wishes to calculate the specific intensity, for a given frequency ν and direction Ω, and the point M is the intersection point with the grid-plane that one finds when moving in the 'upwind' direction along $-\Omega$ (figure 3.6), the formal solution to solve at the point P is

$$I_P = I_M e^{-\Delta\tau_M} + \int_0^{\Delta\tau_M} S(\tau') e^{-(\Delta\tau_M - \tau')} d\tau' \tag{3.61}$$

where $\Delta\tau_M$ is the optical depth difference between points P and M and we have dropped the frequency and angle dependencies for clarity. In order to evaluate the intensity with this equation, we need to solve the integral of the source functions along the short characteristic $\overline{MP}$. Following Kunasz & Auer 1988 this integral can be solved, with second order accuracy, by interpoling the source function between the points M,P and N. In this way the formal solution become:

$$I_P = I_M e^{-\Delta\tau_M} + \alpha S_M + \beta S_P + \gamma S_N \tag{3.62}$$

where the coefficient α,β and γ are given by

$$\alpha = x + \frac{z - y(\Delta\tau_N + 2\Delta\tau_M)}{\Delta\tau_M(\Delta\tau_M + \Delta\tau_N)} \qquad x = 1 - e^{-\Delta\tau_M}$$
$$\beta = \frac{y(\Delta\tau_M + \Delta\tau_N) - z}{\Delta\tau_M \Delta\tau_N} \qquad y = \Delta\tau_M - x$$
$$\gamma = \frac{z - y\Delta\tau_M}{\Delta\tau_N(\Delta\tau_M + \Delta\tau_N)} \qquad z = (\Delta\tau_M)^2 - 2y$$

where $\Delta\tau_N$ are the optical depth difference between points P and N. In the previews relation the intensity I_M and the optical depth and source functions at the points

M and N are assumed to be known. In general, however, the M-point (like the point P) will not be a grid-point of the chosen 2D statial grid. These quantities have to be therefore calculated by interpoling from the available information at the surrounding grid-points.

The method of Short Characteristic is computationally less time consuming then the method of Long Characteristic, because now the transfer integral is performed over a much shorter path. For the same discretization introduced earlier in this section, the computational time scale as

$$N_{CPU} \propto N_{\bar{x}}^2 \times N_{\Omega}^2 \times N_{\nu} \tag{3.63}$$

which is typically an factor N shorter than in the case of Long Chracteristics.

1D Case. In our plane-parallele geometry we solve the formal solution with the SC method discussed above using the *two stream approach*. In this case we do not have the problem of additional interpolation (the points M and N in figure 3.6 are now grid-point of our spatial grid). The two stream approach consider the radiation field consisting in two streams, to up-streams I_ν^+ $(= I_\nu(+\mu))$ that cross the layers from the midplane to the top at angle $+\mu$ and down-streams I_ν^- $(= I_\nu(-\mu))$ that cross the layers in the opposite direction at angle $-\mu$ (the variable μ is restrict to a positive quantity $0 \leq \mu \leq 1$). With this approach we have to solve, for the two opposite directed pencils $\pm\mu$, the equations

$$\mu \frac{dI_\nu^+(z)}{dz} = \rho_d(z) k_\nu(z) \left(B_\nu(T_d(z)) - I_\nu^+(z) \right) \tag{3.64}$$

$$\mu \frac{dI_\nu^-(z)}{dz} = \rho_d(z) k_\nu(z) \left(B_\nu(T_d(z)) - I_\nu^-(z) \right) \tag{3.65}$$

We can perform the formal solution (3.62) by using the two-point boundary value method specifing two BC at the upper and lower grid-point. For the down-streams radiation I_ν^-, the formal solution is computed using, at $z = z_{max}$, the BC

$$I(-\mu, \nu, z_{max}) = 0 \tag{3.66}$$

So we are assuming no incaming radiation (the stellar radiation field is treated as separate problem as showed in Sec. 3.4). For the up-streams radiation I_ν^+, the formal solution is computed using, at $z = 0$, the BC

$$I(+\mu, \nu, 0) = I(-\mu, \nu, 0) \tag{3.67}$$

This is due to the symmetry condition of the radiation field respect to the midplane $z = 0$. Once the up-streams and down-streams intensity are obtained, two averange quantity are computed

$$u_{\mu,\nu}(z) = \frac{1}{2} \left(I_\nu^+(z) + I_\nu^-(z) \right) \quad \textit{(symmetric average)} \tag{3.68}$$

$$v_{\mu,\nu}(z) = \frac{1}{2} \left(I_\nu^+(z) - I_\nu^-(z) \right) \quad \textit{(antisymmetric average)} \tag{3.69}$$

which have, respectively, a mean-intensity-like and flux-like character. From these two quantities we can then compute:

$$J_\nu(z) = \int u_{\mu,\nu}(z)d\mu \quad H_\nu(z) = \int v_{\mu,\nu}(z)\mu d\mu \quad f_\nu(z) = \frac{\int u_{\mu,\nu}(z)\mu^2 d\mu}{J_\nu(z)}$$

and the respective frequency-integrated value J,H, J-mean Eddington factor f_J, J-mean opacity k_J and the ratio $\psi = J/H(z_{max})$ which are needed to solve the truncated system of frequency-integrated moment equations (Eq.3.56).

3.6.3 Convergence and Acceleration methods

Each successive iteration of our procedure, brings the solution closer to the true solution. A quicker convergence can be reach by applying a linear convergence amplifier. One common approach is to use the *Ng acceleration* method ([90] Ng 1974, [10, 11] Auer 1987, 1991). In this method one uses the results in previous iterates step to estimate the convergence behavior of the problem. After every fourth iteration steps an extrapolation can then be performed towards the expected convergence. The number of iteration is not a strict requirement but four is typically found to give a reliable and significant acceleration.
The effect of the acceleration is show, for example, in figure 3.12 where is shown the convergence history of the relative difference in temperature between successive iteration using the VEF method with Ng accelerator and without.

3.7 Dust-to-Gas ratio and Maximum grain size distribution

Numerical simulations of cougulation/sedimentation dust models in circumstellar disks predict that grains grow, migrate and frament in the disk and predict variation of dust properties as a function of position, disk age and physical properties. Detailed models of dust grain growth and settling and the resulting vertical disk structure can be found in [42] Dullemond & Dominik 2004. An analysis of the radial drift of the dust grains can be found in [26] Brauer et al. (2008) and [20] Birnstiel et al. (2010). In our model we do not include the detailed picture of the dust growth and sedimentation but we try to reproduce them incorporating in parametric way the possibility to have spatial variation of the maximum grain size and dust-to-gas ratio distribution.

We adopt for both these two distributions a profile characterised by a power law distribution in radial direction and a gaussian distribution in vertical direction:

$$\eta(R,z) = \eta_0 \left(\frac{R}{R_0^{(\eta)}}\right)^{d_R} exp\left(-d_z * \frac{z^2}{H_p^2}\right) \tag{3.70}$$

$$a_{max}(R,z) = a_0 \left(\frac{R}{R_0^{(a)}}\right)^{b_R} exp\left(-b_z * \frac{z^2}{H_p^2}\right) \tag{3.71}$$

where η_0 (a_0) is the dust-to-gas ratio (maximum grain size) value at the reference position (R_0, z_0) ($(R_{in}, 0)$ for η and $(40, 0)$AU for a_{max}), d_R (b_R) is the index of the radial power law profile and d_z (b_z) is the index of vertical gaussian profile. We relate this two quantities to the disk structure expressing the vertical gaussian profile of both distributions in function of the characteristic pressure height $H_p(R)$. In this way, at the height H_p, the dust-to-gas ratio decrease of a factor e^{d_z} (e^{b_z} for the maximum grain size) respect at the midplane. As the disk is not isothermal in vertical direction we can not use the classical expression (Eq. 3.3) valid for an vertically isothermal disk. As show the Eq. 3.2, H_p represents the height at which the pressure decrease of a factor $e^{1/2}$. We define therefore H_p in this way computing the vertical gas pressure profile (Eq. 3.31) using the temperature and density distributions compute, respectively, in step 2 and 3 of our iteration procedure.

The *maximum grain size* $a_{max}(R, z)$ and the *dust-to-gas ratio* $\eta(R, z)$ distributions contribuite to specify the dust opacity distribution ($\kappa_\nu = \rho_d k_\nu$) and they therefore regulate the radiative transport in the disk and so influence its thermal structure. Using different Rz-distribution for a_{max} and η we will see (Sec. 3.12) that the model predict change in the disk structure and dust continuum emission.

3.8 Observable: SED and Emission Map

After our iterative procedure compute the thermal and geometrical disk structure of the disk in vertical hydrostatic equilibrium, intensity profile and Spectral Energy Distribution (SED) can be produced. This is done by using the ray-tracing procedure which compute the emerging intensity by integrating the formal solution of the RT equation (Eq. 3.11) along rays originating from the observer. As we have done in Sec.3.6.2 to solve the thermal structure, we use here the same numerical algorithm (see. Sec. 3.6.2). Once obtained the intensity profile $I_\nu(R)$ at each wavelenght, we can then compute the resulting flux.

Fiducial Annulus Model			
STAR	$L_\star = 0.3 L_\odot$	ANNULUS	$R = [10 - 10.1] AU$
	$M_\star = 0.5 M_\odot$	DOMAIN	$z = [0 - 8 H_p]$
	$T_\star = 3000° K$	GAS SURFACE	$\Sigma_g = 100 g/cm^2$
GAS	$\mu = 2.3$	DENSITY	
COMPOSITION	(H_2,He mixture)	DUST-TO-GAS	$\eta_0 = 0.01$
DUST	7% silicates	RATIO	$d_R = 0.0$, $d_z = 0.0$
COMPOSITION	21% carbonaceous	MAXIMUM	$a_0 = 10 \mu m$
	42% water ice	GRAIN SIZE	$b_R = 0.0$, $b_z = 0.0$
	30% vacuum		

Table 3.1: Parameters of the fiducial annulus model.

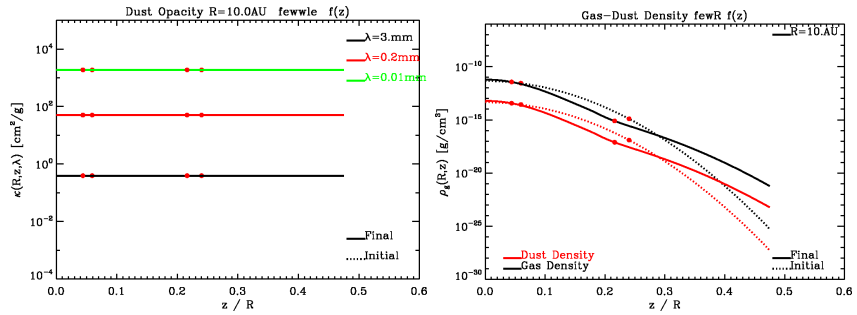

Figure 3.7: The dust opacity $k_\nu(z)$ distributions at few wavelenghts (*left panel*) and the gas-dust density distributions $\rho_g(z)$, $\rho_d(z)$ (*right panel*) of the fiducial annulus model.

3.9 Annulus structure and emission

To illustrate the basic results of the annulus structure calculation, we construct a **fiducial annulus model** (table 3.1) for a typical T Tauri star. We consider an annulus at $10AU$ from the central star with width $0.1AU$ (i.e an annulus between 10 and 10.1 AU) and extended in vertical direction from the midplane $z = 0$ to $z_{max} = 8H_p$ (where H_p is the pressure height of the initial gaussian density distribution). This model corrisponds to a annulus with gas mass $M^{gas}_{annulus} = 7.1 \times 10^{-5} M_\odot$ and so dust mass $M^{dust}_{annulus} = 7.1 \times 10^{-7} M_\odot$. For this annulus test we assume, for simplicity, that the incident angle is fixed to $\alpha = 0.05$. Our computations adopt a uniform grid of 100 points in vertical direction, a logarithmic grid in wavelenght of 100 points covering a domain $0.1\mu m \leq \lambda \leq 1cm$ and a logarithmic grid in μ of 100 points covering a domain $0.01 \leq \mu \leq 1$. To show how the final result (i.e. when the convergence criterio is reached) change respect to the results corrisponding to the initial guess (IG) configuration, we plot both the initial (dot line) and final (solid line) profile. The red points overplotted correspond to the characteristic heights of the disk: the gas pressure height H_p and the surface height z_s. The dust deplection

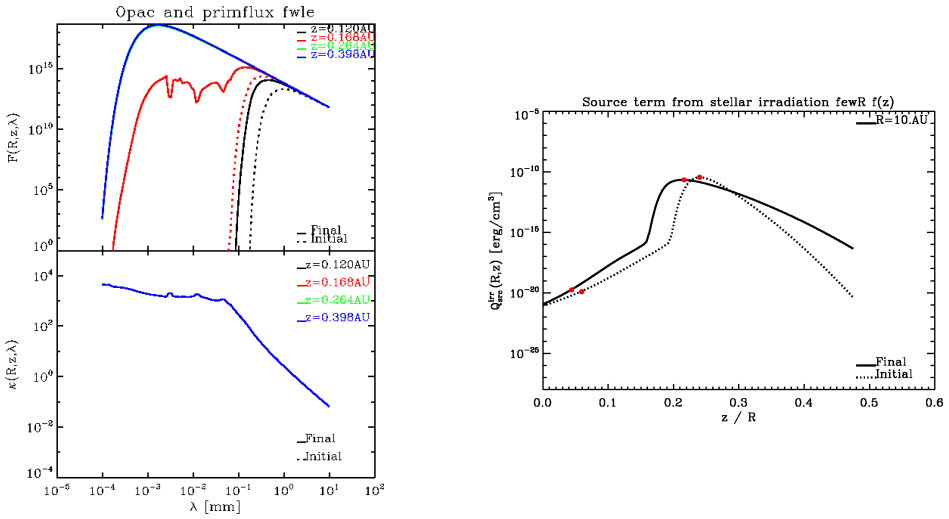

Figure 3.8: The source term from stellar irradiation of the fiducial annulus model.

height z_{depl} is setted by the $a_{max}(z)$ distribution which in this case correspond to z_{max} because of the constant ($10\mu m$) $a_{max}(z)$ distribution.

In Fig. 3.7 (*left pannel*) we show the resulting dust opacity $k_\nu(z)$ at few wavelenghts. Because of the constant dust properties along the annulus, the opacity has therefore a vertically constant profile with lower values at long wavelengths (black line) than at shorter wavelenghts (green line). This can be also see in Fig. 3.8 (*left-bottom pannel*) where is shown the opacity in function of the wavelenght.

In Fig. 3.7 (*right pannel*) we show the resulting gas density profile $\rho_g(z)$ (black line). The initial gaussian profile (dot line) turn, when the vertical HS equilibrium is reached, in a profile which is stepper then the gaussian in the inner layer and shallower in the surface layer. This is given to the presence, now, of a temperature gradient in vertical direction and can be easily understood looking the Eq. 3.32 and the resulting temperature (Fig. 3.10). Just above the gas pressure height, where the temperature increase very fast, the gas density gradient increase; while in the upper layer, where the temperature stabilize at a certain value, the density gradient become smaller. For this reason, moreover, the resulting gas pressure height is slightly different of that of an initial vertically isothermal disk. At each height z, the dust density (red line) has a value 100 time less then the gas density one because of the constant (0.01) dust-to-gas ratio distribution.

In Fig. 3.8 (*right pannel*) we show the resulting energy absorbed by the dust grains from the primary stellar radiation $Q(z)$. Starting from upper point z_{max} the profile is characterized by an initial increase and then by an quick decrease. This can be easly understood looking at the resulting stellar radiation flux (Fig. 3.8 *left-top pannel*) and dust density (Fig. 3.7 right pannel) profiles (see the Eq. 3.40). In the upper layer, where the flux does not change due the optically thin regime environment, the energy absorbed by the dust increase because of the increase in dust density. When the stellar radiation cross over the surface height z_s, the

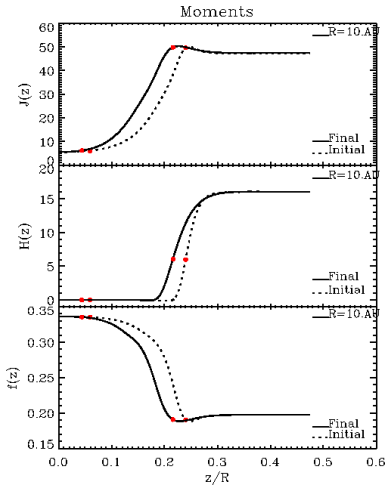

Figure 3.9: Characteristic quantities of the radiation field. *Top panel*: the frequency-integrated mean intensity $J(z)$. *Central panel*: the frequency-integrated Eddington flux $H(z)$. *Bottom panel*: the frequency-averaged Eddington factor $f(z)$.

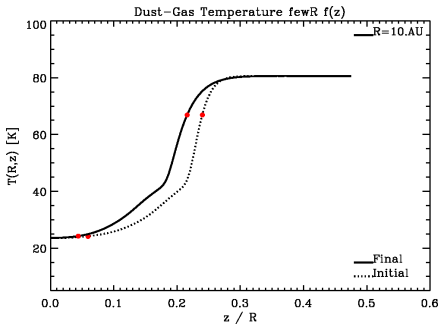

Figure 3.10: The gas-dust temperature distribution $T(z)$ of the fiducial annulus model.

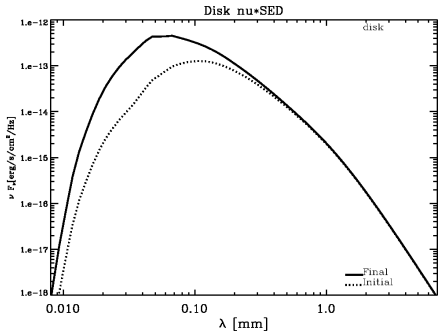

Figure 3.11: The SED of the fiducial annulus model.

exponentially decrease of the flux cause a fall off of the energy absorbed by the dust and only a very small ammount of energy (from the longest wavelengths) is absorbed by the midplane dust.

In Fig. 3.9 we show same characteristic quantities of the radiation field in the disk. Firstly, one can see (*bottom pannel*) how the Eddington factor $f(z)$ drop below 1/3 in the upper layers of the disk. This because here we are in optically thin regime and we are not in the diffusion limit approximation anymore and the radiation field become anisotropic.

In Fig. 3.10 we show the resulting temperature distribution $T(z)$. As we can see the temperature profile shift downward. This can be understood looking at the resulting $Q(z)$ (Fig. 3.8 right pannel) and mean intensity $J(z)$ profiles (see Eq. 3.57). At lower heights, the stellar energy absorbed by the dust and the mean intensity of the reprocessed radiation is bigger at the final configuration, we have an higher temperature at the final configuration.

In Fig. 3.11 we show the resulting SED. As we can see, the infrared flux from the annulus in vertical HS equilibrium increase respect to that corrisponding to the initial configuration. The reason for this is that the IR emission forms in the upper layers of the disk where the final dust density value result bigger then the initial gaussian profile (see Fig. 3.7 *right pannel*).

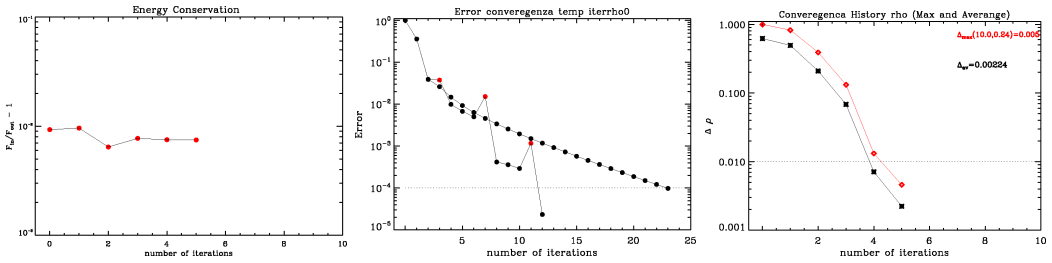

Figure 3.12: *Left panel*: Energy conservation test. *Central panel*: Convergence history for the relative difference in temperature between successive iteration using the VEF method with Ng acceleration and without acceleration. *Right panel*: Convergence history for the relative difference in gas density between successive iteration to reach the vertical HS equilibrium.

3.9.1 Testing and convergence

In order to verify the reliability of our annulus structure calculation, a few tests are performed. First of all we check if we have achive the energy conservation i.e the annulus emitt more or less radiation that they receive (entering flux $F_{in} \backsimeq$ exit flux F_{out}). As show the Fig. 3.12 (*left panel*) the difference relative between F_{in} and F_{out}, at each iteration, remain less then 1%.

Fig. 3.12 (*central panel*) shows the convergence history for the relative difference in temperature between successive iteration using the VEF method with Ng accelerator and without accelerator. How we can see using extrapolate temperature every 4 step reduce considerably the number of iteration. As proved by [39] Dullemond et al. (2002) the VEF method is much faster then method like Lambda Iteration (LI) and Accelerator Lambda Iteration (ALI) (see Appendix A2 in Dullemond et al.).

Finally, Fig. 3.12 (*right panel*) shows the convergence history for the relative difference in gas density between successive iteration to reach the vertical HS equilibrium. How we can see our convergence criterio is reached (*red points*) after six iteration. We also plot the average difference (*black points*) which obviously decrease rapidly.

3.10 Effects of different $\eta(z)$ and $a_{max}(z)$ distributions on the annulus structure

Here we show how different $\eta(z)$ and $a_{max}(z)$ distributions, affect the structure and emission properties of the annulus. In order to do this we consider two grids of models, each one construct varing, respect to the fiducial model (table 3.1), the values of few parameters corrisponding to the effect that we want to investigate. In particular we will analyze the effect of the dust-to-gas ratio distribution (*grid model A*), maximum grain size distribution (*grid model B*). For each model we compute the self-consistent annulus structure in vertical hydristatic equilibrium (as described in Sec. 3.2) and the Spectral Energy Distribution (as described in Sec. 3.8).

Grid model A			
η_0	**0.01**	0.0125	0.015
d_z	**0.0**	0.186	0.394

Table 3.2: Parameters of the model grids for the dust-to-gas ratio distribution (Eq.3.70): d_z is the index of vertical Gaussian profile and η_0 is the dust to gas ratio value at the reference position $z_0 = 0$. The **fiducial model** values are highlighted in bold face.

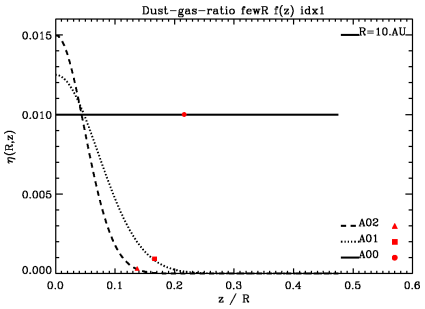

Figure 3.13: The dust-to-gas ratio $\eta(z)$ of the grid model A.

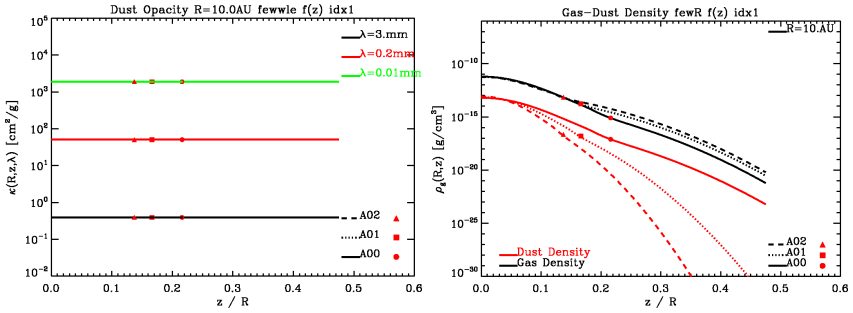

Figure 3.14: The dust opacity $k_\nu(z)$ distributions at few wavelenghts (*left panel*) and the gas-dust density distributions $\rho_g(z)$, $\rho_d(z)$ (*right panel*) of the grid model A.

3.10.1 Effects of spazial variation of the $\eta(z)$ distribution

In order to see the effect of the *dust-to-gas ratio* distribution $\eta(z)$, we construct a grid of 3 models (table 3.2) varing the parameters η_0 and d_z (d_R is fixed to zero) of our gaussian parametrization (Eq. 3.70). The model A_0 corrispond to the fiducial annulus model (Sec. 3.9) with constant $\eta(z)$ distribution and the model A_1,A_2 corrispond to annuli with increse z-variation (Fig. 3.13). As consequence of this increase of the index d_z, the annuli have different dust density profiles (Fig. 3.14 *right pannel* red lines). However the parameters η_0 and d_z have been chosen in a way to have 3 annuli with the same dust surface density ($\Sigma_d = 1.0 g/cm^2$) and so the same dust mass ($M_d = 7.1 \times 10^{-7} M_\odot$). In this grid models the variation of the vertical optically depth distributions and so of the flux $F_\nu(z)$ of the stellar radiation that penetrate through the annulus, are essentially due to the variation of the dust density distribution.

In Fig. 3.15 (*top pannel*) we show the resulting dust absorbed energy $Q(z)$ from the primary stellar radiation. How we can see the grains in the upper layers absorb, at a given z, more energy in model 0 then in model 2. This because in these layers the dust density has heigher values in model 0 then in model 2 (see Fig. 3.14 *right pannel*). For this reason, moreover, the surface height z_s ($\tau = 1$) move downward

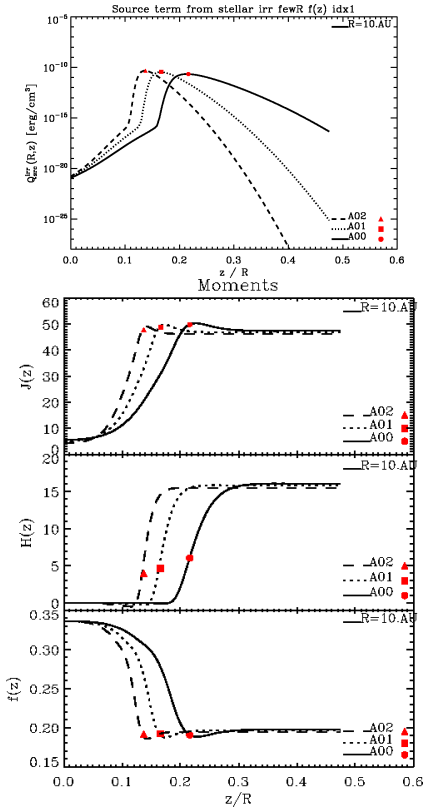

Figure 3.15: The source term from stellar irradiation $Q(z)$ (*top panel*) and the characteristic quantities of the radiation field (as in Fig. 3.9) (*bottom panels*) of the grid model A.

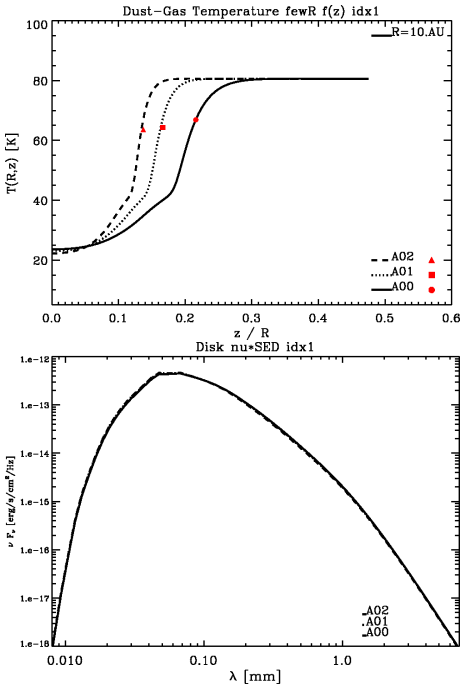

Figure 3.16: The gas-dust temperature distribution $T(z)$ (*top panel*) and SED (*bottom panel*) of the grid model A.

from model 0 to model 2: the stellar photons can deppler penetrate the annulus in model 2 and so the largest fraction of stellar radiation is absorbed closer to the midplane.

In Fig. 3.15 (*bottom pannel*) we show same characteristic quantities of the radiation field in the disk.

In Fig. 3.16 (*top pannel*) we show the resulting temperature distribution $T(z)$. As we can see the temperature profile shift downward from model 0 to model 2. This because the surface height z_s move downward. At lower heights, as the stellar energy absorbed by the dust and the mean intensity of the reprocessed radiation increase from model 0 to model 2, we have an higher temperature in model 2 then in model 0. Near the midplane, however, the temperature is ...

In Fig. 3.16 (*bottom pannel*) we show the resulting SED.

Grid model B			
a_0[mm]	**0.01**	0.2	3.0
b_z	**0.0**	0.18	0.5

Table 3.3: Parameters of the models grid for the maximum grain size distribution (Eq.3.71): b_z is the index of vertical Gaussian profile and a_0 is the maximum grain size value at the reference position $z_0 = 0$. The **fiducial model** values are highlighted in bold face.

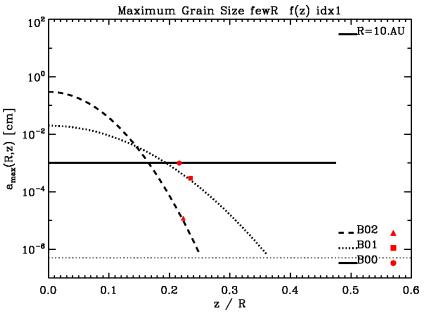

Figure 3.17: The maximum grain size distribution $a_{max}(z)$ of the grid model B.

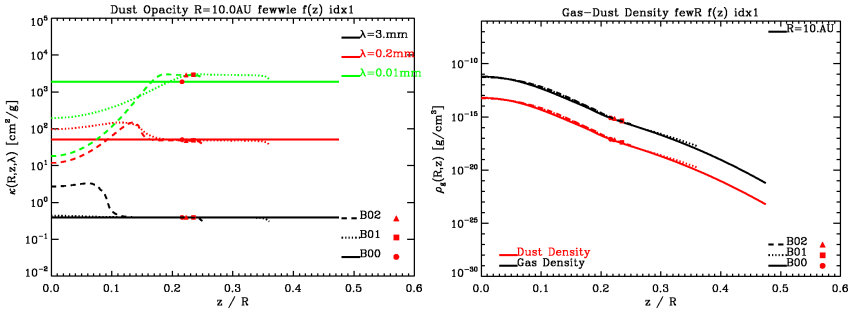

Figure 3.18: The dust opacity $k_\nu(z)$ distributions at few wavelenghts (*left panel*) and the gas-dust density distributions $\rho_g(z)$, $\rho_d(z)$ (*right panel*) of the grid model B.

3.10.2 Effects of spazial variation of the $a_{max}(z)$ distribution

In order to see the effect of the *maximum grain size* distribution $a_{max}(z)$, we construct a grid of 3 models (table 3.3) varing the parameters a_0 and b_z (b_R is fixed to zero) of our gaussian parametrization (Eq. 3.71). The model B_0 corrispond to the fiducial annulus model (Sec. 3.9) with constant $a_{max}(z)$ distribution and the model B_1,B_2 corrispond to annuli with increase z-variation (Fig. 3.17). As consequence of this increase of the index b_z, the deplection height z_{depl} become lower as the maximum grain size reach the minimum size at lower height. In this way, moreover, the dust surface density Σ_d decrease from model B_0 to model B_2 (as the dust-to-gas ratio profile is fixed). However this decrease of dust mass is very low as we are just cutting the tail of the $\sim$ gaussian dust density distribution in the upper layer. So, as in the grid model A, we are compare 3 annuli with the same dust surface density ($\Sigma_d = 1.0 g/cm^2$) and so the same dust mass ($M_d = 7.1 \times 10^{-7} M_\odot$).

In Fig. 3.18 (*left pannel*) we show the resulting dust opacity $k_\nu(z)$ at few wavelenghts. How we can see, the variation of the a_{max} profile lead to different dust opacity profile. The dust opacity has, at each wavelenght, a peak in its distribution. The width of the peak and his position in the annulus depend from the z-variation of the maximum grain size and can be clearly understood looking at the plot $k_\nu(z)$

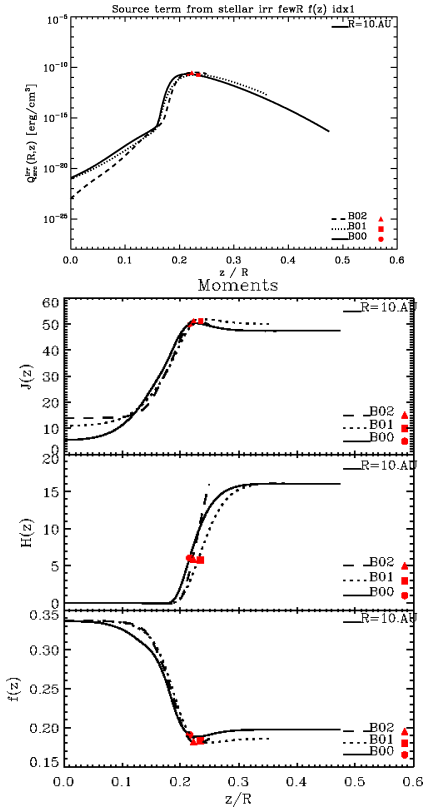

Figure 3.19: The source term from stellar irradiation $Q(z)$ (*top panel*) and the characteristic quantities of the radiation field (as in Fig. 3.9) (*bottom panels*) of the grid model B.

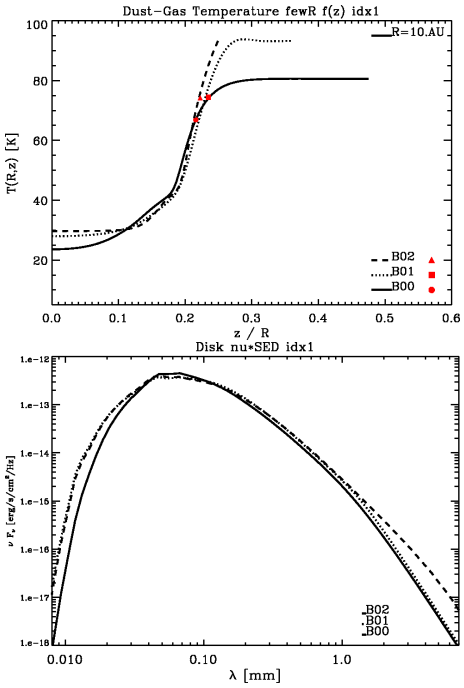

Figure 3.20: The gas-dust temperature distribution $T(z)$ (*top panel*) and SED (*bottom panels*) of the grid model B.

as function of a_{max} (Fig. 2.2). For wavelenght of $3mm$, for example, the regions of the annulus that have a value of a_{max} between 0.01 cm and 0.1 cm, will present the peak in the $k_\nu(z)$ distribution. In particular, the position of the opacity peak move to lower heights as the index b_z increase from model B_0 to model B_2. This beacuse the a_{max} range, responsible for the opacity peak, move at lower z. In this grid models the variation of the vertical optically depth profile and so of the flux $F_\nu(z)$ of the stellar radiation that penetrate through the annulus, are essentially due to the variation of the dust opacity distribution.

In Fig. 3.19 we show the resulting dust absorbed energy $Q(z)$ from the primary stellar radiation.
In Fig. 3.19 we show same characteristic quantities of the radiation field in the disk.
In Fig. 3.20 we show the resulting temperature distribution $T(z)$.
In Fig. 3.20 we show the resulting SED.

Fiducial Disk Model			
STAR	$L_\star = 0.3 L_\odot$	DISK DOMAIN	$R = [0.1 - 150] AU$
	$M_\star = 0.5 M_\odot$		$z = [0 - 8H_p]$
	$T_\star = 3000° K$	GAS SURFACE	$\Sigma_0 = 25 g/cm^2$
GAS	$\mu = 2.3$	DENSITY	$p = 1.0$
COMPOSITION	(H_2,He mixture)	DUST-TO-GAS	$\eta_0 = 0.01$
DUST	7% silicates	RATIO	$d_R = 0.0$, $d_z = 0.0$
COMPOSITION	21% carbonaceous	MAXIMUM	$a_0 = 10 \mu m$
	42% water ice	GRAIN SIZE	$b_R = 0.0$, $b_z = 0.0$
	30% vacuum		

Table 3.4: Parameters of the fiducial disk model.

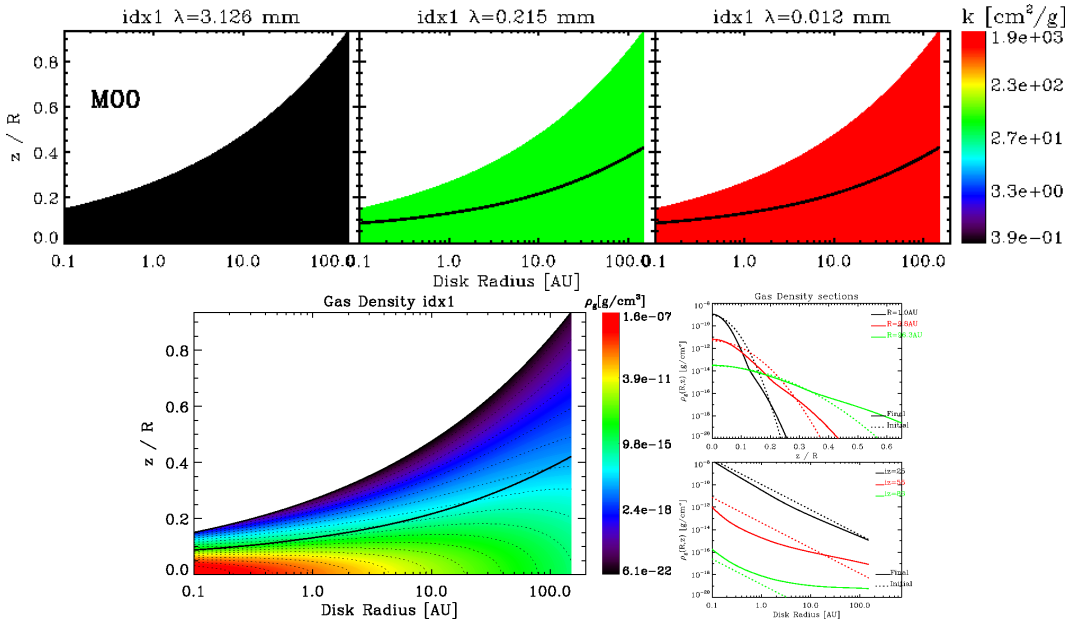

Figure 3.21: The dust opacity $k_\nu(R, z)$ distributions at few wavelenghts (*top panel*) and the gas density distribution $\rho_g(R, z)$ (*bottom panels*) of the fiducial disk model.

3.11 Disk structure and emission

To illustrate the basic results of the disk structure calculation, we construct a **fiducial disk model** (table 3.4) for a typical T Tauri star. We consider a disk with an inner hole extended in radial direction from $0.1 AU$ to $150 AU$ from the central star and in vertical direction from the midplane $z = 0$ to $z_{max} = 8H_p(R)$ (where H_p is the pressure height of the initial gaussian density distribution). We assume here a surface density following a power low distribution $\Sigma_g(R) = \Sigma_g \, (R/R_0)^p$. This model corrisponds to a disk with gas mass $M_{disk}^{gas} \backsimeq 0.1 M_\odot$ and so dust mass

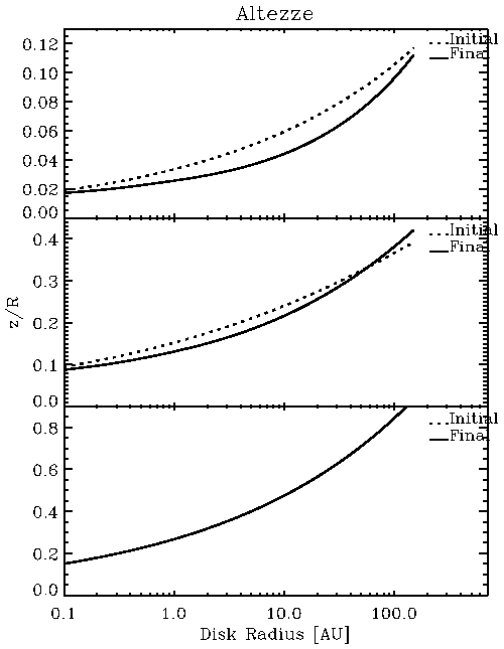

Figure 3.22: The characteristic disk heights profiles of the fiducial disk model. *Top panel*: the pressure height scale $H_p(R)$. *Middle panel*: the disk surface height $z_s(R)$. *Bottom panel*: the deplection height $z_{depl}(R)$.

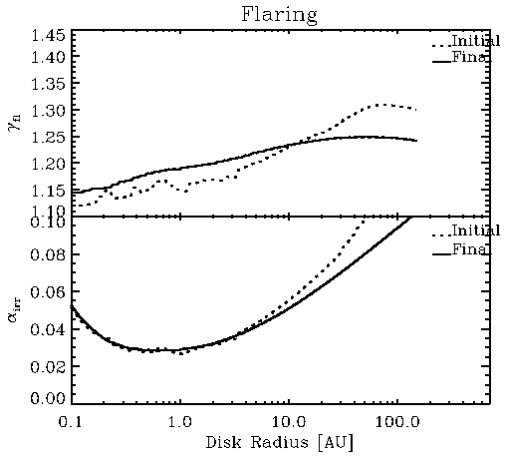

Figure 3.23: The flaring index $\gamma(R)$ (*top panel*) and incidente angle $\alpha_{irr}(R)$ profiles (*bottom panel*) of the fiducial disk model.

$M_{disk}^{dust} \backsimeq 10^{-3} M_{\odot}$. Our computations adopt the same grids used in the annulus test (Sec. 3.9) with a logarithmic grid of 100 points in radial direction. To show how the final result (i.e. when the convergence criterio is reached) change respect to the results corrisponding to the initial configuration, we plot both the initial guess (IG) (solid line) and final (F) (dot line) profile. The red points overplotted correspond to the characteristic heights of the disk: the gas pressue height H_p and the surface height z_s. The dust deplection height z_{depl} is setted by the $a_{max}(R,z)$ distribution which in this case correspond to z_{max} because of the constant $(10\mu m)$ $a_{max}(R,z)$ distribution.

In Fig. 3.21 (*top pannels*) we show the resulting dust opacity $k_\nu(R,z)$ at few wavelenghts. Because of the constant dust properties throghtout the disk, the opacity has therefore a spatially constant profile with lower value at long wavelenghts (*left pannel*) then at shorter wavelenght (*right pannel*) (see also Fig. 3.8 *left-bottom pannel* where is shown the opacity in function of the wavelenght).

In Fig. 3.21 (*bottom pannels*) we show the resulting gas density distribution $\rho_g(R,z)$. Clearly the gas density distribution decrease in radial direction as we have choosen a gas surface density with $p > 0$. As we have already discuss in the annulus test (Sec. 3.9), the resulting vertical gas density gradient change with respect to that of the initial isotermal configuration as a consequence of the presence, now,

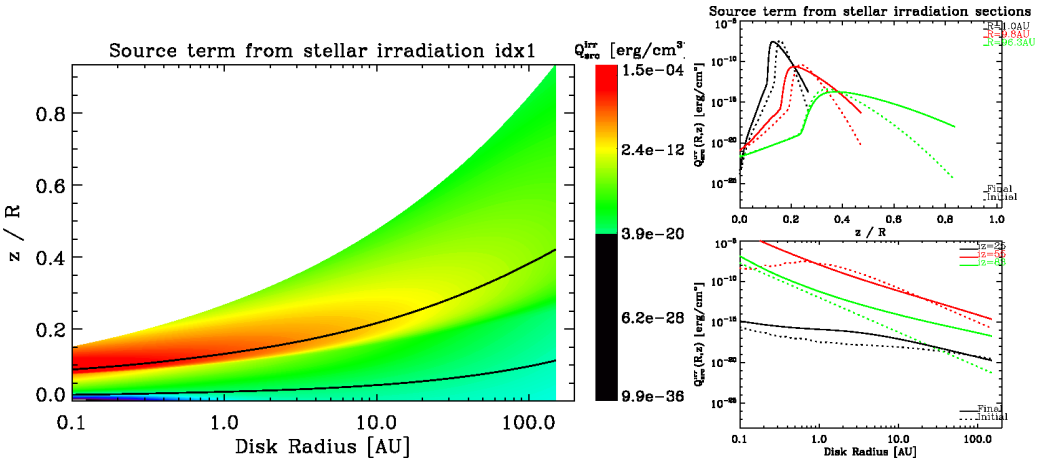

Figure 3.24: The source term from stellar irradiation $Q(R, z)$ of the fiducial model. *Left panel*: the final distribution in the (R,z) plane. *Right panels*: some R and i_z sections.

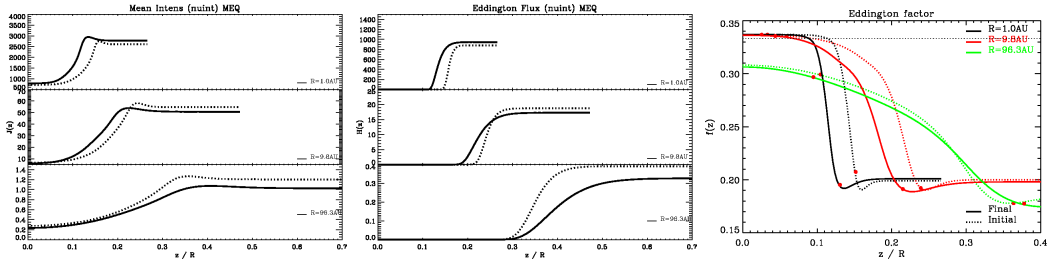

Figure 3.25: Some characteristic quantities of the radiation field as derive solving the RT problem with VEF method of the fiducial disk model. *Left panel*: the frequency-integrated mean intensity $J(z)$. *Central panel*: the frequency-integrated Eddington flux $H(z)$. *Right panel*: the frequency-averaged Eddington factor $f(z)$.

of a vertical temperature gradient (Fig. 3.26). At each position (R, z) the dust density has a value 100 time less then the gas density one because of the constant (0.01) dust-to-gas ratio distribution.

In Fig. 3.22 we show the resulting characteristic heights profiles $H(R)$.
In Fig. 3.23 we show the resulting flaring index profile $\gamma(R)$.

In Fig. 3.24 we show the resulting energy absorbed by the dust grains from primary stellar radiation $Q(R, z)$. As we have already discuss in the annuls test (Sec. 3.9) the vertical profile of Q is characterized by a peak in correspondence to the surface height z_s.

In Fig. 3.25 we show same characteristic quantities of the radiation field in the disk. As we have already discuss in the annuls test (Sec. 3.9), the Eddington factor $f(z)$ drop below 1/3 in the upper layers of the disk.

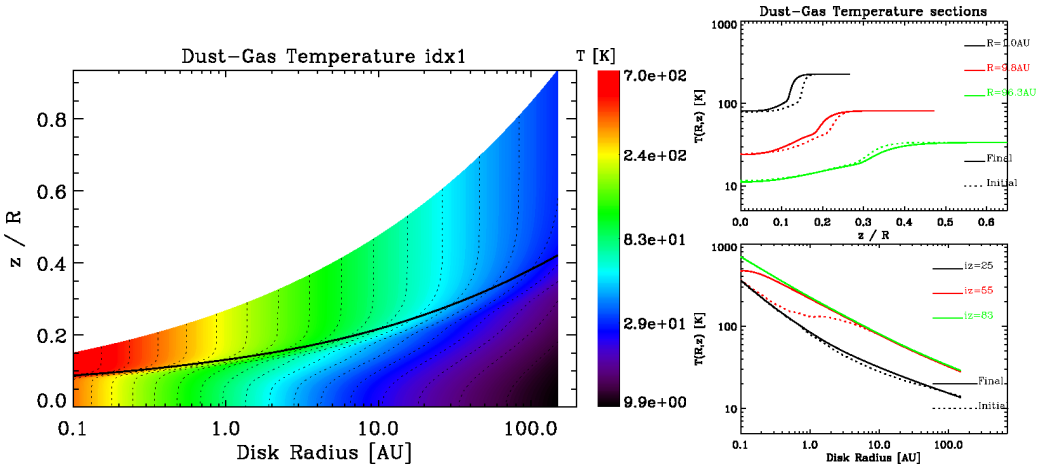

Figure 3.26: The gas-dust temperature distribution $T(R,z)$ of the fiducial model. *Left panel*: the final distribution in the (R,z) plane. *Right panels*: some R and i_z sections.

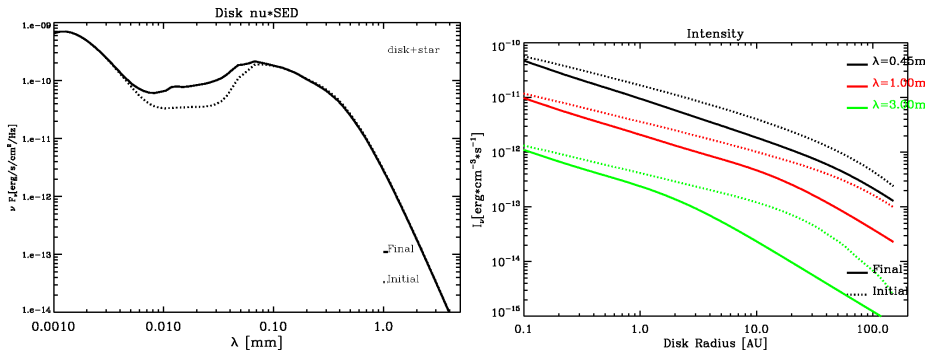

Figure 3.27: The SED (*left panel*) and intensity profile ar few wavelenghts (*right panel*) of the fiducial disk model.

In figure 3.26 we show the resulting temperature distribution $T(R,z)$.

In figure 3.27 we show the resulting intensity profile and SED.

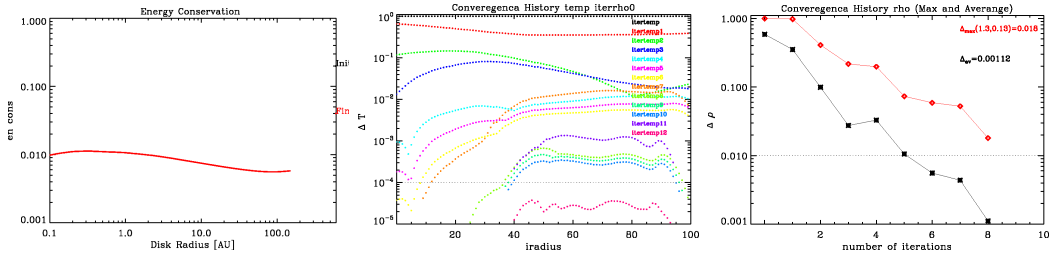

Figure 3.28: *Left panel*: Energy conservation test. *Central panel*: Convergence history for the relative difference in temperature between successive iteration, for each annulus, using the VEF method with Ng acceleration. *Right panel*: Convergence history for the relative difference in gas density between successive iteration to reach the vertical HS equilibrium.

3.11.1 Testing and convergence

As the annulus test, in order to verify the reliability of our disk structure calculation, we performe few tests. First of all we check if we have achive the energy conservation i.e the annulus emitt more or less radiation that they receive (entering flux $F_{in} \backsimeq$ exit flux F_{out}). As show the Fig. 3.28 (*left panel*) the difference relative between F_{in} and F_{out}, at each iteration, remain around 1%.

Fig. 3.28 (*central panel*) show the convergence history for the relative difference in temperature between successive iteration, for each annulus, using the VEF method (with Ng accelerator). How we can see on average the number of iteration is around 10.

Finally, the Fig. 3.28 (*right panel*) show the convergence history for the relative difference in gas density between successive iteration to reach the vertical HS equilibrium. How we can see our convergence criterio is reached (*red point*) after 10 iteration.

3.12 Effects of different $\eta(R,z)$ and $a_{max}(R,z)$ distributions on the disk structure

Here we show how the different $\eta(R,z)$ and $a_{max}(R,z)$ distributions, affect the structure and emission properties of the disk. In order to do this we consider, as in the annulus test, two grids of models, each one construct varing, respect to the fiducial model (table 3.4), the values of few parameters corrisponding to the effect that we want to investigate. In particular we will analyze the effect of the dust-to-gas ratio distribution (*grid model A*), maximum grain size distribution (*grid model B*). For each model we compute a self-consistent disk structure in vertical hydristatic equilibrium (as described in Sec. 3.2) and the Spectral Energy Distribution (as described in Sec. 3.8).

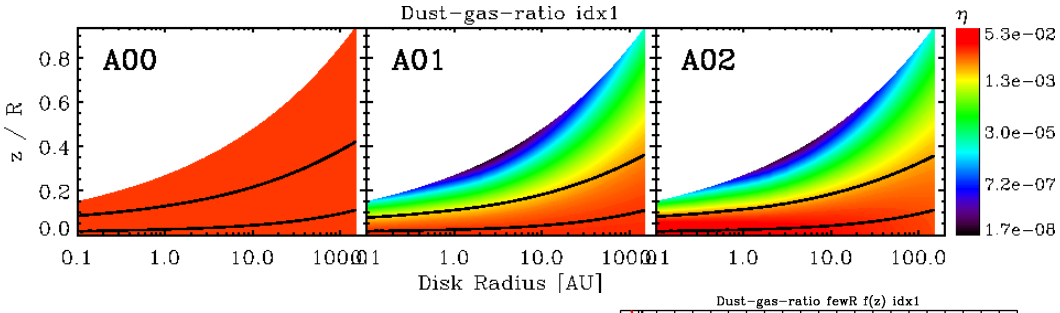

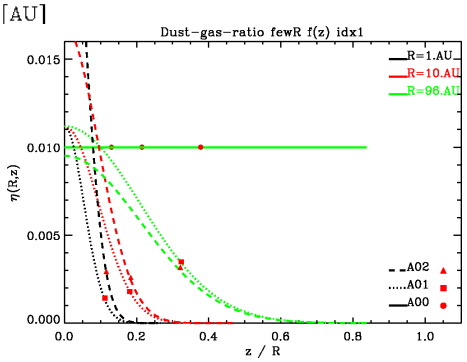

Figure 3.29: The final dust-to-gas ratio distribution in the (R, z) plane (*top panels*) and some R sections (*bottom panel*) of the grid model A.

Grid model A			
η_0	**0.01**	0.0112	0.053
d_R	**0.0**	0.0	0.25
d_z	**0.0**	0.1	0.1

Table 3.5: Parameters of the models grid for the dust-to-gas ratio distribution (Eq.3.70): d_R is the index of radial PL profile, d_z is the index of vertical Gaussian profile and η_0 is the dust-to-gas ratio value at the reference position $(0.1, 0)AU$. The **fiducial model** values are highlighted in bold face.

3.12.1 Effects of spazial variation of the $\eta(R, z)$ distribution

In order to see the effect of the *dust-to-gas ratio* distribution $\eta(R, z)$, we construct a grid of 3 models (table 3.5) varing the parameters η_0,d_R and d_z of our parametrization (Eq. 3.70). The model A_0 corrispond to the fiducial disk model (Sec. 3.11) with constant $\eta(R, z)$ distribution, the model A_1 corrispond to a disks with z-variation and R-constant distribution and the model A_2 corrispond to a disks with same z-distribution of A_1 but with also R-variation (Fig. 3.29). As consequence of this different parameters value, the disks have different dust density profiles (Fig. 3.30 *bottom pannel*). However the parameters η_0,d_R and d_z have been chosen in a way to have 3 disks with the same dust mass $M_d = 0.00106 M_\odot$. In this grid models the variation of the optically depth distribution and so of the flux $F_\nu(R, z)$ of the stellar radiation that penetrate through the disk, are essentially due to the variation of the dust density distribution.

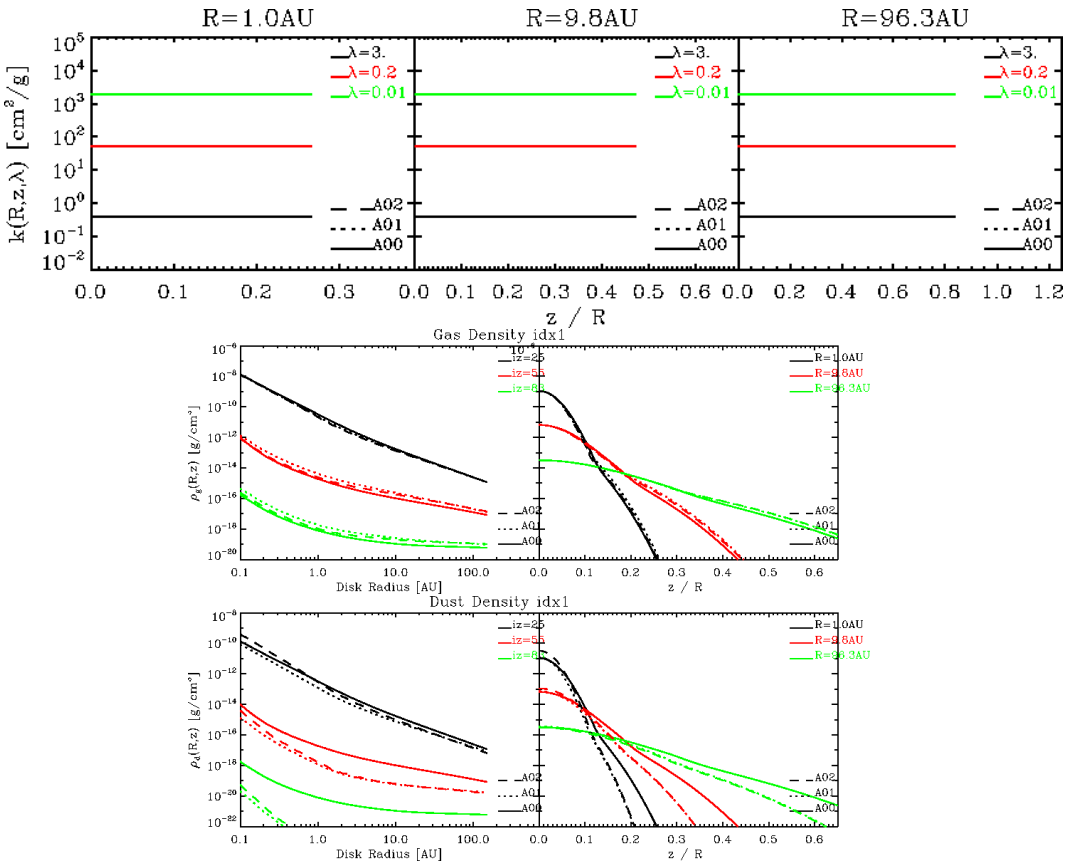

Figure 3.30: Some R and i_z sections of the dust opacity distributions at few wavelenghts (*top panels*) and the gas-dust density distributions (*bottom panels*).

In figure 3.31 we show the resulting characteristic heights profiles $H(R)$.

In figure 3.32 we show the resulting flaring index profile $\gamma(R)$.

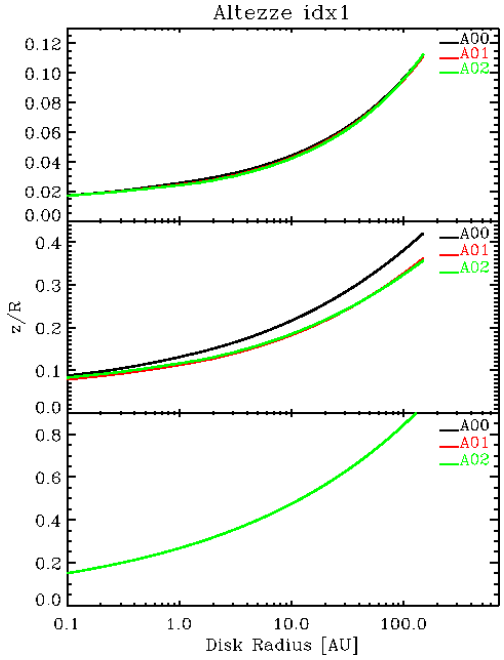

Figure 3.31: The characteristic disk heights profiles of the grid model A. *Top panel*: the pressure height scale $H_p(R)$. *Middle panel*: the disk surface height $z_s(R)$. *Bottom panel*: the deplection height $z_{depl}(R)$.

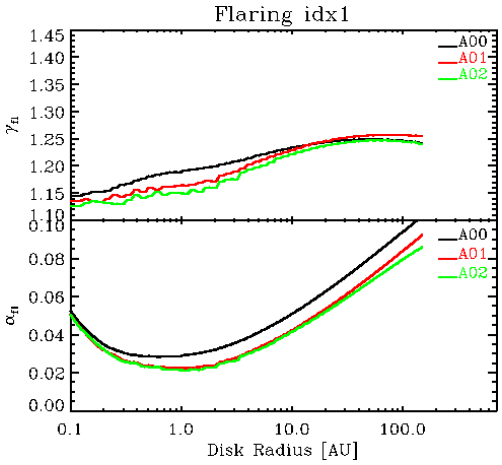

Figure 3.32: The flaring index $\gamma(R)$ (*top panel*) and incidente angle $\alpha_{irr}(R)$ profiles (*bottom panel*) of the grid model A.

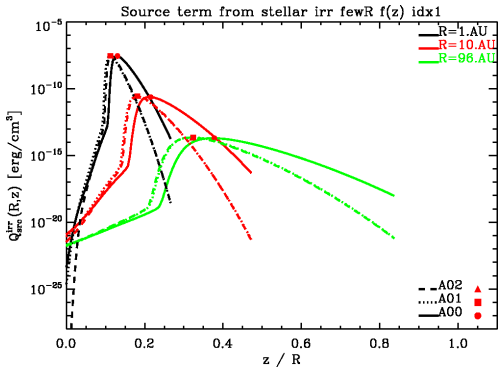

Figure 3.33: Some R sections of the source term from stellar irradiation $Q(R,z)$ of the grid model A.

In Fig. 3.33 we show the resulting dust absorbed energy $Q(R,z)$ from the primary stellar radiation. As we have already discuss in the annulus test (Sec. 3.10.1), the grains in the upper layers absorb, at a given z, more energy in model 0 then in model 1 because the heigher dust density in these layers (see Fig. 3.30 *bottom pannel*). For this reason, moreover, the surface height z_s ($\tau = 1$) move downward from model 0 to model 1: the stellar photons can deppler penetrate the annulus in model 1 and so the largest fraction of stellar radiation is absorbed closer to the midplane.

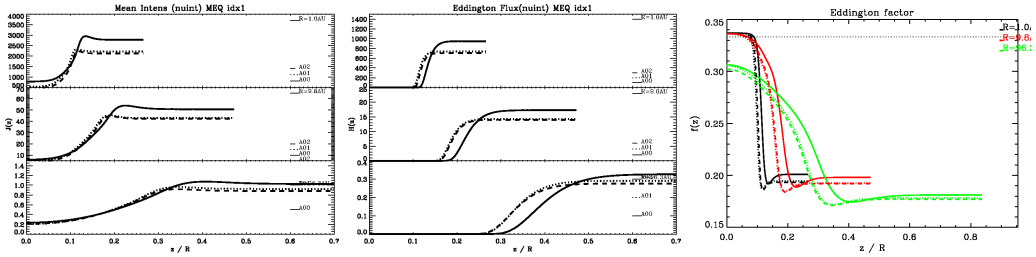

Figure 3.34: Some R sections of the characteristic quantities (as Fig. 3.25) of the radiation field of the grid model A.

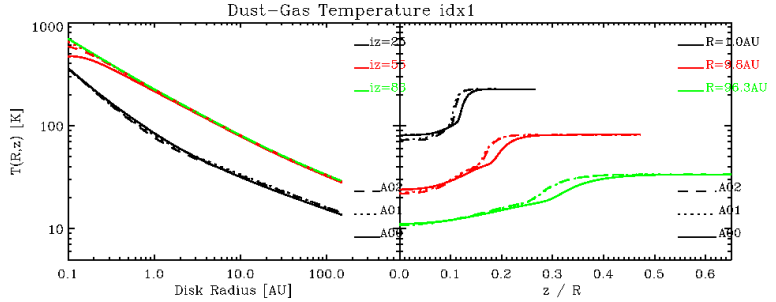

Figure 3.35: Some R and i_z sections of the gas-dust temperature distribution of the grid model A.

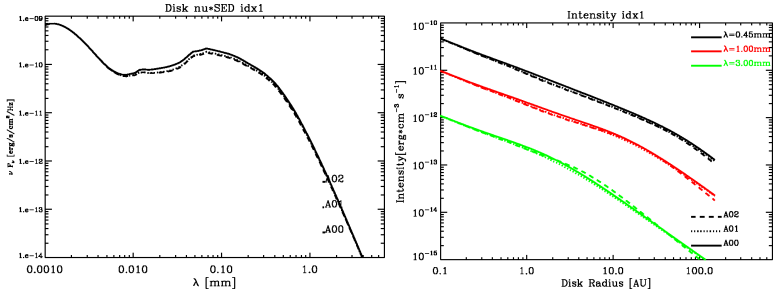

Figure 3.36: The SED and the intensity profile at few wavelenghts of the grid model A.

In Fig. 3.34 we show same characteristic quantities of the radiation field in the disk.

In Fig. 3.35 we show the resulting temperature distribution $T(R,z)$.
As we can see the temperature profile shift downward from model 0 to model 1. This because the surface height z_s move downward. At lower heights, as the stellar energy absorbed by the dust and the mean intensity of the reprocessed radiation increase from model 0 to model 1, we have an higher temperature in model 1 then in model 0. Near the midplane, however, the temperature is ...

In Fig. 3.36 we show the resulting intensity profile and SED.

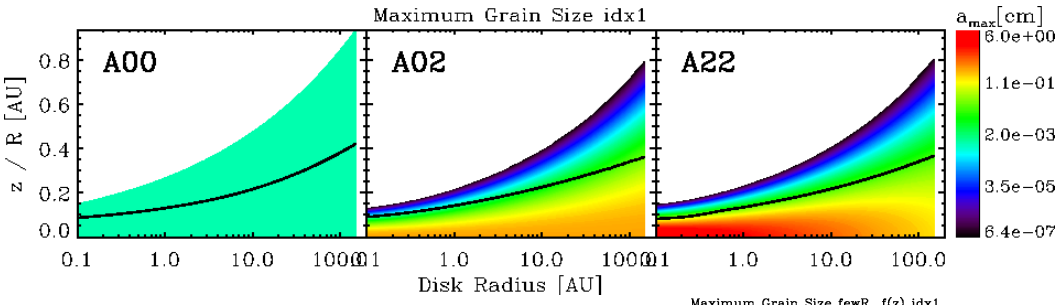

Grid model B			
$a_0[mm]$	**0.01**	0.2	3.0
b_R	**0.0**	0.2	0.5
b_z	**0.0**	0.23	0.23

Table 3.6: Parameters of the models grid for the maximum grain size distribution (Eq.3.71): b_R is the index of radial PL profile, b_z is the index of vertical Gaussian profile and a_0 is the maximum grain size value at the reference position $(40, 0)AU$. The **fiducial model** values are highlighted in bold face.

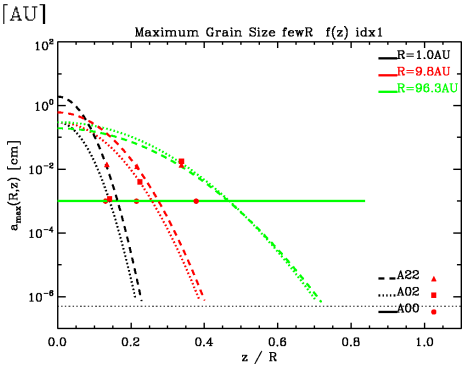

Figure 3.37: The final maximum grain size distribution in the (R, z) plane (*top panels*) and some R sections (*bottom panel*) of the grid model B.

3.12.2 Effects of spazial variation of the $a_{max}(R, z)$ distribution

In order to see the effect of the *maximum grain size* distribution $a_{max}(R, z)$, we construct a grid of 3 models (table 3.6) varing the parameters a_0,b_R and b_z of our parametrization (Eq. 3.71). The model B_0 corrispond to the fiducial disk model (Sec. 3.11) with constant $a_{max}(R, z)$ distribution, the model B_1 corrispond to a disks with z-variation and R-constant distribution and the model B_2 corrispond to a disks with same z distribution of B_1 but with also R-variation (Fig. 3.37). As consequence of the different parameter values, the deplection height profile $z_{depl}(R)$ change (see Fig. 3.37 *bottom pannel*). In this way, moreover, the mass of the disk decrease from model B_0 to model B_1 (as the dust-to-gas ratio distribution is fixed). However this decrease of mass is very low as we are just cutting the tail of the $\sim$ gaussian dust density distribution in the upper layer. So, as in the grid model A, we are compare 3 disks with the same dust mass ($M_d = 0.00106 M_\odot$).

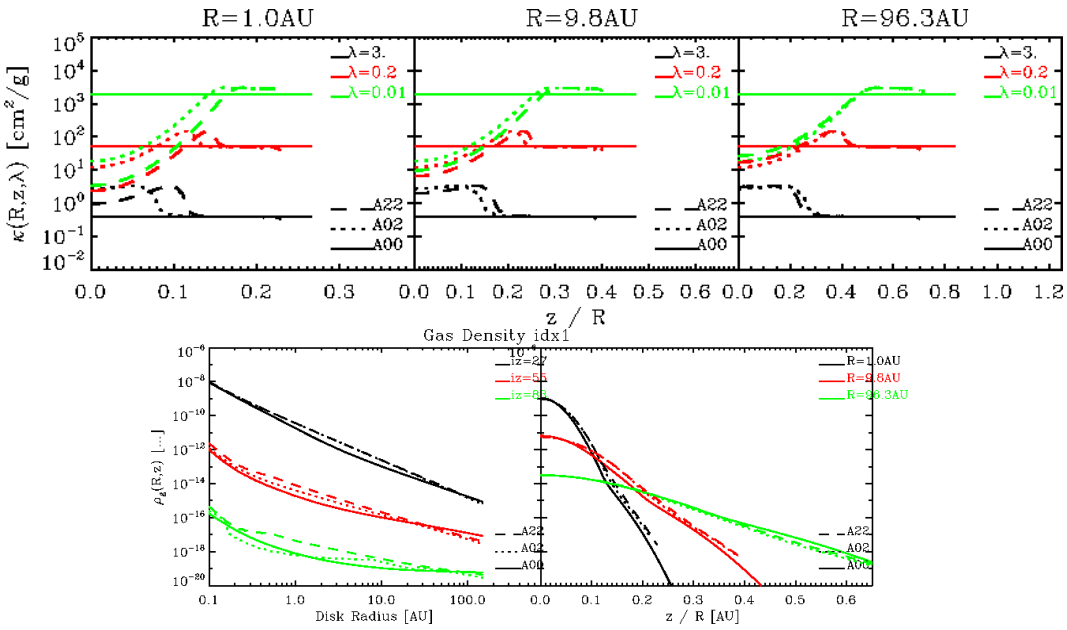

Figure 3.38: Some R and i_z sections of the dust opacity distributions at few wavelenghts (*top panels*) and the gas-dust density distributions (*bottom panels*).

In Fig. 3.38 (*top pannel*) we show the resulting dust opacity $k_\nu(R,z)$ at few wavelenghts. As we have already discuss in the annulus test (Sec. 3.10.2), different a_{max} distribution lead to different dust opacity distribution which present a peak in correspondence to a certain .....

In Fig. 3.38 (*bottom pannel*) we show for some models the resulting gas density distribution $\rho_g(R,z)$. How we can see the Rz-profile are almost the same for all the models. This is given by the fact that all the models have the same $\Sigma(R)$ distribution and at each radius the gas reach the hydrostatic equilibrium .....

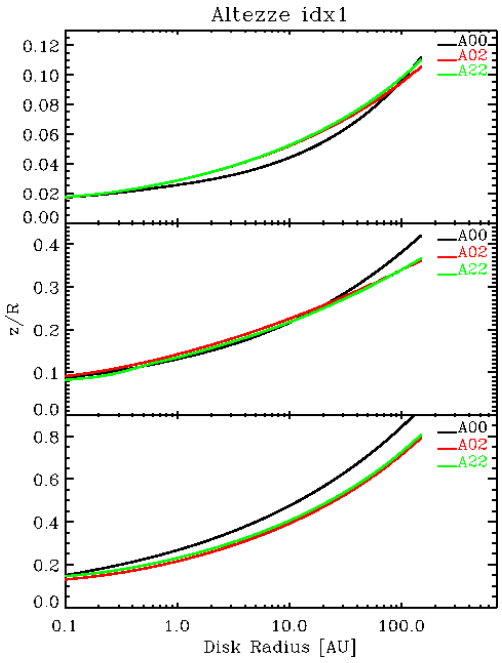

Figure 3.39: The characteristic disk heights profiles of the grid model B. *Top panel*: the pressure height scale $H_p(R)$. *Middle panel*: the disk surface height $z_s(R)$. *Bottom panel*: the deplection height $z_{depl}(R)$.

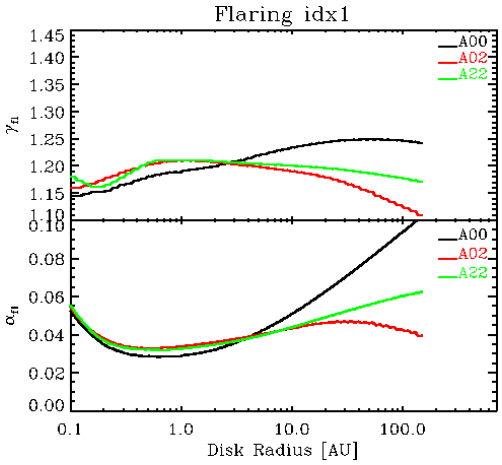

Figure 3.40: The flaring index $\gamma(R)$ (*top panel*) and incidente angle $\alpha_{irr}(R)$ profiles (*bottom panel*) of the grid model B.

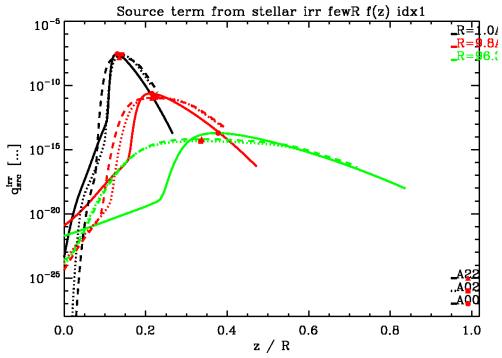

Figure 3.41: Some R sections of the source term from stellar irradiation $Q(R,z)$ of the grid model B.

In Fig. 3.39 we show the resulting characteristic heights profiles $H(R)$.

In Fig. 3.40 we show the resulting flaring index profile $\gamma(R)$.

In Fig. 3.19 we show the resulting dust absorbed energy $Q(z)$ from the primary stellar radiation.

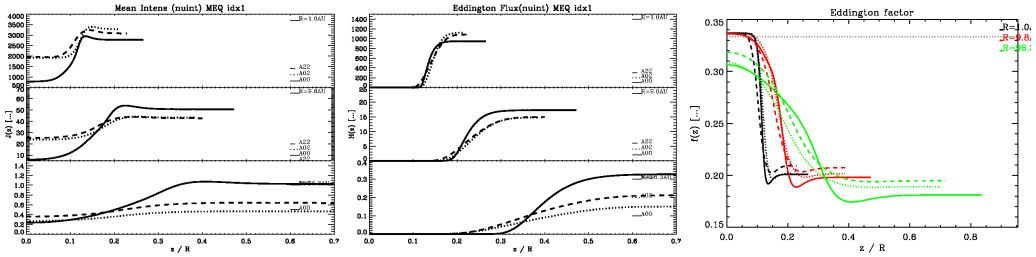

Figure 3.42: Some R sections of the characteristic quantities (as Fig. 3.25) of the radiation field of the grid model B.

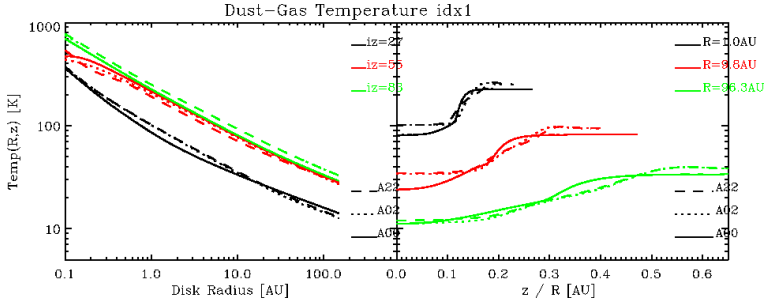

Figure 3.43: Some R and i_z sections of the gas-dust temperature distribution of the grid model B.

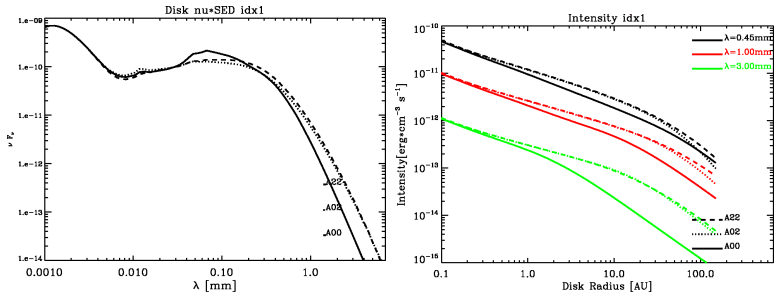

Figure 3.44: The SED and the intensity profile at few wavelenghts of the grid model B.

In Fig. 3.42 we show same characteristic quantities of the radiation field in the disk.

In Fig. 3.43 we show the resulting temperature $T(R,z)$.

In Fig. 3.44 we show the resulting intensity profile and SED.

Chapter 4

2-Layer Disk Approximation

Contents

In this chapter we present a more simplified circumstellar disk model which allow, as the 1+1D model, a self consistent computation of the structure of a steady passive thin disk in vertical hydrostatic equilibrium unter the single annulus approximation. This model resolve the radiative transfer problem in a more simple way adopting the 2-layer approximation of [30] Chiang & Goldreich (1997) with the modification of [38] Dullemond, Dominick & Natta (2001). Moreover, it include the possibility to have a radial variation of the dust properties, in particular, the possibility to modify the grain size distribution depending on the location in the disk. Given this possibility, we have used it to study the dust emission from the resolved disks around CQTau with the intention to investigate the radial variation of the dust properties in the disk trying to constrain the grain growth process.

The chapter is organized as follow: In Sec.4.1 we introduce the 2-layer disk model. In Sec.4.2 we analyse the basic equations and the adopted assumptions of the model. In Sec.4.3 we show the adopted (paramteric) distribution for the maximum grain size. In Sec.4.4 we show how we compute the Spectral Energy Distribution. In Sec.4.5, **??** we illustrate the basic results of the disk structure calculation of a fiducal disk model and we show how the different quantity describing the disk, affect its structure and emission properties. In Sec.4.6 we show the work of Ricci, Trotta, & al. (submitted) which investigate the effect of possible local optical thick regions on the mm-wave emission of protoplanetary disks. In Sec.4.7 we show the work of [21] Brinstiel, Ricci, Trotta, & al. 2010 which presented the comparison of mm-observations of disks around pre-main sequence stars in the Taurus-Auriga and Ophiuchus star-forming regions with predicted mm-SED based on a dust evolution model. In Sec.4.8 we show the result of fitting spatially resolved multi-frequency observations at mm-wavelenghts of the disk around CQ Tau with our two layer model.

4.1 Introduction: The 2-Layer Disk Model

As we have already described in the Sec. 3.1, disk models who better reproduce results consistent with observations, are characterized by a flared geometry and a vertical temperature stratification. The simplest way to solve this problem is adopting the so called '*two layers*' approximation first proposed by [30] Chiang & Goldreich 1997. These models solve the radiative transfer problem in a simple way (Fig. 4.1): the outer layer of the disk is directly irradiated by the stellar radiation which strik the surface at an angle α_{irr}. The stellar radiation energy is completely absorbed within a visible optical depth along the direction of the ray of unity ($\tau_V = 1$). Energy conservation requires that this absorbed radiation is re-emitted as infrared radiation, half of which is emitted away from the disk, while the other half is emitted towards the disk midplane. This downward emitted flux is absorbed by the disk interior and re-emitted once more in the infrared, though this time at longer wavelenght. So the disk vertical structure is composed of

1. a *surface layer* containing hot and small grains (from a fraction of μm up to

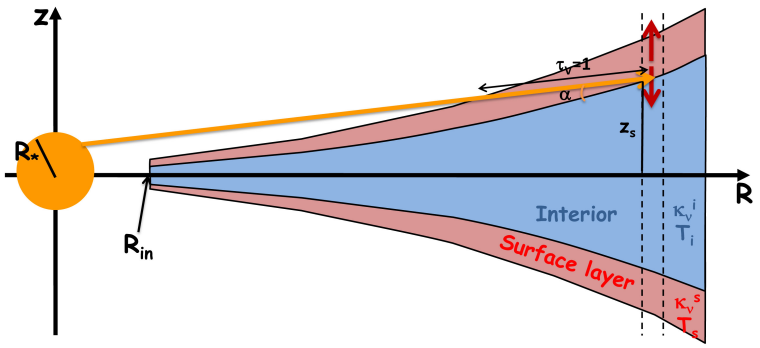

Figure 4.1: Radial slice of a flared 2-Layer passive disk and sketch of the radiative trasfer. Stellar radiation strikes the surface at an angle α and is absorbed within a visible optical depth of unity. Dust particles in this first absorbtion layer are superheated to the temperature T_s. About half of the emission from the superheated layer emerges as dilute blackbody radiation. The remaining half heats the interior to a temprature T_i

few μm) directily heated from the stellar radiation. It is characterized by a dust opacity k_ν^s and a dust temperature T_s.

2. a *internal layer* containing cooler grains than the surface one as they are heated by the radiation reprocessed by the surface layer. It is characterized by a dust opacity k_ν^i and temperature T_i.

Extensions has been done by [38] Dullemond, Dominick & Natta 2001 which include the effects of self-irradiation and self-shadowing and [74] Lachaume et al. (2003) which include the viscous heating.

These semi-analytical models allow a self-consistent computation of the disk structure solving the radiative transfer problem in simple way. The main advantage of these models is therefore the fast computation time of the disk structure which allow for an efficient fitting of visibility datasets even allowing for the computation of large grids of model parameters. In spite of the simple radiative transfer approach, this model retain a good accuracy in predicting the millimiter emission from the disk midplane ([41] Dullemond & Natta 2003).

4.2 Basic Equations and adopted assumptions

As the 1+1D model, the 2-layer model solve the disk structure assuming: (1) an axisymmetric disk in a single annulus approximation, (2) a geometrical thin disk, (3) a disk in vertical hydrostatic equilibrium between stellar gravity and gas pressure, with a flared geometry, (4) a passive disk, (5) gas and dust in thermal equilibrium ($T_d = T_g$). We remand to the previous chapter for the physical discussion of the above listed assumptions. Moreover the thermal disk structure is constructed in simple way without numerically solve the RT problem. Let's now discuss the ba-

sic equations of the model (see also [30, 31] Chiang & Goldreich 1997,2001, [38] Dullemond,Dominick & Natta (2001)).

4.2.1 Vertically isotherm interior disk

As we have seen in Sec. 3.3.2, a thin disk in vertical hydrostatic equilibrium must have a gas disk structure (ρ_g, P_g, T_g) that satisfy the pressure balance equation (3.30) which we rewrite here for clearity:

$$\frac{1}{\rho_g(R,z)}\frac{\partial P_g(R,z)}{\partial z} = -\frac{GMz}{R^3} \tag{4.1}$$

and we relate P_g, ρ_g and T_g by the equation of state of an ideal gas

$$P_g(R,z) = \frac{kT_g(R,z)}{\mu m_H}\rho_g(R,z) = c_s^2(R,z)\rho_g(R,z) \tag{4.2}$$

where $c_s = dP_g/d\rho_g = \sqrt{kT_g/\mu m_H}$ is the sound speed. The 2-layer disk model semplify the problem assuming a vertically isothermal interior gas ($T_i = T_i(R)$) and so a vertically constant sound speed ($c_s = c_s(R)$). In this way the Eq. 4.1 can be easily analitically solved leading to a gas density distribution with vertical gaussian profile

$$\rho_g(R,z) \quad = \quad \rho_{0g}(R)e^{-\frac{z^2}{2H_p(R)^2}} \tag{4.3}$$

where $\rho_{0g}(R)$ is the gas density at the midplane $z = 0$ and the quantity $H_p(R)$ denotes the pressure scale height of the gas given by

$$H_p(R) = \frac{c_s(R)}{\Omega_k(R)} \tag{4.4}$$

where $\Omega_k(R) = \sqrt{GM_*/R^3}$ is the local angular velocity. As show the Eq. 4.3, the pressure height represent the height at which the gas density (and so the gas pressure) decreased by a factor $e^{-1/2}$ and is therefore a good measure of the disk thickness. The disk aspect ratio is then

$$\frac{H_p(R)}{R} = \frac{c_s(R)}{u_k(R)} = \left(\frac{T_i(R)}{T_{gr}(R_*)}\right)^{1/2}\left(\frac{R}{R_*}\right)^{1/2} \tag{4.5}$$

where $T_{gr}(R_*)$ is the gravitational temperature at the stellar surface (T_{gr} is the temperture at which the thermal energy of a particle balance the gravitational energy $K_B T_{gr} = GM_*\mu m_H/R$). The above relation demostrates that requiring that the disk be thin is equivalent to requiring that the disk rotation is highly supersonic $u_k \gg c_s$. Moreover it shows the close relationship between the disk thickness and its midplane temperature, higher temperature = higher pressure height. The physical origin of this relation is easily understood: due to thermal pressure, the disk tends to expand in vertical direction, counteracting gravity, and hotter the disk, the stronger

this tendency is. In order to obtain the vertical structure of the disk at different radii, we thus need to know how does the temperature vary with radius.

For a vertically isothermal disk, the gas density distribution (4.3) can be also written in function of the gas surface density Σ_g. Infact using one properties of the gaussian function ($\int_{-\infty}^{+\infty} e^{-px^2}dx = \sqrt{\pi/p}$) one can see that the surface density is related to the disk midplane gas density ρ_{0g} by

$$\Sigma_g(R) \quad = \quad \rho_{0g}(R)\int_{-\infty}^{+\infty} e^{-\frac{z^2}{2H_p(R)^2}}dz = \sqrt{2\pi}H_p(R)\rho_{0g}(R) \tag{4.6}$$

In this way we can write the gas gaussian density distribution as

$$\rho_g(R,z) = \frac{1}{\sqrt{2\pi}}\frac{\Sigma_g(R)}{H_p(R)}e^{-\frac{z^2}{2H_p(R)^2}} \tag{4.7}$$

4.2.2 Extintion of the primary stellar radiation

As in the 1+1D Model, the extintion process of the primary stellar photons, when they enter into the disk and get absorbed by the dust, is modelled using a *irradiation-angle description* ([30] Chiang e Goldrich 1997). This recipe models the stellar irradiation in simple way: the stellar photons are inserted into the disk under angle $\alpha_{irr}(R)$ with respect to the disk's surface height $z_s(R)$, which is computed self-consistently from the disk geometry. As showed in Sec 3.4.1, the incidente angle of the photons for a flared disk is given by the Eq. 3.45 that we rewrite here for clearity:

$$\alpha_{irr}(R) = \frac{4}{3\pi}\frac{R_*}{R} + (\gamma(R)-1)\frac{z_s}{R} \tag{4.8}$$

where $\gamma(R) = \frac{d\log z_s}{d\log R}$ is the flaring index. This incidente angle is typically very small (around 0.05) and we can use the approximation [$\sin\alpha = \alpha$]. The flaring index is a number of order $\gamma \approx 2/9$. Its value is computed self-consistently during the iteration procedure. Usually the iteration is started with a guess for γ and updated after each few iteration steps. In order to avoid numerical instabilities, γ is always evaluated two radial gridpoints away from the point where it is used (see Appendix of [31] Chiang et al. 2001). It is important to note that a proper self-consistent computation of the flaring index γ is crucial if one wants to achieve energy conservation. The stellar flux impinging with this angle into the disk can be write:

$$F^*_{irr} = \phi \sin\alpha\frac{L_*}{4\pi R^2} = \phi\alpha\left(\frac{R_*}{R}\right)^2\sigma T_*^4 \tag{4.9}$$

where a stellar blackbody emission is assumed ($L_* = 4\pi R_*^2\sigma_B T_*^4$). The parametr ϕ takes into account possible shadowing effects i.e. point on the disk surface can not see the entire star. If the disk would stretch all the way to the star, the bottom half of the star would not be visible ($\phi = 1/2$). However, since we will consider disks with large inner holes, we can ignore this effect ($\phi = 1$).
As the photons enter the disk, they get completely absorbed by the dust in the

very tenuous upper layer of the disk, the *surface layer*. This layer is locate above the surface height $z_s(R)$ which is define as the height z above the midplane where the visual optical depth along the direction of the incident stellar light is egual 1 ($\tau_V = \tau_V^{\perp}/\sin\,\alpha_{gr} = 1$). Unlike the 1+1D model (see Eq. 3.47), the 2-layer model define the vertical optically depth $\tau^{\perp}$ using a mean dust opacity:

$$\tau^{\perp}(R) = k_P^s(R, T_*) \int_z^{\infty} \rho_d(R, z) dz \tag{4.10}$$

where $k_P^s(T_*)$ is the Planck mean opacities (per unit of dust matter) of the surface layer dust at stellar temperature. Under the assumption of constant (0.01) dust-to-gas ratio and with a Gaussian vertical gas density profile (Eq. 4.7), the equation $\tau_V = 1$ can be written:

$$1 - \mathrm{erf}\left(\frac{\chi_{hh}(R)}{\sqrt{2}}\right) = \frac{2\alpha(R)}{\Sigma_g(R) k_P^s(R, T_*)} \tag{4.11}$$

where $\chi_{hh} = z_s/H_p$ and $\mathrm{erf}(x)$ is the error function ($\mathrm{erf}\,(x) = \frac{2}{\sqrt{\pi}} \int_{-\infty}^{x} e^{-x^2} dx$). ($k_P^s$ per unit of gas matter). Once obtained χ_{hh}, the surface height is given by:

$$\frac{z_s}{R} = \frac{z_s}{H_p}\frac{H_p}{R} = \chi_{hh} \left(\frac{T_i}{T_c}\right)^{\frac{1}{2}} \left(\frac{R}{R_*}\right)^{\frac{1}{2}} \tag{4.12}$$

4.2.3 Disk thermal structure

The 2-layer model solve the disk thermal structure in a simple way. The temperature of the dust particles in the surface layer is obtained simply from the optically thin expression. Infact, since the disk surface layer is defined as the layer of matter in direct sight of the central star up to $\tau_V = 1$ (see Sec. 4.2.2), the dust temperature in this layer can be estimated as:

$$T_s(R) = \frac{1}{\varepsilon_s^{1/4}} \left(\frac{R_*}{2R}\right)^{1/2} T_* \tag{4.13}$$

where ε_s is the ratio of the Planck mean opacities of the surface dust at T_s and T_*.

The temperature of the dust particles in the interior layer is determined in the follow way. From energy conservation, this heated surface dust particle will re-emit at low wavelenght half away from the disk and half towards the disk midplane. This flux re-emitted towards the interior is then

$$F_s^{emit}(R) = \frac{1}{2} F_{irr}^{*} = \frac{\phi\alpha}{2} \left(\frac{R_*}{R}\right)^2 \sigma T_*^4 \tag{4.14}$$

This flux is then assorbed by the interior dust particle and re-emitted once more at longer wavelenght. In the calculation of the flux absorbed by the interior dust particles (heating radiation), the 2-layer model take in accounts for the possibility that the disk interior is not full optically thick to the radiation from the surface

layer. Only a fraction ψ_s (between 0 and 1) of the emitted flux from surface layer will be absorbed by the interior. So the interior will absorb a flux given by:

$$F_i^{abs}(R) = \psi_s F_s^{emit} = \psi_s \frac{\phi\alpha}{2} \left(\frac{R_*}{R}\right)^2 \sigma T_*^4 \tag{4.15}$$

where the fraction ψ_s is:

$$\psi_s(R) = \frac{\int_0^\infty B_\nu(T_s) k_\nu^s \left[1 - e^{-\Sigma k_\nu^i}\right] d\nu}{\int_0^\infty B_\nu(T_s) k_\nu^s d\nu} \tag{4.16}$$

The limits for high and low optical depth are respectively $\psi_s(R) = 1$ (for $\Sigma k_P(T_s) \gg 1$) and $\psi_s(R) = \Sigma k_P(T_s)$ (for $\Sigma k_P(T_s) \ll 1$). In the calculation of the emitted flux (cooling radiation) the 2-layer model take in accounts for the possibility that the disk interior is not full optically thick to its own radiation. Only a fraction ψ_i (between 0 and 1) of the emitted flux from interior dust will be absorbed by themself. So the interior will emit a flux given by:

$$F_i^{emit}(R) = \psi_i \sigma T_i^4 \tag{4.17}$$

where the fraction ψ_i is:

$$\psi_i(R) = \frac{\int_0^\infty B_\nu(T_i) \left[1 - e^{-\Sigma k_\nu^i}\right] d\nu}{\int_0^\infty B_\nu(T_i) d\nu} \tag{4.18}$$

The limits for high and low optical depth are respectively $\psi_i(R) = 1$ (for $\Sigma k_P(T_i) \gg 1$) and $\psi_i(R) = \Sigma k_P(T_s)$ (for $\Sigma k_P(T_i) \ll 1$). The midplane temperature is then determined by equating the thermally emitted flux (Eq. 4.17) to the absorbed flux (Eq. 4.15)

$$T_i(R) = \left(\frac{\phi\alpha}{2} \frac{\psi_s}{\psi_i}\right)^{1/4} \left(\frac{R_*}{R}\right)^{1/2} T_* \tag{4.19}$$

4.3 Maximum grain size distribution

Numerical simulations of cougulation/sedimentation dust models in circumstellar disks predict that grains grow, migrate and frament in the disk and predict variation of dust properties as a function of position, disk age and physical properties. As we have done in the 1+1D disk model, we incorporate in our 2-layer disk model, the possibility to have, in parametric way, a spatial variation of the maximum grain size distribution. We will assume here, for semplicity, that the gas and dust are well mixed throughout the disk with a constant (0.01) dust-to-gas ratio.

We adopt for $a_{max}(R, z^{(i,s)})$ distribution a radial power law profiles (both for interior $z^{(i)}$ and surface $z^{(s)}$ layer)

$$a_{max}(R, z^{(i,s)}) \quad = \quad a_{0max}^{i,s} \left(\frac{R}{R_0}\right)^{b_R^{i,s}} \tag{4.20}$$

where $a_{0max}^{i,s}$ is the maximum grain size value at the reference position R_0, $b_R^{i,s}$ is the index of the radial power law profile. The maximum grain size distribution $a_{max}(z)$ throughout the disk is governed by the process of grain growth and the subsequent settling of the large grains to the midplane. This quantity contribuite to specify the dust opacity distribution $k_\nu(z)$ (Eq. 2.10) and therefore regulate the radiative transport in the disk.

4.4 Spectral Energy Distribution

Once the disk structure is know, we can compute intensity profile and Spectral Energy Distribution (SED) from the circumstellar disk. As first approximation, the SED of a circumstellar disk can be modeled as the sum of the contribution of annuli and at each annulus one combine the flux arising from the disk interir F_ν^i with the flux from the disk surface layer F_ν^s. These are expressed respectively by

$$F_\nu^i = \frac{2\pi \cos i}{d^2} \int_{R_{in}}^{R_{out}} B_\nu(T_i(R)) \left[1 - e^{-\frac{\Sigma(R) k_\nu^i(R)}{\cos i}}\right] R dR \tag{4.21}$$

$$F_\nu^s = \frac{2\pi}{d^2} \int_{R_{in}}^{R_{out}} B_\nu(T_s(R)) \Delta\Sigma(R) k_\nu^s(R) \left[1 + e^{-\frac{\Sigma(R) k_\nu^i(R)}{\cos i}}\right] R dR \tag{4.22}$$

([38] Dullemond et al. 2001, [31] Chiang et al. 2001) where d is the distance to the source, i the disk inclination angle with respect to the plane of the sky ($i = 0$ means face-on), $\Delta\Sigma$ is the column density in the disk surface and $k_\nu^{i,s}$ are the dust opacityat the disk midplane and surface.

Fiducial Disk Model			
STAR	$L_* = 0.3L_\odot$ $M_* = 0.5M_\odot$ $T_* = 3000°K$	DISK DOMAIN	$R = [0.1 - R_{th}]AU$
GAS COMPOSITION	$\mu = 2.3$ (H_2,He mixture)	GAS SURFACE DENSITY	$\gamma = 1.0$ $R_{tr} = 30AU$ $\Sigma_{tr} = 10g/cm^2$
DUST COMPOSITION	7% silicates 21% carbonaceous 42% water ice 30% vacuum	MAXIMUM GRAIN SIZE	$a_0^i = 0.1cm$, $b_R^i = 0$ $a_0^s = 1\mu m$, $b_R^s = 0$

Table 4.1: Parameters of the fiducial disk model.

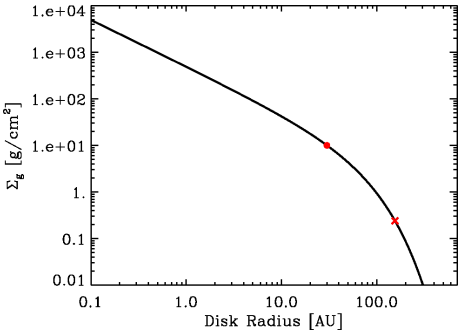

Figure 4.2: The gas surface density $\Sigma_g(R)$ distributions of the fiducial disk model.

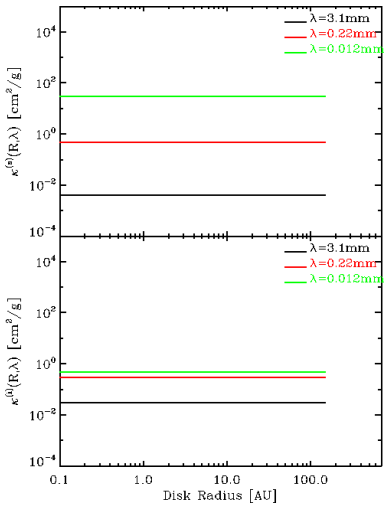

Figure 4.3: The dust opacity $k_\nu^{(i,s)}(R)$ distributions at few wavelenghts of the fiducial disk model. (top)....(bottom)

4.5 Disk structure and emission

To illustrate the basic results of the disk structure calculation, we construct a **fiducial disk model** (table 4.1) for a typical T Tauri star. We consider a disk with an inner hole of stellocentric radius $0.1AU$. We assume here a gas surface density $\Sigma_g(R)$ give by the the self-similar solution for a viscous thin disk (Eq. B.10). Due to the radial exponential fall-off of this surface density (see figure 4.2), the very outermost disk regions become optically thin to the stellar radiation and the two-layer approximation can not be applied. This transition to this optically thin regime occurs at a certain radius R_{th} (the red cross in the figure) and we adopt this radius as

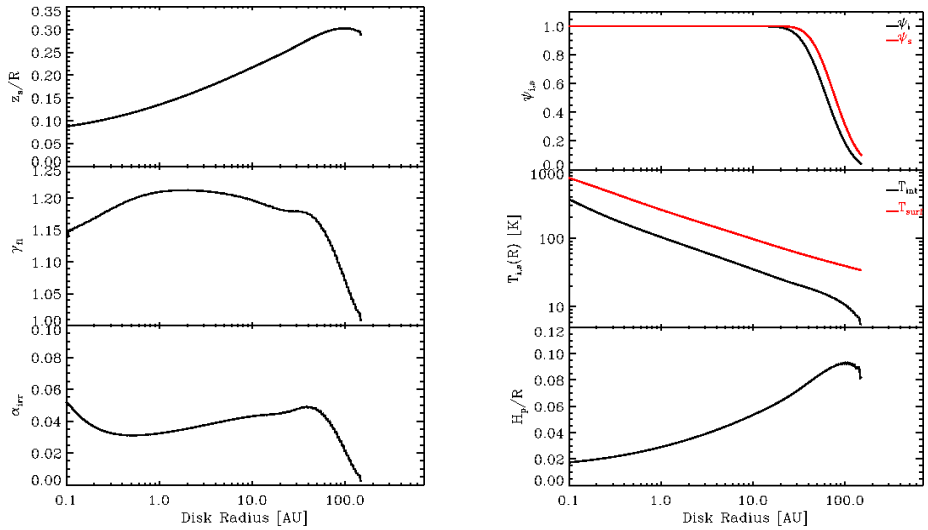

Figure 4.4: Characteristic quantities of the disk structure calculation for the 2-layer model. (*Left panels*) are the surface height z_s/R, the flaring index γ_{fl} and the incident angle α_{irr}. (*Right panels*) are the parameters $\psi_{(i,s)}$, the midplane and surface temperature $T_{(i,s)}$ and the pressure height H_p/R.

the disk outer radius ($R_{out} = R_{th}$). This model corrisponds to a disk with vertical absorbtion optical depth on the midplane (at visible wavelenght $\lambda_V = xx$) go from $\tau_V = xx$ at inner radius to $\tau_V = xx$ at the outer disk, a gas mass $M_{disk}^{gas} = 0.xxM_\odot$ and dust mass 100 time less. Our computations adopt a logarithmic grid of 300 points in radial direction, a logarithmic grid in wavelenght of 100 points covering a domain $0.1\mu m \leq \lambda \leq 1cm$ and a logarithmic grid in grain size of 200 points covering a domain $0.005\mu m \leq a \leq 10cm$.

In figure 4.3 we show the resulting dust opacity $k_\nu^{(i,s)}(R)$ at few wavelenghts. Because of the constant dust size distribution in radial direction, both the interior and surface layer have therefore a radially constant dust opacity. As a consequence of the two different a_{max} values in the two layers ($0.1cm$ in the interior and $10\mu m$ in the surface), we have different values of dust opacity: the dust population in the surface is more opaque at short wavelenght then the interior dust (green line) mentre at long wavelengts (black line) the interior dust population is more opaque then the surface dust.

In figure 4.4 (*left panel*) we show the result of the flaring angle calculation.

In figure 4.4 (*right panel*) we show the resulting temperature $T(R)$.

In the bottom pannel finaly we show the pressure height H_p.

In figure 4.5 we show the resulting gaussian gas density distribution $\rho_g(R, z)$. Clearly the gas density distribution decrease in radial direction as we have choosen a gas surface density with $\gamma > 0$. At each position (R, z) the dust density has a

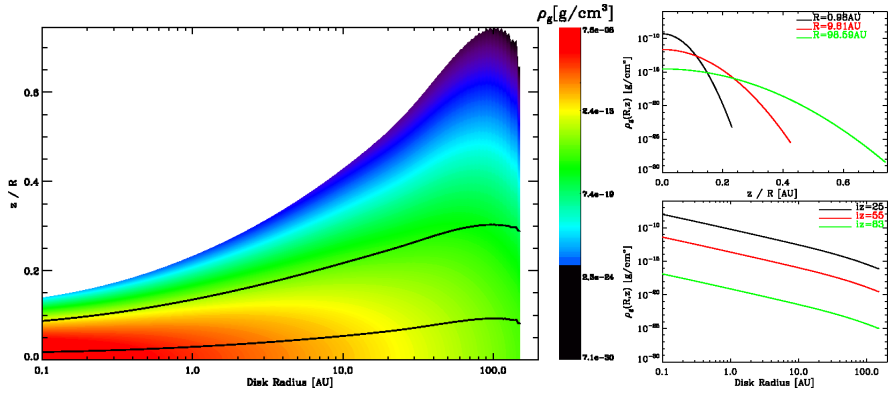

Figure 4.5: The gas density distribution $\rho_g(R, z)$ of the fiducial disk model.

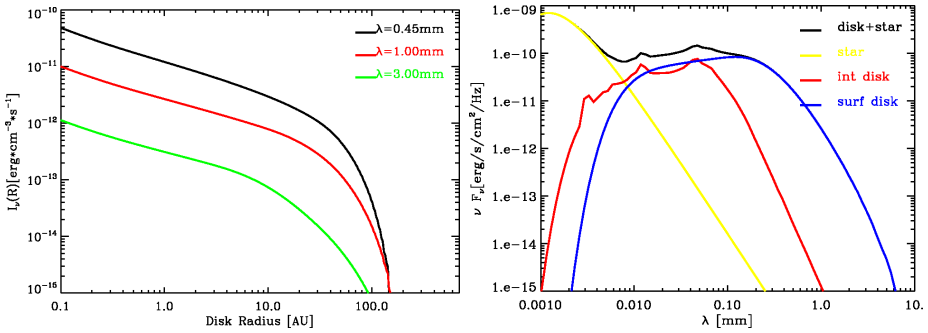

Figure 4.6: The intensity profile at few wavelenghts (*left panel*) and the SED (*right panel*) of the fiducial disk model.

value 100 time less the the gas density because of the constant (0.01) dust-to-gas ratio distribution.

In figure 4.6 (*left panel*) we show the resulting intensity profile. As the surface density falling off exponentially at large radii, the intensity profile also decrease exponentially in the outer disk.

Figure 4.6 (*right panel*) show the resulting SED. The contribution to the SED from the central star (red line) dominates at $\lambda \sim 1\mu m$. At wavelenght of few μm to $\sim 60\mu m$ emition arises from the hot surface layer of the disk (red line). The contribution to the SED from the disk interior (blue line), which at a given radius is cooler then disk surface by a factor ~ 3, dominates at $\lambda \gtrsim 100\mu m$.

4.6 The Effect of the local optically thick regions in the long-wave emission of young circumstellar disk

Ricci, Trotta, Testi, Natta, Isella, Wilner 2011 (submitted)

Multi-wavelength observations of protoplanetary disks in the sub-millimeter continuum have measured spectral indices values which are significantly lower than what is found in the diffuse interstellar medium. Under the assumption that mm-wave emission of disks is mostly optically thin, these data have been generally interpreted as evidence for the presence of mm/cm-sized pebbles in the disk outer regions.

In this work we investigate the effect of possible local optical thick regions on the mm-wave emission of protoplanetary disks. A significant local increase of the optical depth in the disk can be caused by the concentration of solid particles, as predicted by different physical mechanisms potentially acting in the disk. We calculate which filling factors and overdensities these optically thick would need to have for significantly affecting the mm-fluxes of disks, and we discuss their physical plausibility in real disk.

We find that optically thick regions characterized by relatively small filling factors can reproduce the mm-data of young disks without requesting emission from mm/cm-sized pebbles. However, these optically thick regions require dust overdensities much larger than what predicted by any of the physical processes proposed in the literature to drive the concentration of solids. We find that only for the most massive disks it is possible and plausible to imagine that the presence of optically thick regions in the disk is responsible for the low measured values of the mm spectral index. For the majority of the disk population, optically thin emission from a population of large mm-sized grains remains the most plausible explanation. The results of this analysis further strengthen the scenario for which the measured low spectral indices of protoplanetary disks at mm wavelengths are due to the presence of large mm/cm-sized pebbles in the disk outer regions.

4.6.1 Disk Model description

In order to derive the disk structure we adopted the 2-layer disk model of [30] Chiang & Goldreich (1997) with the modifications of [38] Dullemond, Dominik & Natta (2001). The model requires as input a set of parameters for the central star and the disk. Here we consider disks around a PMS stars with a mass of $0.5 M_{\odot}$, bolometric luminosity of $0.9 L_{\odot}$ and effective temperature of 4000 K, which are typical values for the sample of low-mass PMS star in [102, 103, 103] Ricci et al. (2010a, 2010b, 2011) in Taurus, Ophiuchus and Orion Nebula Cluster forming regions.

As disk surface density distribution we adopt the similarity solution for a viscous evolution of thin accretion disk ([81] Lynden-Bell & Pringle 1974) written in the form

$$\Sigma_{dust}(R) = \Sigma_0 \left(\frac{R}{R_c}\right)^{-\gamma} exp\left[-\left(\frac{R}{R_c}\right)^{2-\gamma}\right] \tag{4.23}$$

with values of the Σ_0, γ and R_c parameters in the ranges observationally constrained by sub-arcsec angular resolution imaging of young protoplanetary disks in the sub-mm ([66] Isella et al. 2009, [6, 7] Andrews et al. 2009, 2010).

We compute the dust opacity coefficient adopting the same dust model as [20] Birnstiel et al. (2010a), [102, 103] Ricci et al. (2010a, 2010a), i.e. porous composite spherical grains made of (vol. perc.) 7% astronomical silicates, 21% carbonaceous material and 42% water ice and 30% vacuum. To estimate the optical properties of such composite particles we use the Bruggeman effective medium theory ([27] Bruggeman 1935) to calculate an effective dielettric function ε_{eff} for a composite grain and then we use this function in the Mie Theory to derive the dust absorbtion efficiency $Q_{abs}(a, \nu)$. The Mie coefficients are calculate using the complex optical constant of individual components that are taken from ([118] Weingartner & Drain 2001) for astronomical silicates, from ([124] Zubko et al.1996) for carbonaceous material and from ([115] Warren 1984) for water ice. We adopt a power-law grain size distribution with slope q

$$n(a) \propto a^{-q} \tag{4.24}$$

truncated between the minimum and maximum grain sizes a_{min} and a_{max}, respectively. Since in this work we want to investigate the impact of local optically thick regions in the outer disk on the slope of the mm-SED without invoking the presence of large mm-sized grains, we consider here a size distribution which has been proposed by [88] Mathis et al. (1977) to fit extinction measurements of the interstellar medium. For this ISM-like dust $a_{max} \approx 0.1\mu m$, $a_{min} \ll a_{max}$, and $q \backsimeq 3.5$. Note however that, for a given grain chemical composition, as long as $a_{max} < 0.1mm$ the dust opacity coefficient k_ν at mm wavelengths stays unchanged and does not even depend on q (see Fig. 3 in [102] Ricci et al. 2010a). Therefore, the dust model adopted here refers to a more general dust population in which only grains smaller than $\sim 0.1mm$ are present.

In order to investigate the impact of possible local optically thick regions in the outer disk on the mm emission properties we consider a disk containg at each annulus a fraction $f(R)$ of area which is optically thick at all the wavelengths. The total flux density of a such system can be written as

$$F_\nu^i = \frac{2\pi \cos i}{d^2} \int_{R_{in}}^{R_{out}} B_\nu(T_i(R)) \left[f(R) + (1 - f(R)) \left(1 - e^{-\tau_\nu(R)} \right) \right] R dR \tag{4.25}$$

In this way, a completely optically thick disk corrispond to have $f(R) = 1$ and a disk without optically thick region corrispond to $f(R) = 0$ (we call this second case 'unperturbed' disk).

In order to make these regions optically thick, a certain quantitity of dust mass has to be added to the disk. A simple way to estimate this mass is to calculate the surface density which has to be present in the added regions to give them an optical depth of about 1 at the longest wavelength considered in this work, i.e. 3mm, and then integrate over the disk area covered by the filling factor f. This represents actually a lower limit for the mass which has to be present in the added regions to

make them optically thick: if more mass is put onto those regions this does not have a significant effect onto the SED. Therefore, the dust surface density in the optically regions is given by the condition

$$\tau_{3mm} \approx \Sigma^f_{dust}\kappa_{3mm} \approx 1 \rightarrow \Sigma^f_{dust} \approx \frac{1}{\kappa_{3mm}} \tag{4.26}$$

which implies that Σ^f_{dust} does not dipend on the stellocentric radius. As concequence of this, if we consider a presence of optically thick region between the radii R_{in} and R_{out}, the total dust mass in this region is

$$M^f_{dust} = f\int_{R_{in}}^{R_{out}} \Sigma^f_{dust} 2\pi R dR = \pi f \Sigma^f_{dust}(R^2_{out} - R^2_{in}) \tag{4.27}$$

4.6.2 Results

In order to investigate the effect of the local optical thick regions on the mm-wave emission we construct a grid of models varing faring the filling factor f and the parameters Σ_0, γ and R_c of the surface density. We will treat first the simplest case of $f(R)$ which is constant with the radius (Sec. 4.6.2.1) and then we will consider for $f(R)$ a family of step functions which are non-zero only within specified regions in the disk (Sec. 4.6.2.2).

For each model we compute the mm-flux density (Eq. 4.25) and we estimate how much mass has to be added to the disk in order to make a fraction of the disk surface optically thick even at mm-wavelengths (Eq. 4.27) and we compare the predicted mm flux and spectral slope with those measured by [102, 103, 103] Ricci et al.(2010a, 2010b, 2011) for 49 disks in Class II YSOs in the Taurus, Ophiuchus and Orion star forming regions.

4.6.2.1 Case of a constant f

We consider here the case of optically thick regions present at each radius (from R_{min} to R_{max}) with constant filling factor. Each pannels in Fig. 4.7 show the model predictions (black symbols) on the $F_{1mm} - \alpha_{1-3mm}$ diagram for a given couple of the (γ, R_c) parameter for the disk unperturbed structure and for different values of the filling factor f and of the dust mass M^{unp}_{dust} [1]. The values of the parameters considered in this work for the unperturbed disk, i.e. $\gamma = 0, 1$ and $R_c = 20, 200AU$, lay at the limits of the ranges for these parameters as recently constrained by a high-angular resolution survey of about 30 protoplanetary disks in the sub-mm ([66] Isella et al. 2009, [6, 7] Andrews et al. 2009, 2010).

In each panel the points with $f = 0$ represent the emission of the unperturbed disk, i.e. without any addition of optically thick regions. The dependence of the flux density at 1 mm on the dust mass is due to the fact that the bulk of the material reside in the outer disk regions where the surface density is relatively low and the

[1] The value of the normalization factor in equation 4.23 i.e. Σ_0, is set after the (unperturbed) dust mass in the disk

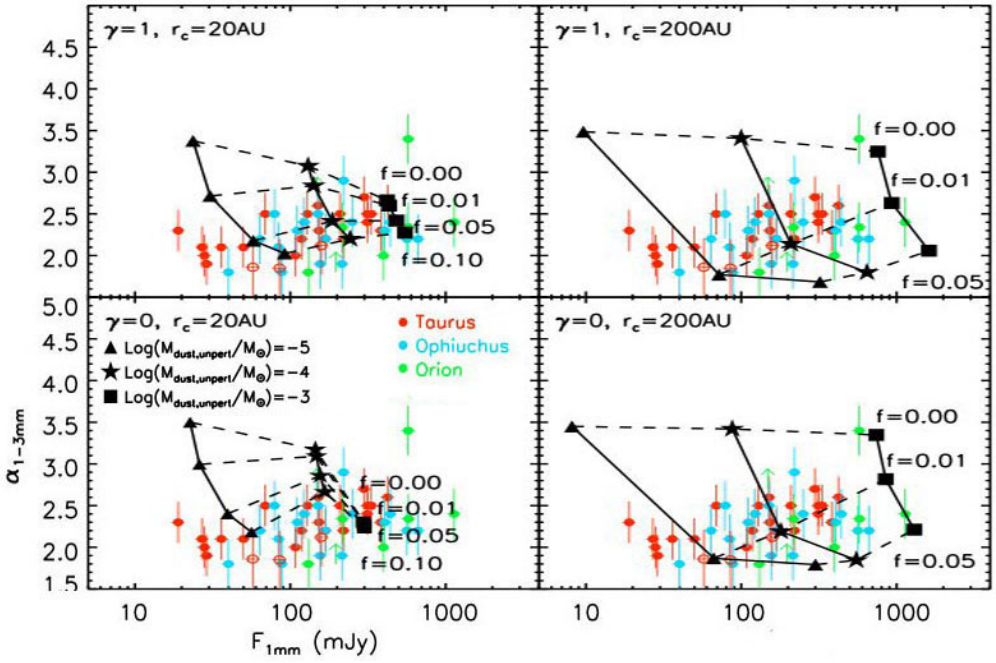

Figure 4.7: Flux density at 1mm vs. spectral index between 1 and 3mm. Red, blue and green points represent observational data of disks in Class II YSOs in Taurus, Ophiuchus and OrNebula Cluster, respectively. Black symbols show the models predictions for different unperturbed dust mass: triangle for $10^{-5}M_{\odot}$, stars for $10^{-4}M_{\odot}$ and squares for $10^{-3}M_{\odot}$ and in the case of optically thick regions present at each radius.

emission optically thin. In terms of the spectral index α_{1-3mm} the points with $f = 0$ lay at relatively large values of about $3-3.5$. This is due to the adopted dust model made of small grains, for which the value of the spectral slope β of the dust opacity coefficient is about 1.5. The slight decrease of α_{1-3mm} with increasing dust mass is given by the fact that for disks that are massive enough the innermost disk regions ($R < 10-20AU$) are so dense that the emission from these regions becomes optically thick in the sub-mm, and this has the effect of making the SED shallower. Note however that the points with $f = 0$ do not get into the area of the $F_{1mm} - \alpha_{1-3mm}$ diagram which contains the bulk of the observational data. In particular the models presented here with $f = 0$ overpredict the observed spectral index α_{1-3mm}.

The effect of increasing the filling factor f of the optically thick regions has always the same kind of signature in the (F_{1mm},α_{1-3mm})-plane: the absolute flux in the (sub-)mm increases because more and more optical depth is added into the system, whereas the spectral index tends to decrease and approach the value of about 2, as exspected for completely optically thick emission in the Rayleigh-Jeans regime.

The main result shown in Figure 4.7 is that, for most of the unperturbed disk structures, relatively low values of the filling factor ($f < 0.05$) are required to

explain the bulk of the data. The most significant variation of the mm-fluxes with the properties of the unperturbed disk comes when the characteristic radius changes from 20 to 200 AU (see left and right panels, respectively). With $R_c = 20AU$ the surface density is more concentrated in the inner disk than in the $R_c = 200AU$ case. As a consequence of this the impact of the optically thick inner regions to the total emission is more evident (see e.g. the low α_{1-3mm}-value of the model with $f = 0$ and a dust mass of $10^{-3}M_{\odot}$ for the unperturbed disk structure). However, the fluxes of the disks with $f > 0$ do not dramatically depend on the structure of the unperturbed disk. This is due to the fact that in most of the cases already for $f \approx 0.05$ the total disk emission becomes dominated by the added optically thick regions.

What varies strongly with the unperturbed disk structure at a given f is the mass which has to be included in these added regions in order to make them optically thick. The total dust mass (Eq. 4.27) in this case can be written

$$M^f_{dust} \approx \pi f \Sigma^f_{dust} R^2_{out} \tag{4.28}$$

i.e. the total dust mass in the optically regions depends quadratically on the largest radius in which these regions are present in the disk, namely 300 AU in this simulation. For the dust considered, $\kappa_{3mm} \approx 0.45 cm^2/g$ and $M^f_{dust} \approx f \times 0.07 M_{\odot}$. This means that even in the case of the model with the largest unperturbed mass in dust ($10^{-3}M_{\odot}$) and with the lowest value of the filling factor f considered here (0.01), the optically thick region contain at least 70% of the mass in the unperturbed disk. This ratio then increases linearly with f and decreases with increasing the dust mass of the unperturbed disk. This argument clearly shows that in order to have optically thick regions of the kind discussed so far in the outer disk a very strong redistribution of dust particles has to occur in the disk.

4.6.2.2 Case of $f(R)$ as a step function

We consider here the result of optically thick regions localized in smaller areas of the disk. In particular, we discuss four cases in which $f(R)$ is a step function with values greater than 0 between 10 and 20 AU, 30 and 40 AU, 50 and 60 AU, 80 and 90 AU, respectively. We consider annuli with a width of 10 AU because the physical mechanisms proposed so far to concentrate particles locally in the disk typically act on these length scales or smaller (see 4.6.3). The different central radii chosen for the annuli allow us to investigate how the location of the optically thick regions in the disk can affect its total sub-mm emission.

The four panels in Fig. 4.8 show the model predictions (black symbols) on the $F_{1mm} - \alpha_{1-3mm}$ diagram for disk with such localized optically thick regions and an unperturbed disk structure with $\gamma = 0.5$ and $R_c = 60AU$, which are the median values for disks imaged at high-angular resolution.

The optically thick regions can have a signficant impact onto the global mm-SED even if they are concentrated in rings with the relatively small width of 10 AU. The effect is stronger for the disk with lower masses because of the higher constrast in

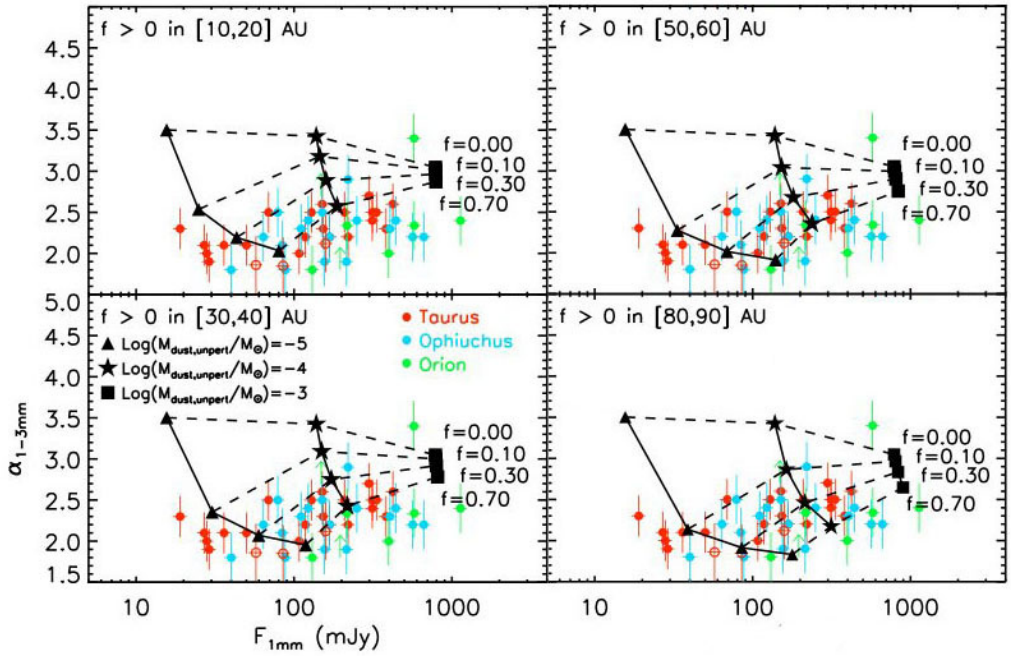

Figure 4.8: Like in Fig. 4.7 but in the case of optically thick regions localized in annuli of 10 AU-width, with inner and outer radii indicated in the top left corner of each panel and an unperturbed structure of the disk is characterized by $\gamma = 0.5$ and $R_c = 60AU$.

optical depth between the unperturbed disk and the optically thick regions. For the same reason, i.e. the contrast with the unperturbed disk structure, and for the fact that the area of an annulus of a given width scales linearly with the central radius of the annulus, at a given filling factor f inside the ring, the effect of the optically thick regions is the largest in the ring which is the furthest from the star, i.e. between 80 and 90 AU. Note that to reproduce the bulk of the data, larger fractions f are needed than in the $f(R) = const$ case. This is because in the case of optically thick emission, apart for the temperature, it is the surface area of the emitting material that determines the amount of its emission. Therefore, if these regions are distributed over a smaller area of the disk, they need to occupy a larger fraction of that area, which is what we find with our analysis. This argument justifies our choice of dealing with very simple structures for the optically thick regions: even if optically thick regions in real disks would likely have more complex structures than modelled here, our analysis is meaningful in terms of the fractional area covered by such regions throughout the disk.

As done in Section 4.6.2.1 for the case of a constant f within 300 AU, we analize here the dust mass which has to be present in the optically thick regions (Eq. 4.27). For the case of the ring between 10 and 20 AU the total dust mass in the optically thick regions is $M_{dust} \approx f \times 2.4 \cdot 10^{-4} M_\odot$, and rises to $\approx f \times 5.5 \cdot 10^{-4} M_\odot$, $\approx f \times 8.7 \cdot 10^{-4} M_\odot$ and $\approx f \times 1.3 \cdot 10^{-3} M_\odot$ when the ring is moved outward to $50-60$

optically regions inside a ring between 10 and 20 AU						
	$\gamma = 1$		$\gamma = 0.5$		$\gamma = 0$	
	$R_c = 20AU$	$R_c = 200AU$	$R_c = 20AU$	$R_c = 200AU$	$R_c = 20AU$	$R_c = 200AU$
$M_{dust}^{unpert} = 10^{-5} M_\odot$	100	520	70	1200	55	3200
$M_{dust}^{unpert} = 10^{-4} M_\odot$	10	52	7	120	5.5	320
$M_{dust}^{unpert} = 10^{-3} M_\odot$	1	5.2	0.7	12	0.55	32

optically regions inside a ring between 10 and 20 AU						
	$\gamma = 1$		$\gamma = 0.5$		$\gamma = 0$	
	$R_c = 20AU$	$R_c = 200AU$	$R_c = 20AU$	$R_c = 200AU$	$R_c = 20AU$	$R_c = 200AU$
$M_{dust}^{unpert} = 10^{-5} M_\odot$	630	1300	530	2000	680	3300
$M_{dust}^{unpert} = 10^{-4} M_\odot$	63	130	53	200	68	330
$M_{dust}^{unpert} = 10^{-3} M_\odot$	6.3	13	5.3	20	6.8	33

optically regions inside a ring between 10 and 20 AU						
	$\gamma = 1$		$\gamma = 0.5$		$\gamma = 0$	
	$R_c = 20AU$	$R_c = 200AU$	$R_c = 20AU$	$R_c = 200AU$	$R_c = 20AU$	$R_c = 200AU$
$M_{dust}^{unpert} = 10^{-5} M_\odot$	2700	2300	5700	2700	62000	3400
$M_{dust}^{unpert} = 10^{-4} M_\odot$	270	230	570	270	6200	340
$M_{dust}^{unpert} = 10^{-3} M_\odot$	27	23	57	27	620	34

optically regions inside a ring between 10 and 20 AU						
	$\gamma = 1$		$\gamma = 0.5$		$\gamma = 0$	
	$R_c = 20AU$	$R_c = 200AU$	$R_c = 20AU$	$R_c = 200AU$	$R_c = 20AU$	$R_c = 200AU$
$M_{dust}^{unpert} = 10^{-5} M_\odot$	19000	4100	370000	3800	$2.4 \cdot 10^9$	3700
$M_{dust}^{unpert} = 10^{-4} M_\odot$	1900	410	37000	380	$2.4 \cdot 10^8$	370
$M_{dust}^{unpert} = 10^{-3} M_\odot$	190	41	3700	38	$2.4 \cdot 10^7$	37

Table 4.2: Required dust overdensities in the added localized optically regions

AU and $80 - 90$ AU, respectively, because of the increased area of the ring itself. To explain the left end of the F_{1mm}-α_{1-3mm} diagram Fig.4.8 filling factors $f > 0.1$ on the top of the lowest mass disk ($M_{dust}^{unpert} = 10^{-5} M_\odot$) are needed. However, the mass in the optically thick regions is larger than the one in the unperturbed structure for all the rings considered here. This would require an extremely strong concentration of particles in those regions which are not seen in the results of the numerical simulations run so far (see discussion in 4.6.3). For the disk with $M_{dust}^{unpert} = 10^{-4} M_\odot$ a significant decrease of the spectral index α_{1-3mm} , i.e. down to about 2.5 and lower is obtained only for $f > 0.3$. These filling factors require dust masses in the optically thick regions as large as at least 70% of the unperturbed disk mass. Finally, the added optically thick regions in the most massive disk considered here, with $M_{dust}^{unpert} = 10^{-3} M_\odot$, contain relatively low dust mass as compared with the unperturbed disk mass. For example, in the case of $f = 0.5$ the ratio among the former and latter masses is about 12%, 28%, 44%, 65% for the optically thick regions inside rings with radii of $10 - 20$ AU, $30 - 40$ AU, $50 - 60$ AU and $80 - 90$ AU, respectively.

Tables 1-4 report, for models with different unperturbed disk structures in terms of total dust mass, γ and R_c , the required overdensities in the optically thick regions. These are defined as the ratio between the dust surface density Σ_{dust}^{f} in the optically

thick regions and the surface density in the unperturbed disk structure evaluated at the center of the ring. Since Σ^{f}_{dust} is always the same (i.e. $1/k_{3mm} \approx 2.2 cm^2/g$), the required overdensities depend only on the value that the dust surface density of the unperturbed disk assumes in the ring, and therefore on the (M^{unpert}_{dust}, γ, R_c) parameters which define such surface density. Note that the values of these overdensities do not depend on the adopted value for the dust opacity κ_{3mm} (or equivalently on the adopted dust model). This is because both the surface density in the optically thick regions, and the surface density in the optically thin unperturbed disk structure at a given flux depend on the dust opacity as κ^{-1}_{3mm}. The lowest values for the overdensities are found for the most massive disk when the overdensity region is located closest to the star. The low overdensity values of order of unity indicate that this disk is assive enough to have the unperturbed structure at radii of $\sim 10-20$ AU marginally optically thick by itself, i.e. without the addition of any artificial optically thick region.

4.6.3 Discussion

In this work we have discussed the possible effect of local optically thick regions in the integrated fluxes of young disks in the millimeter. Since the required overdensities needed to make these regions optically thick are typically very large one could expect these regions to be easily detectable with high-angular resolution imaging through (sub-)millimeter interferometry. However, the contrast between the surface brightnesses inside and outside the optically thick regions is not the only factor determining the possible observability of these structures. In fact, if the bright optically thick regions were uniformly distributed throughout the disk and with characteristic length scales much smaller than the angular resolution of the observations, they would be smeared out by the convolution with the resolution element.

Since all the high-angular resolution observations of disks conducted so far in the (sub-)mm have revealed a disk structure which is essentially homogeneous, the results of existent observations provide an upper limit to the characteristic length scales of the invoked optically thick regions. The highest angular resolutions achieved so far in the sub-mm are about 0.2-0.4 arcsec, corresponding to physical scales of $\sim 30-60$ AU at the distances of nearby star forming regions (Isella et al. 2010, Andrews et al. 2011, Guilloteau et al. 2011). This means that if optically thick regions were concentrated in those 20 AU-wide annuli, a radial bump in the surface brightness map could have been marginally detected, although not spatially resolved, by these observations.

In order to probe non-homogeneous structures at smaller scales higher angular resolution is needed. The Atacama Large Millimeter/Submillimeter Array (ALMA) will allow to do that down to scales of a few AU only. For example, ALMA can detect spiral density waves in nearby massive disks (Cossins et al. 2010). If non-homogeneous regions will be detected by future observations with very high angular resolution, a prediction of the models presented in this work is that the millimeter spectral index measured in the bright regions should be equal to the spectral index

of the Plank function in that region, which would be 2 in the case of Rayleigh-Jeans emission. To determine more precise predictions from these models would require further modelling of the disk structure with a proper treatment of the radiative transport in the optically thick regions.

To understand whether the overdense optically thick regions discussed in this paper are physically plausible in real protoplanetary disks, one has to compare the required filling factors and overdensities of regions with small < 0.1 mm-sized grains discussed in the last section with the outcome of the numerical simulations of different mechanisms leading to the concentration of solid particles (see a recent review by Chiang & Youdin 2010).

A promising mechanism to concentrate solid particles is through the development of streaming instabilities, in which the gas and solid components are mutually coupled by drag forces in a turbulent disk. Johansen & Youdin (2007) showed that overdensities of particles even larger than 1000 can be formed. Another possible mechanism which has been proposed to trap solids involves the presence of large anticyclonic vortices in the disk. These structures can be the result of baroclinic instability (Klahr & Bodenheimer 2003), the Rossby wave instability (Lovelace et al. 1999, Regaly et al. 2011), or magneto-rotational instability (Fromang et al. 2005). Long-lived axisymmetric pressure bumps have been obtained in simulations of magneto-rotational turbulent disks (Johansen et al. 2009). These pressure bumps have the potential of trapping solids which are marginally coupled to the gas, like mm-cm sized pebbles, but the obtained overdensities in gas are not large enough ($\lesssim 10-20\%$) to redistribute more gas-coupled small grains at the levels required for the optically thick regime. Finally, some concentration of dust particles can occur in disks undergoing gravitational instabilites. In these disks, the non-linear evolution of the instabilities lead to the formation of spiral waves with local overdensities in the gas component as high as about 100 (Rice et al. 2004, Boss 2010). Since sub-mm sized particles are well coupled to the gas, the same level of overdensity is expected for small grains as well. Considering that spiral waves are characterized by very extended structures, the results presented in this work show that the overdense regions in spiral waves can be optically thick even at mm-wavelengths and can even dominate the emission of a young disk at these wavelengths. This means that for gravitational unstable disks the measured low values of the mm-spectral index ($\alpha_{1-3mm} \lesssim 3.0$) can be potentially explained by the optically thick emission of small grains from overdense regions in spiral waves.

4.7 Testing the theory of grain growth and fragmentation by mm-observations of protoplanetary disks

Brinstiel, Ricci, Trotta, Dullemond, Natta, Testi, Dominik, Henning, Ormel, & Zsom 2010b A&A, 503, L5.

Observations at sub-millimeter and mm wavelengths will in the near future be able to resolve the radial dependence of the mm spectral slope in circumstellar disks with a resolution of around a few AU at the distance of the closest star-forming regions.

In this work we presents the comparison of mm-observations of disks around pre-main sequence stars in the Taurus-Auriga and Ophiuchus star-forming regions with predicted mm-SED based on a dust evolution model with the aim to constrain the grain growth and fragmentation processes. In order to predict mm-SED we coupled a coagulation/fragmentation and disk structure codes.

Our models can quite naturally reproduce the observed mm-slopes, but a simultaneous match to the observed range of flux levels can only be reached by a reduction of the dust mass by a factor of a few up to about 30 while keeping the gas mass of the disk the same. This dust reduction can either be caused by radial drift at a reduced rate or during an earlier evolutionary time (otherwise the predicted fluxes would become too low) or due to efficient conversion of dust into larger, unseen bodies.

4.7.1 Disk Model description

Both the coagulation/fragmentation and disk structure models, requires as input a set of parameters for the central star and the disk. Here we consider disks around a PMS stars with a mass of $0.5 M_{\odot}$, bolometric luminosity of $0.9 L_{\odot}$ and effective temperature of 4000 K, which are typical values for the sample of low-mass PMS star in [102, 103] Ricci et al. (2010a, 2010b) in Taurus, Ophiuchus star-forming regions.

As disk surface density distribution we adopt the similarity solution for a viscous evolution of thin accretion disk ([81] Lynden-Bell & Pringle 1974) written in the form

$$\Sigma_{dust}(R) = \Sigma_0 \left(\frac{R}{R_c}\right)^{-\gamma} exp\left[-\left(\frac{R}{R_c}\right)^{2-\gamma}\right] \tag{4.29}$$

with values of the Σ_0, γ and R_c parameters in the ranges observationally constrained by sub-arcsec angular resolution imaging of young protoplanetary disks in the sub-mm ([66] Isella et al. 2009, [6, 7] Andrews et al. 2009, 2010). The surface density gradient γ and the characteristic radius R_c are assumed to be $\gamma = 1$ and $R_c = 60$AU. We assume a constant dust-to-gas mass ratio of 0.01

We compute the dust opacity coefficient adopting the same dust model as [102] Ricci et al. (2010a) i.e. porous composite spherical grains made of astronomical

Parameters				
M_{disk} $[M_\odot]$	5×10^{-3}	$\mathbf{10^{-2}}$	5×10^{-2}	10^{-1}
α_t	$\mathbf{5 \times 10^{-4}}$	10^{-3}	5×10^{-3}	-
u_f [m/s]	1	**3**	10	-
f_{vac} [% vol.]	**10**	30	50	-
ξ	1.0	**1.5**	1.8	-

Table 4.3: Parameters of the model grid: M_{disk} is the total disk mass, α_t is the turbulence parameter, u_f is the critical collision velocity, f_{vac} is the grain volume fraction of vacuum, and ξ is the index of the distribution of fragments. The parameters of the fiducial model are highlighted in bold face.

silicates, carbonaceous material and water ice and vacuum. The ratio between the fractional abundance of each species comes from [106] Semenov et al. 2003, and model with three different porosities have been considered (see Table 4.3) To estimate the optical properties of such composite particles we use the Bruggeman effective medium theory ([27] Bruggeman 1935) to calculate an effective dielettric function ε_{eff} for a composite grain and then we use this function in the Mie Theory to derive the dust absorbtion efficiency $Q_{abs}(a, \nu)$. The Mie coefficients are calculate using the complex optical constant of individual components that are taken from ([118] Weingartner & Drain 2001) for astronomical silicates, from ([124] Zubko et al.1996) for carbonaceous material and from ([115] Warren 1984) for water ice.

Instead of using simple truncated parametric power-law distribution, in this work we used the coagulation/fragmentation model ([20] Birntiel et al. 2010a) to simulate the growth of dust particles. Particles grow through mutual collisions (induced by Brownian motion and by turbulence, see [93] Ormel & Cuzzi 2007) and subsequent sticking by van der Waals forces. We assume the dust particles to be spheres of internal density ρ_s and vary ρ_s to account for porosity effects.

In this work to derive steady-state grain distribution where grain growth and fragmentation effects balance each other. Because the relative velocities for particles typically increase with grain radius, we can relate the fragmentation velocity to a certain grain size

$$a_{max} \backsimeq \frac{2\Sigma_g}{\pi \alpha_t \rho_s} \frac{u_f^2}{c_s^2} \tag{4.30}$$

above which particles fragment. The distribution of fragments are assumed to follow a power-law number density distribution $n(m) \backsimeq m^{-\xi}$ with an upper end at m_f.

So, the shape of the steady-state grain size distributions is influenced mainly by the parameters α_t, u_f, Σ_g, c_s and ξ which consist the free-parameters of our investigation.

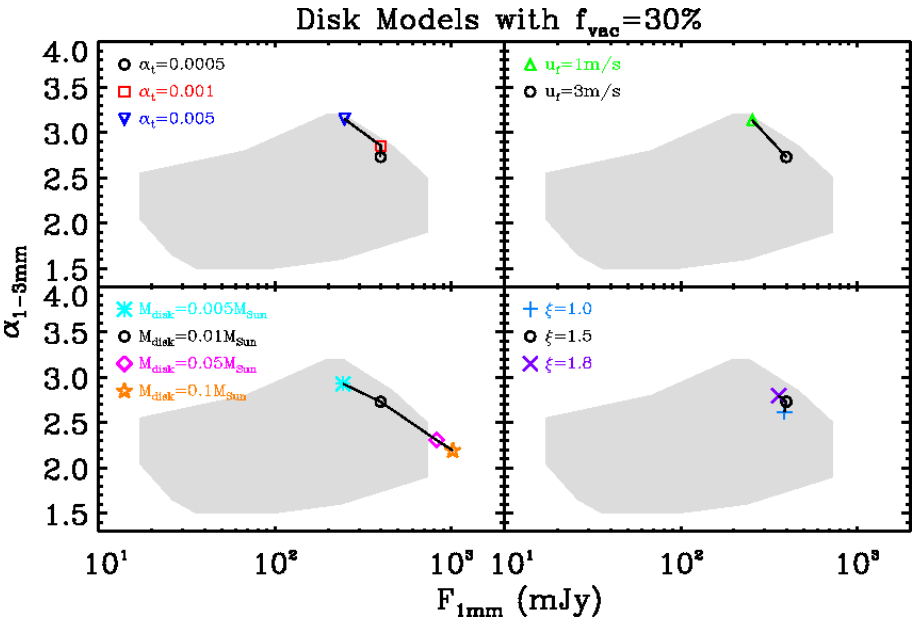

Figure 4.9: Influence of the parameters α_t (top left), fragmentation velocity (top right), disk mass (bottom left) and index ξ (bottom right) on the observed fluxes and spectral indices. The black circle denotes the fiducial model whose parameters are given in Table 4.3. The grey area represents the region in which the observed sources lie (see Fig. 6.2).

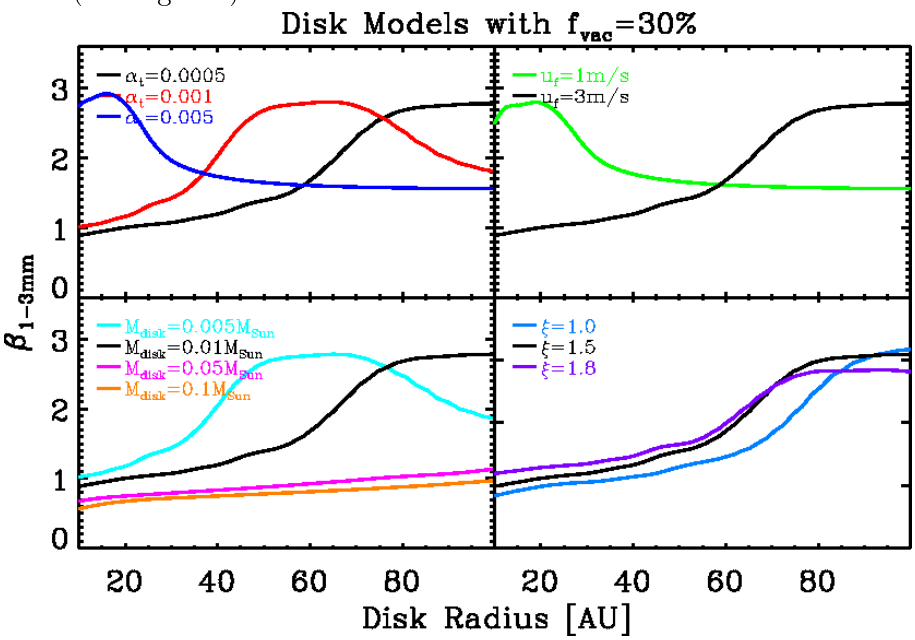

Figure 4.10: Predicted profiles of the dust opacity index at mm-wavelengths for different variations of the fiducial model. The colors correspond to the parameters shown in Fig. 4.11

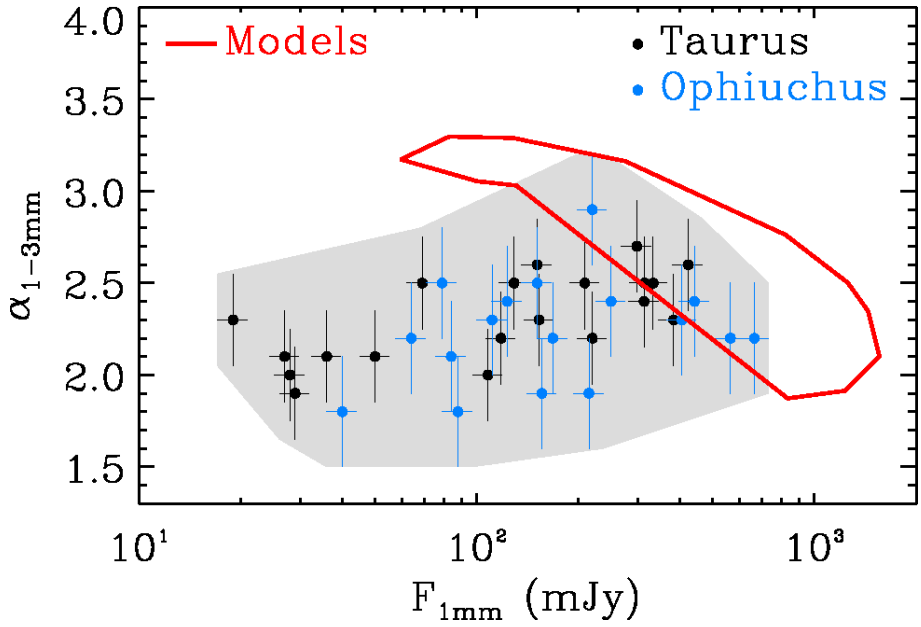

Figure 4.11: Observed fluxes at mm-wavelengths of the Taurus (black dots) and the Ophiuchus (blue dots) star-forming regions and the areas covered by the simulation results for all possible combinations of the parameters shown in Table 4.3

4.7.2 Results

In order to see the effect of the different quantities, characterizing the grain size distribution, we construct a grid of models (table 4.3) chosing with a range expected from theoretical (see. Johoansen & Klahr 2005; Dzyurkevich et al. 2010), observational ([6] Andrews et al. 2009) and experimental works (Güttler et al. 2010).

Figure 4.9 show the influence of the different parameters on the obseved flux and spectral indices

1. $\boldsymbol{\alpha_t}$ **effect** (*top left panel*): According to Eq. 4.30 the maximum grain size decrease if α_t increase. Depending on where a_{max} lies with respect to the opacity peak, α_{1-3mm} can increase or decrease with increasing α_t. For the α_t values used here, a_{max} is typically so large that increasing α_t predicts steeper spectral slopes.

2. $\boldsymbol{u_f}$ **effect** (*top right panel*): The maximum grain size is proportional to u_f^2, therefore an increase of u_f by a factor of about 3 significantly change α_{1-3mm} by increasing the grain size by about one order of magnitude. However many models with a fragmentation velocity of $10m/s$ never reach a steady state. It is therefore not possible to explain lower α_{1-3mm} values by a further increase of u_f alone.

3. $\boldsymbol{M_{disk}}$ **effect** (*bottom left panel*): The influence of M_{disk} on F_{1mm} and α_{1-3mm} is twofold. Firstly, a decrease in M_{disk} (assuming a constant dust-to-gas ratio

and a fixed shape of the disk surface density, i.e. not varying R_c and γ) reduces the amount of emitting dust and thus F_{1mm} . Secondly, such a reduction in gas mass also reduces a_{max} (Eq. 4.30), which tends to increase α_{1-3mm}. Hence, in order to explain faint sources with low α_{1-3mm}, the amount of emitting dust has to be reduced while the disk gas mass stays large. This effect could be achieved in two ways: the amount of dust could be reduced by radial drift at a reduced rate (full radial drift would quickly remove all mm-sized grains, see Brauer et al. 2007) or only the 'visible' amount of dust is reduced if some of the dust is already contained in larger bodies. This latter case is predicted by our non-steady-state distribution models and will be discussed in more detail in a forthcoming paper.

4. **ξ effect** (*bottom right panel*): In general, lower values of ξ translate to shallower grain-size distribution, which results in lower values of β_{1-3mm} (see Draine 2006). The figure does not seem to indicate a strong dependence on ξ, but lower values of ξ (around 1) seem to be closer to the observations especially at high fluxes.

Figure 4.10 show the predicted radial dependence of the dust opacity index β_{1-3mm}. It can be seen that the shape of most models looks similar, slightly increasing from β_{1-3mm}-values around 0.5 at 10 AU up to around 1.5 at 100 AU. The reason for this is that a_{max} depends on the ratio of surface density over temperature. Under typical assumptions, a_{max} will decrease with radius. An upper grain size, which is decreasing with radius and stays outside the peak in the opacity, results in β_{1-3mm} increasing with radius (cf. Fig. 3 in Ricci & al. 2010). If the radially decreasing upper grain size a_{max} reaches sizes just below mm, then the peak in opacity will produce also a peak in the radial profile of β_{1-3mm} (the size of which depends much on the assumed opacity), which can be seen in Fig. 4.10. Thus, even though a_{max} is monotone in radius, β_{1-3mm} does not need to be monotone.

4.7.3 Discussion and calculation

In this work we have present the first comparison of simulated grain size distributions and observed mm spectral indices of YSOs in the Taurus and the Ophiuchus star-forming regions. Additionally we present the first predictions of the radial profile of the dust opacity index at mm wavelength that are consistent with the limits set by Isella et al. (2010).

Low values of the observed mm-slopes are quite naturally reproduced by our models, favoring low values of ξ and α_t as well as fragmentation threshold velocities above $1 ms^{-1}$. However, a simultaneous match to the observed range of flux levels requires a reduction of the dust mass by a factor of a few up to about 30. This over-prediction of fluxes cannot be fixed by simply reducing the disk mass because the predicted α_{1-3mm} would be too large for smaller disk masses. Opacities induce a large uncertainty in the flux levels. However, considering the results of Draine (2006), it seems implausible that the large spread in observed fluxes for different

disks with similar α_{1-3mm} (which is probably even larger as very faint disks are not contained in the sample) can be explained by different grain mineralogy alone. The reduction of observable dust could be due to radial drift at a reduced rate or during an earlier epoch (drift has been artificially suppressed in this work in order to explain the low values of α_{1-3mm} by $\gtrsim 1mm$ sized grains). Another possible explanation is grain growth to even larger sizes, as these bodies have a small opacity coefficient per unit mass.

Finally, a different dependence between α_{1-3mm} and the observed flux F_{1mm} might also originate from disk surface densities profiles that differ from what we have assumed in this work.

4.8 Constraining variations of dust properties in circumstellar disks with high angular resolution observations at mm-wavelenghts

Trotta, Testi, Natta, Ricci (in preparation)

Grain growth in protoplanetary disks is the first step towards the formation of the rocky cores of planets. Models predict that grains grow, migrate and fragment in the disk and predict varying dust properties as a function of radius, disk age and physical properties. To constrain grain growth and migration in protoplanetary disks high-angular resolution observations at more then one (sub-)mm wavelength are currently being performed to detect possible radial variations of the dust properties ([67] Isella et al. 2010, [14] Banzatti et al. 2011, [55] Guilloteau et al 2011).

In this work we present results of fitting spatially resolved multi-frequency observations at mm-wavelenghts of the disk around CQ Tau with the two-layer disk model that include the possibility different grain size distribution as a function of radius.

We have obtained a clear evidence of a radial dependence of the grain size distribution in this disk. In particular our model predict a grain size distribution with a maximum size decreasing with radius. These results moreover, are in agreement with recent dust evolution model prediction by [20] Birnstiel et al 2010a.

4.8.1 Disk Model description

In order to derive di disk structure we adopted the 2-layer disk model of [30] Chiang & Goldreich (1997) with the modifications of [38] Dullemond, Dominik & Natta (2001). The model requires as input a set of parameters for the central star and the disk. The stellar properties of CQTau are assumed known as in [112] Testi et al. (2003) ($T_{eff} = 6900K$, $L_\star = 6.6L_\odot$, $M_\star = 1.5M_\odot$ and $d = 100$pc). As disk surface density distribution we adopt the similarity solution for a viscous evolution of thin accretion disk ([81] Lynden-Bell & Pringle 1974) written in this form

$$\Sigma(R,t) = \Sigma_{tr}\left(\frac{R_{tr}}{R}\right)^{\gamma} e^{-\frac{1}{2(2-\gamma)}\left[\left(\frac{R}{R_{tr}}\right)^{(2-\gamma)}-1\right]} \tag{4.31}$$

where Σ_{tr} is the surface density at transition radius R_{tr} and γ is the slope of the assumed power-low viscosity (see Appendix B for a brief review).

We compute the dust opacity coefficient adopting the same dust model as [14] Banzatti et al. 2011 i.e. porous composite spherical grains made of (vol. perc.) 7% astronomical silicates, 21% carbonaceous material and 42% water ice and 30% vacuum To estimate the optical properties of such composite particles we use the Bruggeman effective medium theory ([27] Bruggeman 1935) to calculate an effective dielettric function ε_{eff} for a composite grain and then we use this function in the Mie Theory to derive the dust absorbtion efficiency $Q_{abs}(a,\nu)$. The Mie coefficients

are calculate using the complex optical constant of individual components that are taken from ([118] Weingartner & Drain 2001) for astronomical silicates, from ([124] Zubko et al.1996) for carbonaceous material and from ([115] Warren 1984) for water ice. We adopt a power-law grain size distribution with slope q

$$n(a) \propto a^{-q} \tag{4.32}$$

truncated between the minimum and maximum grain sizes a_{min} and a_{max}, respectively. The value of a_{min} is set to $5nm$ according to the typical value observed for unprocessed dust in the ISM and for the power law exponent we have used $q = 3$ as proposed in previous studies and theoretical expectation ([37] Draine 2006). Since in this work we want to investigate the radial dependence of the dust properties in the disk around CQ Tau, we have included in our model the possibility to have a radial variation of the grain size distribution adopting for the maximum size, a power low profile

$$a_{max}(R) = a_{0max} \left(\frac{R}{R_0} \right)^{b_{max}} \tag{4.33}$$

where a_{0max} is the maximum grain size value at the reference position $R_0 = 40AU$ and b_{max} is the power-law exponent.

4.8.2 Model fitting

In order to avoid the nonlinear effects introduced by the deconvolution process (which can increases the noise level, specially in the case of weak extended source like circumstellar disk) models and observations are compared in the Fourier space. We analyze therefore the observed disk emission comparing the measured complex visibilities with a theoretical predictions of our 2-Layer disk model. To define how well the model fits the data, we adopt the χ^2 parameter:

$$\chi^2 = \sum_j \left[[Re_j(obs) - Re_j(mod)]^2 + [Im_j(obs) - Im_j(mod)]^2 \right] \cdot w_j \tag{4.34}$$

where Re and Im are the real and imaginary part of the j-th observed (obs) or model predicted (mod) visibility and w is the weight of each data point in the uv-plane [2]. The five free parameters adopted in our fit procedure are: γ, R_{tr}, Σ_{tr} of the surface density distribution (Eq. 4.31) and b_{max}, a_{0max} of the maximum grain size distribution (Eq. 4.33).

The disk inclination, position angle are assumed known as in [14] Banzatti et al. (2011). Each free parameter is allowed to vary in a large range: $[-1 : +1]$ for γ, $[15 : 40]$ for R_{tr}, $[0.2 : 1.2]$ for Σ_{tr}, $[-2.5 : +1.5]$ for b_{max}, $[0.2 : +5.0]$ for a_{0max}.
For each wavelenght λ_i (0.87mm, 1.3mm, 2.7mm, 7mm), we compute the $\chi^2_{\lambda_i}$ value, corrisponding to a given set of free parameter, follow this sequence of step:

- We produce a model image of a given set of free parameters

[2] The u and v coordinates, the corrisponding visibility and the weight are provided in the observed uv-table

γ	Σ_{tr}	R_{tr}	a_{max}	b_{max}
0.5	0.9	20.0	0.8	-1.8

Table 4.4: For each parameter we report the best fit value and the values of the 1σ confidence level intervals.

- We Fourier-Trasform the predicted disk image and sample the resulting visibility function at the appropriate positions on the (u,v) plane corrisponding to the observed samples.
- We compute the $\chi^2_{\lambda_i}$ value.

This procedure was repeated on the adopted grid of model parameters to contruct a $\chi^2_{\lambda_i}$ hypercube for each wavelenght. In order to find the best fitting model, we construct a new hypercube χ^2_{sum} given by the sum of the all $\chi^2_{\lambda_i}$ hypercube and we search the minimum of the χ^2_{sum} as a function of all parameters.

4.8.2.1 Results

The best fit values and the confidence range for the model parameters are listed in table 4.4. In Fig. 4.12 we show the projections of the χ^2_{sum} hypercube on each coordinate (first line) and on different planes.

The resulting maximum grain size distribution with $b_{max} = -1.8$ and $a_{0max} = 0.8$ clearly evidence the radial dependence of the grain size distribution in the disk around CQ Tau. This impliy the inner disk is populated by dust grains of more the 10 cm while the outer disk is characterized by small grain

These results moreover, are in agreement with recent dust evolution model prediction by [20] Birnstiel et al 2010a.

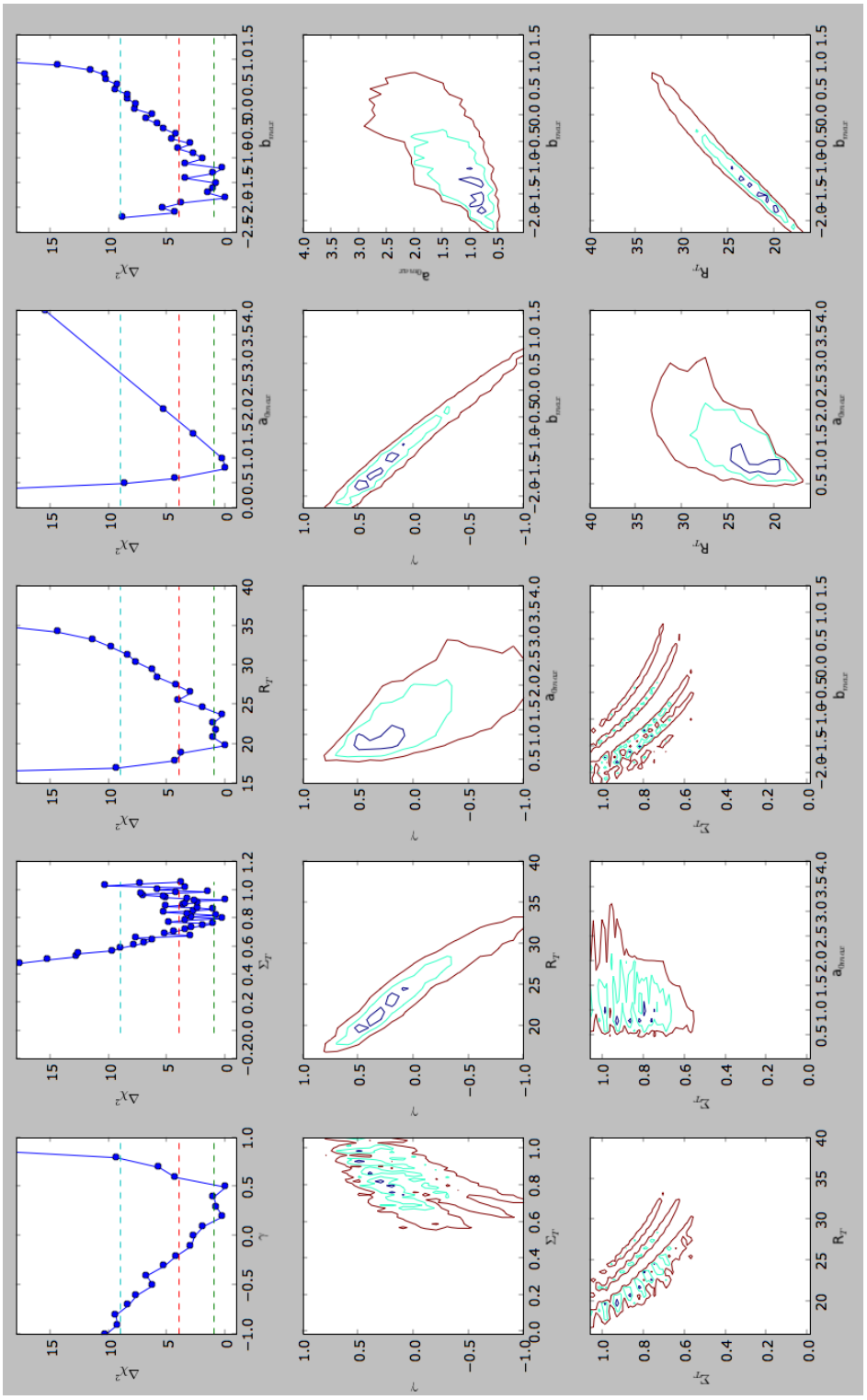

Figure 4.12: χ^2_{sum} hypercube projections on each coordinate (first line) and on different planes. To produce each plot we have chosen the value of the other parameters corresponding to the minimum of χ^2_{sum} at each position on the planes shown.

Chapter 5

Conclusions and Future Prospettive

In this thesis we have studied the structure and the emission properties at (sub-)mm wavelenghts of circumstellar disk around pre-main sequence stars. In particular, the main purpose was to investigated how the spatial variation of the dust opacity can influence the disk thermal and geometrical structure and so affect its emission properties. In order to reach this aim, we have constructed a circumstellar disk structure model which include the possibility to take into account (in parametric way) possible spatial variation of the grain size distribution and dust-to-gas ratio. Moreover we have investigated if, a possible radial variation of a dust grain size distribution can be constrained comparing our two layer disk model, against spatially resolved multi-frequency observations at mm-wavelenghts

In Chap. 3 we have presented a new developed code which allow a self consistent computation of the structure of a steady passive thin disk in vertical hydrostatic equilibrium under the single annulus approximation (the so called 1+1Disk model). In order to compute a self-consistent thermal and geometrical disk structure the model numerically solve the hydrostatic equilibrium equation coupled to the radiative transfer equation in vertical direction. In particular the RT problem is solved with the Variable Eddington Factors (VEF) method which is been proved by [39] Dullemond et al. (2002) to be a fast and efficient method to find the solution of the radiative trasfer equation in circumstellar disk. In order to investigate the spatial variation of the dust opacity, the model include the possibility to have for each single radius and height in the disk a population of dust grains that can be different in terms of maximum grain size and dust-to-gas ratio. Using different (parametric) Rz-distribution for maximum grain size and dust-to-gas ratio the model predict change in the disk structure and dust continuum emission and so can be used to investigate the spatial variation of the dust property and try to constrain the grain growth and settling processes.

In Chap. 4 we have presented a more semplified circumstellar disk model which allow, as the 1+1D model, a self consistent computation of the disk structure. This model solve the radiative transfer problem in simple way adopting the so called '*two layers*' approximation first proposed by [30] Chiang & Goldreich 1997. Using the capability of our two-layer model to have a radial variation of the dust properties, in particular, the possibility to modify the radial profile of the grain size distribution, we have used it to interpret observations at sub-millimiter and mm wavelenghts of disk around pre-main sequence stars.

In Ricci, Trotta, & al. 2011 (submitted) we investigate the effect of possible local optical thick regions on the mm-wave emission of protoplanetary disks. We find that optically thick regions characterized by relatively small filling factors can reproduce the mm-data of young disks without requesting emission from mm/cm-sized pebbles. However, these optically thick regions require dust overdensities much larger than what predicted by any of the physical processes proposed in the literature to drive the concentration of solids. The results of this analysis further strengthen the scenario for which the measured low spectral indices of protoplanetary disks at mm wavelengths are due to the presence of large mm/cm-sized pebbles in the disk outer regions.

In [21] Brinstiel, Ricci, Trotta, & al. 2010 we have presented the comparison of mm-observations of disks around pre-main sequence stars in the Taurus-Auriga and Ophiuchus star-forming regions with predicted mm-SED based on a dust evolution model with the aim to constrain the grain growth and fragmentation processes. In order to predict mm-SED we coupled a coagulation/fragmentation and disk structure codes. Our models can quite naturally reproduce the observed mm-slopes, but a simultaneous match to the observed range of flux levels can only be reached by a reduction of the dust mass by a factor of a few up to about 30 while keeping the gas mass of the disk the same.

Given to fast computation time of the 2-layer model to solve the disk structure and its possibility to take into account possible radial variation of the grain size distribution, we have use it to fit spatially resolved multi-frequency observations at mm-wavelenghts of the disk around CQ Tau. We have obtained a clear evidence of a radial dependence of the grain size distribution in this disk. In particular our model predict a grain size distribution with a maximum size decreasing with radius. These results are, moreover, in agreement with recent dust evolution model prediction by [20] Birnstiel et al 2010a.

The two circumstellar disk models developped in this thesis are based on the approximate 2-layer and 1+1D irradiation-angle description. In reality the structure of these disk is 2-D, if axisymmetry can be assumed, and 3D if it cannot. Over the last 10 years many multidimensional dust constinuum radiative transfer programs and algorithms were developed for this purpose (Sec. 2.3.1). The main improvements of 2D/3D models over 1+1D models is their ability to account for radial radiative energy diffusion in the disk, for cooling of the outer disk in radial direction, for the complex 3D structure of the dust inner rim and in general for more realistic model images. Therefore, an extension of our $1+1D$ circumstellar disk model to a full 2D model can be fondamental for a more precise prediction of dust emission propriety.

Appendix A

Theory of radiation-matter interaction

In this Appendix we give a brief introduction of the theory we use to estimate the optical properties of the dust grain in our disk model. We present in (A.1) the main steps to derive the absorbtion and scattering efficiencies with the *Mie theory* in the simplest case of homogeneous spherical grains (for more detail see [23]). A similar approach can be used for other idealized grain geometry like infinite circular cylinders grains, or spheroidal grains. In (A.2) we give a brief overview of the *effective-medium theories* used to describe the optical properties of inhomogeneous dust grains.

A.1 Mie theory for a sphere

Scattering and absorbtion of light by spherical grains is a problem of classical electrodynamic. The formal solution of this problem was derived by Mie in 1908 and is known as *Mie theory* or *Mie solution*. In the Mie theory, one finds the scattered electromagnetic field and the field inside the particle by expanding both into an infinite series of indipendent solutions to the wave equation; the series coefficients are determinated from the boundary conditions on the particle surface. Let's see the main steps to derive the absorbtion and scattering efficiencies.
Consider a spherical particle in vacuum illuminated by a linearly polarized monocromatic plane wave of frequency $\nu = \omega/2\pi$. Let $\mathbf{E}_i$ and $\mathbf{H}_i$ descibe the incident electric and magnetic field. We denote the field within the particle by $\mathbf{E}_1$,$\mathbf{H}_1$ and outside of it by $\mathbf{E}_2$, $\mathbf{H}_2$. The field outside is the superposition of the incident and the scattered field

$$\mathbf{E}_2 = \mathbf{E}_i + \mathbf{E}_s \tag{A.1}$$
$$\mathbf{H}_2 = \mathbf{H}_i + \mathbf{H}_s \tag{A.2}$$

The further calculation are greatly simplified by the folloing relations. Let $\mathbf{c}$ be an arbitrary constant vector and ψ a solution to the *scalar wave equation*

$$\Delta\psi + k^2\psi = 0 \tag{A.3}$$

where $k = \sqrt{\frac{\omega^2\mu\varepsilon}{c^2}}$ is the wavenumber, μ is the magnetic permeability and ε is the dielectric permeability. So k take into account all material properties. Then the

vector function $\mathbf{M}$, defined by

$$\mathbf{M} = rot(\mathbf{c}\psi) \tag{A.4}$$

is divergence-free ($div\mathbf{M} = 0$) and a solution to the *vector equation*

$$\Delta\mathbf{M} + k^2\mathbf{M} = 0 \tag{A.5}$$

This is easy to prove either by the standard formulae of vector analysis or component-wise. The vector function $\mathbf{N}$ given by

$$\mathbf{N} = \frac{1}{k} rot\ \mathbf{M} \tag{A.6}$$

also obey the wave equation

$$\Delta\mathbf{N} + k^2\mathbf{N} = 0 \tag{A.7}$$

Step 1 In the first step one solve the scalar wave equation with separation of variables method. In spherical polar coordinates (r, θ, ϕ), the (A.3) can be written

$$\frac{1}{r^2}\frac{\partial}{\partial r}\left(r^2\frac{\partial\psi}{\partial r}\right) + \frac{1}{r^2 sin\ \theta}\frac{\partial}{\partial\theta}\left(sin\ \theta\frac{\partial\psi}{\partial\theta}\right) + \frac{1}{r^2 sin^2\theta}\frac{\partial^2\psi}{\partial\phi^2} + k^2\psi = 0 \tag{A.8}$$

We make an ansatz of separated variables $\psi(r, \theta, \phi) = R(r) \cdot T(\theta) \cdot P(\phi)$. This lead to the three equations:

$$\frac{d^2P}{d\phi^2} + m^2P = 0 \tag{A.9}$$

$$\frac{1}{sin\ \theta}\frac{d}{d\theta}\left(\sin\theta\frac{dT}{d\theta}\right) + \left[n(n+1) - \frac{m^2}{sin^2\theta}\right]T = 0 \tag{A.10}$$

$$\frac{d}{dr}\left(r^2\frac{dR}{dr}\right) + [k^2r - n(n+1)]R = 0 \tag{A.11}$$

The linearly indipendent solution to (A.9) are $sin\ (m\phi)$ and $cos\ (m\phi)$. Becouse they must be single-value ($P(\phi) = P(\phi + 2\pi)$) it follow that $m = 0, \pm1, \pm2, ...$ Equation (A.10) is satisfied by the Legendre functions of the first kind $P_n^m(cos\ \theta)$, where n and m are integer and $m \in [-n, n]$. The equation (A.11) has, as solution, the spherical Bessel functions of the first ($j_n = \sqrt{\pi/2\rho}J_{n+\frac{1}{2}}(\rho)$) and second ($y_n = \sqrt{\pi/2\rho}Y_{n+\frac{1}{2}}(\rho)$) kind where $\rho = kr$ and $n + \frac{1}{2}$ is half-integer. Altoghether the solution can be written

$$\psi_{emn} = cos\ (m\phi) \cdot P_n^m(cos\ \theta) \cdot z_n(kr) \tag{A.12}$$

$$\psi_{omn} = sin\ (m\phi) \cdot P_n^m(cos\ \theta) \cdot z_n(kr) \tag{A.13}$$

Here z_n may either equal j_n or y_n. In the subindices of ψ, 'e' stands for even (associated with cosine terms) and 'o' for odd (sine terms). As ψ is the generating function for $\mathbf{M}$, we get, from (A.4)

$$\mathbf{M}_{emn} = rot(\mathbf{r}\psi_{emn}) \tag{A.14}$$

$$\mathbf{M}_{omn} = rot(\mathbf{r}\psi_{omn}) \tag{A.15}$$

$\mathbf{N}_{emn}$ and $\mathbf{N}_{omn}$ then follow from (A.6)

Step 2. In the next step, one expands the incident, internal and scattered waves into the spherical harmonics $\mathbf{M}_{emn}$, $\mathbf{M}_{omn}$, $\mathbf{N}_{emn}$ and $\mathbf{N}_{omn}$. One obtain, for the internal and scattered field:

$$\mathbf{E}_i = \sum_{n=1}^{\infty} E_n \left(c_n \mathbf{M}_{o1n}^{(1)} - i d_n \mathbf{N}_{e1n}^{(1)} \right) \tag{A.16}$$

$$\mathbf{E}_s = \sum_{n=1}^{\infty} E_n \left(a_n \mathbf{N}_{e1n}^{(3)} - b_n \mathbf{M}_{o1n}^{(3)} \right) \tag{A.17}$$

where $E_n = E_0 i^n \frac{2n+1}{n(n+1)}$, the scalar E_0 denotes the amplitude of the incident wave. The superscript (1) signifies that the radial dependence of the generating function ψ is given by j_n and not by y_n and the superscript (3) denotes that the dipendence of the generating function is given by the spherical Hankel function $h_n(z) = j_n(z) + i y_n(z)$ of order n. The magnetic fields $\mathbf{H}_i$, $\mathbf{H}_s$ follow from the corresponding electric fields by applying the curl after Maxwell's equation.

Step 3 Then, one compute the expansion coefficients in (A.16) and (A.17) from the boundary conditions of the electromagnetic field at the surface of the grain. This lead to four linear equation for the expansion coefficients a_n, b_n, c_n and d_n of the internal and scattered field. If λ is the wavelength of the incident radiation, m the complex optical constant of the sphere, a its radius and $x = 2\pi a/\lambda$ the size parameter, then a_n and b_n are given by

$$a_n = \frac{\psi_n(x) \cdot \psi_n'(mx) - m\psi_n(mx) \cdot \psi_n'(x)}{\zeta_n(x) \cdot \psi_n'(mx) - m\psi_n(mx) \cdot \zeta_n'(x)} \tag{A.18}$$

$$b_n = \frac{m\psi_n(x) \cdot \psi_n'(x) - \psi_n(mx) \cdot \psi_n'(x)}{m\zeta_n(x) \cdot \psi_n'(mx) - \psi_n(mx) \cdot \zeta_n'(x)} \tag{A.19}$$

The complex functions

$$\psi_n(z) = z j_n(z) \tag{A.20}$$

$$\psi_n'(z) = z j_{n-1}(z) - n j_n(z) \tag{A.21}$$

$$\zeta_n(z) = z[j_n(z) + i y_n(z)] = z h_n^{(1)}(z) \tag{A.22}$$

$$\zeta_n'(z) = z[j_{n-1}(z) + i y_{n-1}(z)] - n[j_n(z) + i y_n(z)] \tag{A.23}$$

may be calculated from the recurrence relations (Abr70)

$$j_n(z) = -j_{n-2}(z) + \frac{2n-1}{z} j_{n-1}(z) \tag{A.24}$$

$$y_n'(z) = -y_{n-2}(z) + \frac{2n-1}{z} y_{n-1}(z) \tag{A.25}$$

starting with $j_0(z) = sin\ z/z$, $j_1(z) = sin\ z/z^2 - cos\ z/z$, $y_0(z) = -cos\ z/z$, $y_1(z) = -cos\ z/z^2 - sin\ z/z$.

Step 4 One computed the scattered and absorbed power.

...

...

Step 5 We compute the absorbtion and scattering efficiencies.
According the definition in xx, W_a is related to the absorbtion coefficient of the particle, C_{abs} through $W_{abs} = S_i C_{abs}$. replacing the fields $\mathbf{E}_i$ and $\mathbf{E}_s$ in the xx, one obtain, after some algebra, the following formulae for the efficiencies of extintion and scattering:

$$Q_{ext} = \frac{2}{x^2}\sum_{n=1}^{\infty}(2n+1)\left[|a_n|^2 + |b_n|^2\right] \tag{A.26}$$

$$Q_{sca} = \frac{2}{x^2}\sum_{n=1}^{\infty}(2n+1)Re\left\{a_n + b_n\right\} \tag{A.27}$$

where the expansion coefficients a_n,b_n are given in xx. The asymmetry factor becomes:

$$g = \frac{4}{x^2 Q_{sca}}\sum_{n=1}^{\infty}\left[\frac{n(n+2)}{n+1}Re\left\{a_n^* a_{n+1} + b_n^* b_{n+1}\right\} + \frac{2n+1}{n(n+1)}Re\left\{a_n^* b_n\right\}\right] \tag{A.28}$$

We troncate all the infinite series after $n_{max} = x + 4x^{1/3} + 2$ with $x = a2\pi/\lambda$ as sugest by Bohren and Huffman (1983).

A.2 Effective-medium theory

The description of the optical properties of inhomogeneous dust grain is an important task in many astrophysical problems. An approach widely used for this purpose is the application of *effective-medium theories*(EMTs). The basic idea of the EMTs is to derive an effective dielectric function ε_{eff} for a system of subgrain consisting of different materials and therefore with different electromagnetic properties. A homogeneous grain with this dielectric function shall show the same characteristics in absorbtion and scattering as the original inhomogeneous particle.

The basic condition is that the effective dielectric function ε_{eff} searched for, has to fulfil the condition

$$\langle \mathbf{D} \rangle = \varepsilon_{eff} \langle \mathbf{E} \rangle \tag{A.29}$$

where the angular brackets stand for a volume averaging over the entire grain volume V

$$\langle \mathbf{E} \rangle = \frac{1}{V}\int \mathbf{E}(\mathbf{x})dV \qquad \langle \mathbf{D} \rangle = \frac{1}{V}\int \varepsilon(\mathbf{x})\mathbf{E}(\mathbf{x})dV \tag{A.30}$$

If we consider the grain consisting of a finite number of homogeneous components each with its own dielectric function ε_j and volume feaction f_j, we can write

$$\langle \mathbf{E} \rangle = \sum_j f_j \mathbf{E}_j \qquad \langle \mathbf{D} \rangle = \sum_j f_j \varepsilon_j \mathbf{E}_j \tag{A.31}$$

where $\mathbf{E}_j$ are averanges themselves over the subvolume $f_j V$ (we have dropped the brakets). The relation (A.29) is thus replaced by

$$\sum_j \varepsilon_j f_j \mathbf{E}_j = \varepsilon_{eff} \sum_j f_j \mathbf{E}_j \tag{A.32}$$

We envisage the components to be present in the form of many identical subparticles that are much smaller then the wavelength. When such a subparticle is placed into an extended medium with a spatially constant but time-variable field $\mathbf{E}^{'}$, there is a linear relation between the field in the subparticle and the field in the outer medium ε_{eff}

$$\mathbf{E}_j = \beta \mathbf{E}^{'} \tag{A.33}$$

When one assumes that such a large-scale average fiel $\mathbf{E}^{'}$ in the grain exists, one can remove the local fields $\mathbf{E}_j$ and find the effective dielectric function ε_{eff}.

Two different approach can be used in the effective-medium theory. The first is '*Maxwell-Garnett approach*' assumes that the inhomogeneous material consists of an embedding matrix material (subscript m) which contains separated inclusions of other materials in low concentration (subscript i) with the sum of the volume fraction is unit ($f_m + \sum_i f_i = 1$). For the constant large-scale field $\mathbf{E}^{'}$ in (A.33), we take the field in the matrix m and obtain

$$\sum f_i \beta_i \varepsilon_i + f_m \varepsilon_m = \varepsilon_{eff} \sum f_i \beta_i + \varepsilon_{eff} f_m \tag{A.34}$$

which give us the *Maxwell-Garnett rule*:

$$\varepsilon_{eff} = \frac{f_m \varepsilon_m + \sum f_i \beta_i \varepsilon_i}{f_m + \sum f_i \beta_i} \tag{A.35}$$

The second is the '*Bruggeman approach*' supposes that none of the different materials is dominant in the mixture, like the matrix in the Maxwell-Garnett approach. Then the components distinguish themselves only through their permeability and volume fraction and no assumption is made about the averange field $\mathbf{E}'$. Inserting (A.33) in (A.32) yields the *Bruggeman rule*:

$$0 = \sum_j (\varepsilon_j - \varepsilon_{eff}) f_j \beta_j \tag{A.36}$$

with $\sum_j f_j = 1$. If the components consist of spherical entities

$$0 = \sum_j f_j \frac{\varepsilon_j - \varepsilon_{eff}}{\varepsilon_j + 2\varepsilon_{eff}} \tag{A.37}$$

Thus for n components, ε_{eff} is determined from a complex polynomial of n-th degree. This is the eqution that we solve to estimate the optical properties in our disk model.

Appendix B

Angular momentum conservation equation for a thin accretion disk

The key equation describing the gas evolution of an accretion disk is the *angular momentum conservation equation*. In this Appendix we examine the properties of a simple viscous thin disk model where the only angular momentum transport is provided by viscous stresses. In Sec. B.1 we derive the angular momentum conservation equation for a thin disk underlining the important role of the viscosity. In Sec.B.2 we show a simple class of solution that can be obtained when the viscosity function is time-indipendent and has a power-law dependence on radius $\nu \propto R^{\gamma}$.

B.1 The Diffusion equation for the disk surface density

As we have see in Sec. 3.3.2, unter the assumption of an axisymmetric disk, the pressure and gravitational forces do not give any contribution in the azimutal component of the Navier-Stokes equation (Eq. 3.23). Let us then write the Eq. 3.23 in vertically integrated form:

$$\Sigma\left(\frac{\partial u_\phi}{\partial t}+\frac{u_R u_\phi}{R}+u_R\frac{\partial u_\phi}{\partial R}\right)=\frac{1}{R^2}\frac{\partial}{\partial R}\left(R^2 T_{R\phi}\right) \tag{B.1}$$

where $T_{R\phi}$ is the vertical integral of the relevant component of the stress tensor and the last two terms on the left-hand side are obtained from writing the differential operators in cylindrical coordinates (Eq. 3.26). Multipling the above equation by R and using the continuity equation (3.21), we can write (B.1) as

$$\frac{\partial l}{\partial t}+\frac{1}{R}\frac{\partial}{\partial R}\left(R u_R l\right)=\frac{1}{R}\frac{\partial}{\partial R}\left(R^2 T_{R\phi}\right) \tag{B.2}$$

where $l=\Sigma R u_\phi$ is the angular momentum (per unit mass). The physical interpretation of the above expression is readily apparent. The left-hand side is the Lagrangian derivative of the angular momentum and the right-hand side is the torque exerted by viscous forces.

In the case of a thin disk, we have seen in Sec. 3.3.2 that the rotation curve is keplerian (Eq.3.29) and the stress tensor can be simply approximate by the classical shear viscosity (Eq.3.28) which vertically integrated can be written as

$$T_{R\phi}=\nu\Sigma R\frac{d\Omega}{dR}$$

Under these approximations and with the help of the continuity equation (3.21), we can obtain the radial velocity

$$u_R = -\frac{3}{\Sigma R^{1/2}} \frac{\partial}{\partial R}(\nu \Sigma R^{1/2}) \tag{B.3}$$

which can be inserted back in the continuity equation (3.21) to finally give

$$\frac{\partial \Sigma_g}{\partial t} = \frac{3}{R} \frac{\partial}{\partial R} \left[R^{1/2} \frac{\partial}{\partial R} \left(\nu \Sigma_g R^{1/2} \right) \right] \tag{B.4}$$

This equation is one of the key equations in the thin accretion disk theory. This is a *non linear diffusion equation* for the surface density whose temporal evolution is determined only by the viscosity ν. This clearly show the important role of the viscosity in the accretion disk theory, since it ultimately is the quantity that determines the evolution of the disk density

B.2 Self similar Solution

To solve the diffusion equation for the surface density (B.4), we need to specify how the viscosity law is done. Although one can not obtain the general solution of this equation, it's well know that exist a series of analytic solutions (steady state and time-dependent solution) that can be obtained assuming some particular function for the viscosity ν. These solutions can be obtained either in linear case ($\nu = \nu(R)$) in which case the Green function can be obtained analytically ([80] Lüst 1952; [81] Lynden-Bell & Pringle 1974) or in non-linear case ($\nu = \nu(R, \Sigma)$) in which case similarity methods can be used to obtained an exact special solution of the equation ([100] Pringle 1974; [78] Lin & Bodenheimer 1982; [79] Lin & Pringle 1987; [82] Lyubarskii & Shakura 1987).

In this thesis we have used a (Lynden-Bell & Pringle 1974) time-dependent self-similar solution of (B.4) obtained in the linear case unter the assumption that the viscosity law is time-indipendet and has a power law dependence on radius

$$\nu \prec R^{\gamma} \tag{B.5}$$

In this case a self similar solution of ($B.4$) can be written

$$\Sigma(\tilde{R}, \tilde{t}) = \frac{C}{3\pi\nu_1 \tilde{R}^{\gamma}} \tilde{t}^{\left[-\frac{(5/2-\gamma)}{(2-\gamma)}\right]} e^{\left[-\frac{\tilde{R}^{(2-\gamma)}}{\tilde{t}}\right]} \tag{B.6}$$

where C is a normalization constant, $\tilde{R} = R/R_1$ is the disk radius in units of radial scale factor R_1, $\nu_1 = \nu_1(R_1)$ is the disk viscosity at radius R_1, γ is the slope of the disk viscosity, $\tilde{t}$ is the non-dimensional time, $\tilde{t} = t/t_s + 1$, t is the age of the disk, and t_s is the viscous scaling time at the radius R_1 defined by:

$$t_s = \frac{1}{3(2-\gamma)^2} \frac{R_1^2}{\nu_1} \tag{B.7}$$

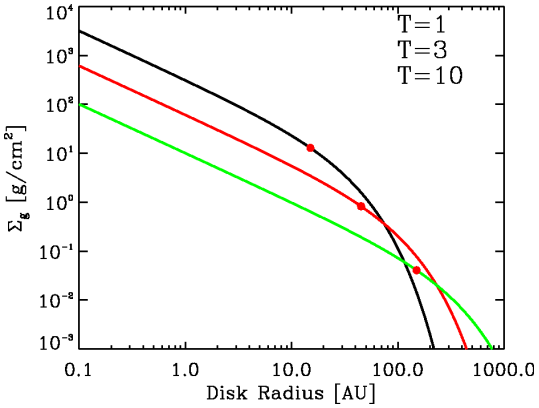

$\tilde{t}$	R_{tr}	Σ_{tr}	M_{disk}
1	15.0	12.871	0.0068
3	45.0	0.8257	0.0039
10	150.0	0.0407	0.0021

Figure B.1: Evolution of the surface density according to Eq. (B.6) for $\gamma = 1$, $R_1 = 30AU$, $\nu_1 = 10^{15}$ and $C = 10^{17}$. The three lines show, from top to bottom, the self-similar solution at increasingly large times ($\tilde{t} = 1, 3, 10$, respectively). The red points correspond to the surface density at the transitional radius R_{tr}.

The evolution of surface density for the case $\gamma = 1$ is showen in figure B.1. How we can see this form of the surface density has the characteristic of falling off exponentially at large disk radii. Over time, the disk mass decreases while the characteristic scale of the disk (initailly R_1) expands to conserve angular momentum. This solution is quite useful both for studying evolving disks analytically, and for comparing observations of disk masses, accretion rates or radii with theory ([56] Hartmann et al. 1998).

The surface density as expressed by Eq. B.6 includes a significant number of unknown quantitaties, C, ν_1, γ, t_s and R_1. As showed in ([67] Isella, Carpent, Sargent 2010) is more suittable for model fitting rewrite the (B.6) in function of the '*transition radius*' (i.e. radius at which the mass flow $\dot{M}(R,t)$ changes sign). Since disk evolution is governed by the conservation of the total angular momentum, the disk must expand while matter is accreting on the central star so that for $R < R_{tr}$ the resulting mass flow is directed inward (disk accretion) and for $R > R_{tr}$ outward (disk expantion). The mass flow can be written as

$$\dot{M}(R,t) = C\tilde{t}^{\left[-\frac{(5/2-\gamma)}{(2-\gamma)}\right]} e^{\left[-\frac{\tilde{R}^{(2-\gamma)}}{\tilde{t}}\right]} \tag{B.8}$$

from which we can compute the transition radius

$$R_{tr}(t) = R_1[\tilde{t}/2(2-\gamma)]^{1/(2-\gamma)} \tag{B.9}$$

As shown in figure B.1, the transition radius (red circle) moves outward as the disk evolves. In function of $R_{tr}(t)$ and the corrispondent surface density $\Sigma_{tr} = \Sigma(R_{tr}, t)$, the surface density profile can be written:

$$\Sigma_g(R,t) = \Sigma_{tr}\left(\frac{R_{tr}}{R}\right)^{\gamma} e^{-\frac{1}{2(2-\gamma)}\left[\left(\frac{R}{R_{tr}}\right)^{(2-\gamma)}-1\right]} \tag{B.10}$$

These models have been recently demostrated to more accurately reproducing the observed dust distribution in protoplanetary disks with respect to a power-law profile ([61] Hughes et al. 2008; [66] Isella et al. 2009; [6] Andrews et al. 2009) and in this thesis we try to constrain the parameter $(\gamma, R_{tr}, \Sigma_{tr})$ fitting of mm spatial resolved observation of CQTau.

Appendix C

Visibility function and uv-plane

A detailed studies of circumstellar disk in star-forming regions need high angular resolution. Since circumstellar disks in nearby star-forming typically have radii between 100 and 500 AU, sub-arcsecond angular resolution is required to spatially resolve the dust emission. Millimiter-wave interferometers are so essential for such studies. In this Appendix we give a brief description of one funtamental quantity for interferometry: the '*Visibility Function*'.

C.1 Visibility function and uv-plane

In radio astronomy, we observe the radio waves emitted from space. Since the source is far away, the received electromagnetic field intensity distribution can be observed only in an angular direction (no information regarding the intensity distribution in the radial direction). Defining the celestial sphere as the maximal sphere that contains no radiating sources, the observed intensity is the projection of the source intensity on the celestial sphere. For simplicity, we will deal with a quasi-monochromatic wave at frequency ν (the general case can be easily derived by a linear combination of quasi-monochromatic waves). The electric field at location $\mathbf{r}$ is given by

$$E_\nu(\mathbf{r}) = \int \boldsymbol{\varepsilon}_\nu(\mathbf{q}) \frac{e^{2\pi i(|\mathbf{q}-\mathbf{r}|/c)}}{|\mathbf{q}-\mathbf{r}|} dS \tag{C.1}$$

where $\boldsymbol{\varepsilon}_\nu(\mathbf{q})$ is the electric field at location $\mathbf{q}$ (on the celestian sphere), dS is surface area on the sphere and the integration is done over the entire sphere and c is the speed of light. For two antennas observing a distant source (receiving the electric field emitted by the source), there is a geometrical delay in one of the antennas relative to the other antenna derived from the source observation angle (figure C.1 a). If the geometric delay is compensed by an electronic delay, the electric field received in one antenna should be highly correlated with the electric field received by the other antenna. The spatial coherency of the electric field for two antennas located at $\mathbf{r}_1$ and $\mathbf{r}_2$ is given by

$$V_\nu(\mathbf{r}_1, \mathbf{r}_2) = \langle \mathbf{E}_\nu(\mathbf{r}_1), \mathbf{E}^*_\nu(\mathbf{r}_2) \rangle \tag{C.2}$$

where $\langle\rangle$ stands for the expectation value. Substituing (C.1) into (C.2) and taking into account the large distance of the source; i.e., $|\mathbf{q}-\mathbf{r}| \approx |\mathbf{q}|$ and that the electric field is spatially incoherent (i.e $\langle \boldsymbol{\varepsilon}_\nu(\mathbf{q}_1), \boldsymbol{\varepsilon}^*_\nu(\mathbf{q}_2) \rangle = 0 \; \forall \mathbf{q}_1 \neq \mathbf{q}_2$) we get

$$V_\nu(\mathbf{r}_1, \mathbf{r}_2) = \int I_\nu(s) e^{2\pi i(\mathbf{r}_1 - \mathbf{r}_2)/c} d\Omega \tag{C.3}$$

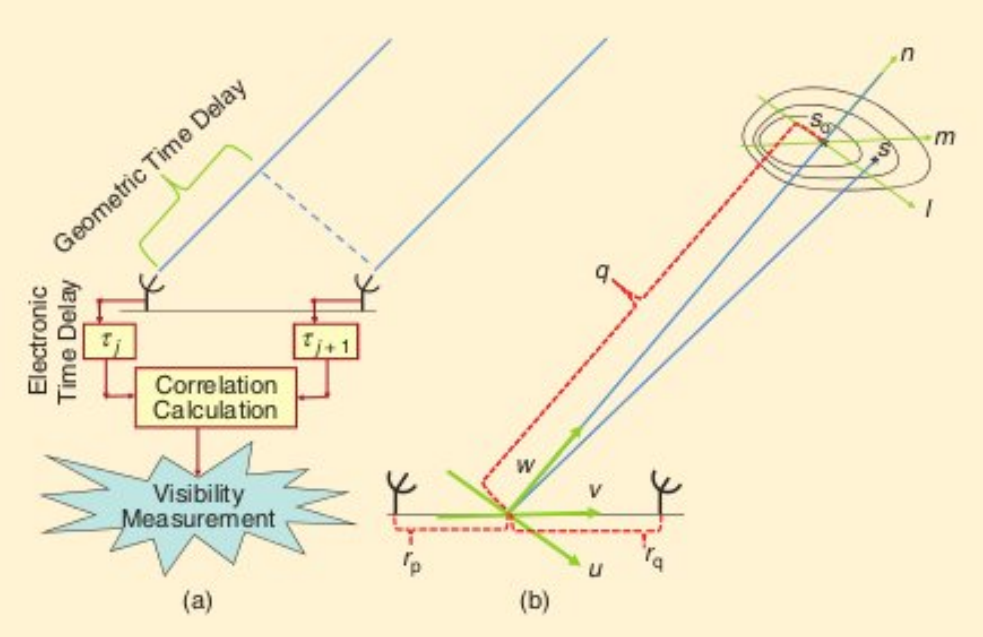

Figure C.1: The visibility is the measurement of spatial correlation between the electric field of antenna pairs. The geometric delay of the wave that propagates from the source to the two antennas is compensated by an electronic delay. (b) A distant source is observed by an antenna pair. The baseline connecting the two antennas is the origin of the (u, v, w) coordinate system. The w axis points from the baseline toward the source reference point. (u, v) are perpendicular to w and selected according to the Earth's orientation. (l, m, n) is a unit vector in the (u, v, w) system pointing toward a specific location in the source (at the source reference point S_0, $l = 0$, $m = 0$) and $n = \sqrt{1 - (l^2 + m^2)}$.

where $I_\nu(s) \equiv \langle \boldsymbol{\varepsilon}_\nu(\mathbf{s})^2 \rangle$ is the source intensity at direction s on the sphere ($\mathbf{s} \equiv \mathbf{q}/|\mathbf{q}|$), and $d\Omega = dS/|q|^2$. Rappresenting (C.3) in the (u, v, w) coordinate system (e.g. planar arrays) we obtain the visibility [1]

$$V_\nu(u, v) = \int\int I_\nu(l, m) e^{2\pi i(ul+vm)} dldm \tag{C.4}$$

The visibility is the Fourier trasform of the source intensity; therefore the inverse relation holds

$$I_\nu(l, m) = \int\int V_\nu(u, v) e^{2\pi i(ul+vm)} dudv \tag{C.5}$$

For a source with visibility measurements covering the entire (u, v) domain, the source image is perfectly computed by the Fourier inversion of the visibility. In practice, only a small part of the (u, v) domain is measured by sampling the existing

[1] the (C.4) is written in coplanar (or small-angle) approximation and we can neglect the w coordinate

antenna pair baselines as they change with the Earth's rotation relative to the (u, v) coordinates (at time t_k two antennas p and q measure a single visibility point in the (u, v) domain at (u^k_{pq}, v^k_{pq})) (figure C.1 b). This set of samples is know as the '(u, v) *coverage*' of the interferometer. This coverage is determined by many factors such as the configuration in which the individual telescopes are placed on the ground, the minimal and maximal distance between antenna pairs, the time difference between consecutive measurements and total measurement time and bandwidth

Bibliography

[1] Adams F.C., Lada C.J., Shu F.H., 1987, ApJ, 312, 788 3, 27

[2] Adams F.C., Hollenbach D., Laughlin G., Gorti U., 2004, ApJ, 611, 360 12

[3] Alexander R.D., Clarke C.J., Pringle J.E., 2006a, MNRAS, 369, 216 12

[4] Alexander R.D., Clarke C.J., Pringle J.E., 2006b, MNRAS, 369, 229 12, 13

[5] Andre P., Ward-Thompson D., Barsony M., 1993, ApJ, 406, 122 3

[6] Andrews S.M., Wilner D.J., Hughes A.M., Qi C., Dullemond C.P., 2009, ApJ, 700, 1502 19, 81, 82, 89, 92, 110

[7] Andrews S.M., Wilner D.J., Hughes A.M., Qi C., Dullemond C.P., 2010, ApJ, 723, 1241 81, 82, 89

[8] Armitage P.J., 2011, ARA&A, 49, 195 10

[9] Arquilla R., Goldsmith P.F., 1986, ApJ, 303, 356 2

[10] Auer, L.H. 1987, in Numerical Radiative Transfer, ed. W.Kalkofen, Cambridge Univ. Press, Cambridge, p.101 45

[11] Auer, L.H. 1991, in Stellar Atmospheres Beyond Classical Models, eds. L. Crivellari, I. Hubeny, D.G. Hummer, Kluwer Academic Publishers, p.9 45

[12] Auer, L., Paletou, F. 1994, A&A, 285, 675 43

[13] Balbus S.A., Hawley J.F., 1991, ApJ, 376, 214 10

[14] Banzatti A., Testi L., Isella A., Natta A., Neri R., Wilner D.J., 2011, A&A, 525, 12 95, 96

[15] Bruggeman D.A.G., 1935, Ann Phys (Leipzig) 24, 636 21, 81, 90, 95

[16] Beckwith S.V.W., Sargent A.I., Chini R.S., Guesten R., 1990, AJ, 99, 924 17

[17] Beckwith S.V.W., Henning T., Nakagawa Y., 2000, prpl.conf, 533 20

[18] Bell K.R., Lin D.N.C., 1994, ApJ, 427, 987 27

[19] Bell K.R., Cassen P.M., Klahr H.H., Henning Th., 1997, ApJ, 486, 372 11, 27

[20] Birnstiel T., Dullemond C.P., Brauer F., 2010, A&A, 513, 79B 45, 81, 90, 95, 97, 100

[21] Birnstiel T., Ricci L., Trotta F., Dullemond C.P., Natta A., Testi L., Dominik C., Henning T., Ormel C.W., Zsom A., 2010, A&A, 516, 14 70, 100

[22] Birnstiel T., Ormel C.W., Dullemond C.P., 2011, A&A, 525, 11 15

[23] Bohren C.F. and Huffman D.R. 1983 Absorption and Scattering of Light by Small Particles (New York: Wiley) 101

[24] Bonnell I.A., Larson R.B. & Zinnecker H., 2007, in Protostars and Planets V 2

[25] Bouwman J., de Koter A., Dominik C., Waters L.B.F.M., 2003, A&A, 401, 577 13

[26] Brauer F., Dullemond C.P., Henning. Th., 2008, A&A, 480, 859 6, 15, 45

[27] Bruggeman D.A.G., 1935, Ann. Phys. Leipzig 24, 636 21, 81, 90, 95

[28] Calvet N., D'Alessio P., Hartmann L., Wilner D., Walsh A., Sitko M., 2002, ApJ, 568, 1008 13

[29] Caselli P., Walmsley CM, Zucconi A., Tafalla M., Dore L., Myers PC, 2002, ApJ, 572, 238 2

[30] Chiang E.I., Goldreich P., 1997, ApJ, 490, 368 16, 27, 35, 70, 72, 73, 80, 95, 99

[31] Chiang E.I., Joung M.K., Creech-Eakman M.J., Qi C., Kessler J.E., Blake G.A., van Dishoeck E.F., 2001, ApJ, 547, 1077 38, 72, 73, 76

[32] Chiang E., Youdin A.N., 2010, AREPS, 38, 493 15

[33] Clarke C.J., Gendrin A., Sotomayor M., 2001, MNRAS, 328, 485 12

[34] D'Alessio P., Canto J., Calvet N., Lizano S., 1998, ApJ, 500, 411 11, 24, 27

[35] D'Alessio P., Calvet N., Hartmann L., Lizano S., Canto' J., 1999, ApJ, 527, 893 27

[36] D'Alessio P., Hartmann L., Calvet N., Franco-HernÃ¡ndez R., Forrest W.J., Sargent B., Furlan E., Uchida K.G.J.D., Watson D.M.; Chen C.H., Kemper F., Sloan G.C., Najita J., 2005, ApJ, 621, 461 13

[37] Draine B.T., 2006, ApJ, 636, 1114 20, 96

[38] Dullemond C.P., Dominik C., Natta A., 2001, ApJ, 560, 957 70, 71, 72, 76, 80, 95

[39] Dullemond C.P., 2002, A&A, 395, 853, 2002, A&A, 395, 853 16, 18, 41, 50, 99

[40] Dullemond C.P., van Zadelhoff G.J., Natta A., 2002, A&A, 389, 464 24, 27

[41] Dullemond C.P., Natta A., 2003, A&A, 405, 597 71

[42] Dullemond C.P., Dominik C., 2004, A&A, 417, 159 23, 45

[43] Dullemond C.P., Dominik C., 2005, A&A, 434, 971 14, 15

[44] Dullemond C.P., Dominik C., 2008, A&A, 487, 205 15

[45] Flock M., Dzyurkevich N., Klahr H., Turner N.J., Henning Th., 2011, ApJ, 735, 122 11

[46] Font A.S., McCarthy, I.G., Johnstone D., Ballantyne D.R., 2004, ApJ, 607, 890 12

[47] Forrest W.J., Sargent B., Furlan E., D'Alessio P., Calvet N., Hartmann L., Uchida K.I., Green J.D., Watson D.M., Chen C.H., Kemper F., Keller L.D., Sloan G.C., Herter T.L., Brandl B.R., Houck J.R., Barry D.J., Hall P., Morris P.W., Najita J., Myers P.C., 2004, ApJS, 154, 443 13

[48] Fromang S., Terquem C., Balbus S.A., 2002, MNRAS, 329, 18 10

[49] Fromang, S.; Papaloizou, J., 2006, A&A, 452, 751 17

[50] Fromang, S.; Papaloizou, J., 2006, A&A, 452, 751 17

[51] Fromang S., Nelson. R.P., 2009, A&A, 496, 597 17

[52] Gammie C.F., 1996, ApJ, 457, 355 9, 10

[53] Gorti U., Dullemond C.P., Hollenbach D., 2009, ApJ, 705, 1237 13

[54] Gorti U., Hollenbach. D., 2009, ApJ, 690, 1539 13

[55] Guilloteau S., Dutrey A., PiÃ©tu V., Boehler Y., 2011, A&A, 529, 105 95

[56] Hartmann L., Calvet N., Gullbring E., D'Alessio P., 1998, ApJ, 495, 385 11, 109

[57] Heng K., Kenyon S.J., 2010, MNRAS, 408, 1476 15

[58] Henning T., Stognienko R., 1996, A&A, 311, 291 20

[59] Harries T.J., 2000, MNRAS, 315, 722 23

[60] Hubeny I., 1990, ApJ, 351, 632 27

[61] Hughes A.M., Wilner D.J., Qi C., Hogerheijde M.R., 2008, ApJ, 678, 1119 18, 19, 110

[62] Hueso R., Guillot T., 2005, A&A, 442, 703 11

[63] Ilgner M., Nelson R.P., 2006, A&A, 445, 205 10

[64] Inutsuka S., Machida M.N., Matsumoto T., 2010, ApJ, 718, 58 8

[65] Isella A., Testi L., Natta A., Neri R., Wilner D., Qi C., 2007, A&A, 469, 213 18

[66] Isella A., Carpenter J.M., Sargent A.I., 2009, ApJ, 701, 260 19, 81, 82, 89, 110

[67] Isella A., Carpenter J.M., Sargent A.I., 2010, ApJ, 714, 1746 95, 109

[68] Jeans J.H., 1902, RSPTA, 199, 1. 2

[69] Jeans J.H., 1929, Astronomy and Cosmogony (Cambridge University Press.) 2

[70] Jones B.W., 2008, Int. J. Astrobiol., 7, 279 5

[71] Kenyon S.J., Hartmann L., 1987, ApJ, 323, 714 27

[72] Kunasz,P.B.,Auer,L.H.1988,J.Quant.Spectrosc.Radiat.Transfer,39,67 43

[73] Lada C.J., Wilking B.A., 1984, ApJ, 287, 610 3

[74] Lachaume R., Malbet F., Monin J.L., 2003, A&A, 400, 185 71

[75] Larson, R.B., 2003, RPPh, 66, 1651. 2

[76] Li Z., Nakamura F., 2004, ApJ, 609, 83 3

[77] Liffman K., 2003, PASA, 20, 337 12

[78] Lin D.N.C.; Bodenheimer P., 1982, ApJ, 262, 768 108

[79] Lin D.N.C.; Pringle J.E., 1987, MNRAS, 225, 607 108

[80] Lüst R., 1952, Z.Naturforsch. A, 7,87 108

[81] Lynden-Bell D., Pringle J.E., 1974, MNRAS, 168, 603 8, 18, 26, 80, 89, 95, 108

[82] Lyubarskij Y.E.; Shakura N.I., 1987, SvAL, 13, 386 108

[83] Malbet F., Bertout C., 1991, ApJ, 383, 814 27

[84] Malbet F., Lachaume. R., Monin J.-L., 2001, A&A, 379, 515 24, 27

[85] Maxwell-Garnett, 1904, Phil.Trans.R.Soc.London., 203, 385 21

[86] Mihalas, D., Auer, L. H., Mihalas, B. W. 1978, ApJ, 220, 1001 43

[87] Miyake K., Nakagawa Y., 1993, Icar, 106, 20 20

[88] Mathis J.S., Rumpl W., Nordsieck K.H., 1977, ApJ, 217, 425 81

[89] Ercolano B., Barlow M.J., Storey P.J., Liu X.W., 2003, MNRAS, 340, 1136 23

[90] Ng, K.C. 1974, J.Chem. Phys. 61, 2680 45

[91] Niccolini G., Woitke P., Lopez B., 2003, A&A, 399, 703 23

[92] Nomura H., 2002, ApJ, 567, 587 18

[93] Ormel C.W., Cuzzi J.N., 2007, A&A, 466, 413 90

[94] Ostriker E.C., Gammie C.F., Stone J.M., 1999, ApJ, 513,259 2

[95] Owen J.E., Ercolano B., Clarke C.J., Alexander R.D., 2010, MNRAS, 401, 1415 13

[96] Piétu V., Guilloteau S., Dutrey A., 2005, A&A, 443, 945 18

[97] Pinte C., Ménard F., Duchêne, G., Bastien P., 2006, A&A, 459, 797 23

[98] Pinte C., Padgett D.L., Ménard F., Stapelfeldt K.R., Schneider G., Olofsson J., Panić O., Augereau J.C., Duchêne G., Krist J., Pontoppidan K., Perrin M.D., Grady C.A., Kessler-Silacci J., van Dishoeck E.F., Lommen D., Silverstone M., Hines D.C., Wolf S., Blake G.A., Henning T., Stecklum B., 2008, A&A, 489, 633 19

[99] Pollack J.B., Hollenbach D., Beckwith S., Simonelli D.P., Roush T., Fong W., 1994, ApJ, 421, 615 20

[100] Pringle J.E., 1974, PhD thesis, Univ. Cambridge 108

[101] Pringle J.E., 1981, ARA&A, 19, 137 8, 11

[102] Ricci L., Testi L., Natta A., Neri R., Cabrit S., Herczeg G.J., 2010, A&A, 512, 15 80, 81, 82, 89

[103] Ricci L., Testi L., Natta A., Brooks K.J., 2010, A&A, 521, 66 80, 81, 82, 89

[104] Ricci L., Mann R.K., Testi L., Williams J.P., Isella A., Robberto M., Natta A., Brooks K.J., 2011, A&A, 525, 81

[105] Sauter J., Wolf S., Launhardt R., Padgett D.L., Stapelfeldt K.R., Pinte C., Duchêne G., Ménard F., McCabe C.E., Pontoppidan K., Dunham M., Bourke T.L., Chen J.H., 2009, A&A, 505, 1167 19

[106] Semenov D., Henning T., Helling C., Ilgner M., Sedlmayr E., 2003, A&A, 410, 61 20, 90

[107] Shakura N.I., Sunyaev R.A., 1973, A&A, 24, 337 8, 11, 26

[108] Shu. F.H., Johnstone D., Hollenbach D., 1993, Icar, 106, 92 11

[109] Spitzer L., 1942, ApJ, 95, 329 2

[110] Spitzer L., 1978, Physical processes in the interstellar medium (New Yoek: Wilwy-Interscience) 2, 3

[111] Steinacker J., Henning Th., Bacmann A., Semenov D., 2003, A&A, 401, 405 24

[112] Testi L., Natta A., Shepherd D.S., Wilner D.J., 2003, A&A, 403, 323 95

[113] Toomre A., 1964, ApJ, 139, 1217 10

[114] Walker C., Wood K., Lada C.J., Robitaille T., Bjorkman J.E., Whitney B., 2004, MNRAS, 351, 607 18

[115] Warren S.G., 1984, ApOpt, 23, 1206 81, 90, 96

[116] Weidenschilling S.J., 2011, Icar, 214, 671 15

[117] Weidenschilling, S. J., 1989, AdSpR, 10, 101 20

[118] Weingartner J.C., Draine B.T., 2001, ApJ, 548, 296 81, 90, 96

[119] Williams J.P., Blitz L. and McKee C.F. 2000, in Protostars and Planets IV, ed. V. Mannings et al. (Tucson: Univ. of Arizona Press), pages 97-120. 1

[120] Wolf S., 2003, CoPhC, 150, 99 23

[121] Wolf S., Padgett D.L., Stapelfeldt K.R., 2003, ApJ, 588, 373 19

[122] Wood K., Wolff M.J., Bjorkman J.E., Whitney B., 2002, ApJ, 564, 887 19

[123] Youdin A.N., Shu F.H., 2002, ApJ, 580, 494 15

[124] Zubko V.G., Mennella V., Colangeli L., Bussoletti E., 1996, MNRAS, 282, 1321 81, 90, 96

[125] Zuckerman B., Evans N.J., 1974, ApJ, 192, 149. 2

Acknowledgments

I need to thank firstly my supervisor, Leonardo Testi, who made possible my experience to ESO, to have tried to guide me in these three years, for having offered me the opportunity of a beautifull experience in Australia and especially for the infinite patience he had with me.

I am profoundly indebted with Luca Ricci for his assistance and helpfulness during all my journeys in Munich .

Many thanks go to Antonella Natta and Andrea Isella for their helpful advice and all the people I have met at ESO and for the discussion we had: Til Birnstiel, Andreas Zsom, Chris Ormel, Kees Dullemond, Carsten Dominick,.

I would like to thank all the friends I have found in Munich especially Antonio, Cosimo Andrea, Augusto, my roommate Marcos and Suraj and Claudia who made my last period in Munich very enjoyable and all the phd student and people here, in this wonderful place called Arcetri Observatory, for the pleasant moments spent together.

A big thanks also to my family for their strong support.

THANKS!!!